TU Delft

Delft University of Technology

Quantum error correction with spins in diamond

Cramer, Julia

DOI
10.4233/uuid:73f63a00-972d-4b83-8c9f-cce7dc14e048

Publication date
2016

Document Version
Final published version

Citation (APA)
Cramer, J. (2016). *Quantum error correction with spins in diamond*. [Dissertation (TU Delft), Delft University of Technology]. https://doi.org/10.4233/uuid:73f63a00-972d-4b83-8c9f-cce7dc14e048

Important note
To cite this publication, please use the final published version (if applicable).
Please check the document version above.

Copyright
Other than for strictly personal use, it is not permitted to download, forward or distribute the text or part of it, without the consent of the author(s) and/or copyright holder(s), unless the work is under an open content license such as Creative Commons.

Takedown policy
Please contact us and provide details if you believe this document breaches copyrights.
We will remove access to the work immediately and investigate your claim.

This work is downloaded from Delft University of Technology.
For technical reasons the number of authors shown on this cover page is limited to a maximum of 10.

Quantum error correction with spins in diamond

Julia Cramer



Quantum error correction with spins in diamond

Quantum error correction with spins in diamond

Proefschrift

ter verkrijging van de graad van doctor
aan de Technische Universtiteit Delft,
op gezag van de Rector Magnificus Prof. ir. K.C.A.M. Luyben,
voorzitter van het College voor Promoties,
in het openbaar te verdedigen op 8 december 2016 om 10:00 uur

door

Julia CRAMER

Master of Science in Applied Physics
Technische Universiteit Delft, Nederland
geboren te Eindhoven, Nederland

This dissertation has been approved by the promotor:

Prof. dr. ir. R. Hanson

Composition of the doctoral committee:

Rector Magnificus,	chairman
Prof. dr. ir. R. Hanson,	Delft University of Technology, promotor
Dr. ir. T. H. Taminiau,	Delft University of Technology, copromotor

Independent members:

Prof. dr. ir. L. M. K. Vandersypen	Delft University of Technology
Prof. dr. ir. K. L. M. Bertels	Delft University of Technology
Prof. Dr. F. Jelezko	Ulm University
Prof. Dr. B. M. Terhal	RWTH Aachen University



Copyright © 2016 by Julia Cramer

All rights reserved. No part of this book may be reproduced, stored in a retrieval system, or transmitted, in any form or by any means, without prior permission from the copyright owner.

ISBN 978-90-8593-270-3

Casimir PhD Series Delft-Leiden 2016-26

Cover design by Caroline Beck

Printed by Gildeprint - www.gildeprint.nl

An electronic version of this thesis is available at www.library.tudelft.nl/dissertations

Contents

1 Introduction **1**
1.1 The future is quantum . . . 2
1.2 A quantum register based on spins in diamond . . . 3
1.3 Thesis overview . . . 5
1.4 Bibliography . . . 6

2 Elements of experimental quantum error correction **11**
2.1 Introduction . . . 12
2.2 Quantum errors . . . 13
2.3 Relevant error-correction codes . . . 13
2.3.1 Bit-flip code . . . 14
2.3.2 Five-qubit quantum error correction . . . 15
2.3.3 Unencoding the logical quantum state . . . 15
2.3.4 Logical qubit operations . . . 16
2.4 Fault-tolerant quantum computing . . . 16
2.4.1 Fault-tolerant quantum operations . . . 17
2.4.2 Error correction and feedback . . . 17
2.5 Characterization of QEC . . . 18
2.5.1 Process fidelity . . . 18
2.5.2 Error syndrome detection . . . 19
2.6 Conclusion . . . 21
2.7 Bibliography . . . 22

3 The Nitrogen-Vacancy centre as quantum node **25**
3.1 The NV centre in diamond . . . 26
3.2 Optical properties of the NV electron spin . . . 27
3.2.1 Room-temperature optical addressing of the NV centre . . . 28
3.2.2 Fine-structure optically excited state . . . 29
3.3 Properties of the ground state NV electronic spin state . . . 32
3.3.1 The nitrogen host spin . . . 32
3.3.2 Electron spin coherence . . . 33

3.4 Weakly coupled spins as qubits in a quantum register 34
3.4.1 Interaction Hamiltonian 34
3.4.2 Detection and characterization of nuclear spins 35
3.4.3 Control and operations 39
3.5 Experimental methods 40
3.5.1 Diamond samples 40
3.5.2 Experimental spin control 41
3.5.3 Resonant readout and initialization - cryogenic temperatures . 41
3.5.4 Real-time feedback 42
3.6 Bibliography 45

4 Universal control and error correction in multi-qubit spin registers in diamond 49
4.1 Introduction 50
4.2 Detection and control of weakly coupled nuclear spins in diamond . 50
4.3 Three-qubit error correction 54
4.4 Discussion 56
4.5 Methods 56
4.5.1 Diamond sample and hyperfine interactions 56
4.5.2 Nuclear gate design 58
4.5.3 Nuclear spin initialization 58
4.5.4 Quantum error correction analysis 59
4.6 Supporting material 59
4.6.1 Setup and sample 59
4.6.2 Electron spin initialization and readout 60
4.6.3 Experimental 60
4.6.4 Characterization and control for three NV centres 62
4.6.5 Nuclear spin dynamics and gates 65
4.6.6 Nuclear initialization fidelity 69
4.6.7 Two-qubit tomography 71
4.6.8 Quantum error correction 71
4.6.9 Decoherence and depolarization 78
4.6.10 Fidelity estimates 84
4.7 Bibliography 86

5 Repeated quantum error correction on a continuously encoded qubit by real-time feedback 89
5.1 Introduction 90
5.2 Error correction code 90
5.3 Stabilizer measurements and real-time feedback 92
5.4 Active quantum error correction on a logical qubit 92
5.5 Multiple rounds of active error correction 94
5.6 Correcting natural dephasing 96

5.7 Discussion . . . 96
5.8 Methods and theoretical analysis . . . 98
5.8.1 Sample and Setup . . . 98
5.8.2 Nuclear spin qubit control . . . 98
5.8.3 Feedback . . . 98
5.8.4 Quantum error correction analysis . . . 99
5.8.5 Error probabilities . . . 102
5.8.6 Qubit readout calibration . . . 103
5.9 Bibliography . . . 116

6 Towards fault-tolerant QEC experiments with spins in diamond 119
6.1 Introduction . . . 120
6.2 Quantum error detection . . . 120
6.2.1 Logical qubit . . . 121
6.2.2 Error detection . . . 122
6.3 Five-qubit quantum error correction . . . 123
6.3.1 Logical qubit . . . 123
6.3.2 Error syndrome detection and correction . . . 125
6.3.3 Proposed experimental implementation . . . 125
6.4 Discussion . . . 127
6.5 Bibliography . . . 129

7 Conclusions and outlook 131
7.1 Conclusions . . . 132
7.2 Extended quantum error correction protocols . . . 133
7.3 Quantum networks . . . 134
7.4 Other related experiments . . . 135
7.5 Bibliography . . . 137

Summary 141

Samenvatting 143

Acknowledgements 145

List of Publications 149

Curriculum Vitae 151

Chapter 1

Introduction

J. Cramer

We cannot clone, perforce; instead, we split
Coherence to protect it from that wrong
That would destroy our valued quantum bit
And make our computation take too long.

Correct a flip and phase - that will suffice.
If in our code another error's bred,
We simply measure it, then God plays dice,
Collapsing it to X or Y or Zed.

We start with noisy seven, nine, or five
And end with perfect one. To better spot
Those flaws we must avoid, we first must strive
To find which ones commute and which do not.

With group and eigenstate, we've learned to fix
Your quantum errors with our quantum tricks.

—Daniel Gottesman - *Quantum Error Correction Sonnet*[1] (1999)

The laws of quantum mechanics provide ways to develop computational systems that promise to be incredibly more efficient than any classical system. A major challenge in quantum information technology however is the protection of quantum information against inevitable errors. The Quantum Error Correction Sonnet points out important aspects of quantum computation and error correction:

- We need to protect quantum information against errors, otherwise quantum computations take too long and there is no advantage over classical computations.
- While we cannot clone quantum information, error correction based on 'quantum tricks' can transform noisy quantum bits into perfect ones.

This thesis focusses on the experimental implementation of such 'quantum tricks', quantum error correction, on a quantum register based on spins in diamond. In this chapter I will give an introduction to quantum information processing and quantum error correction. Additionally, I will introduce the nitrogen vacancy (NV) centre in diamond, the experimental platform for the work presented in this thesis.

1.1 The future is quantum

The beginning of the 20th century is featured by a turning point in the physical sciences. The laws of classical physics did not suffice to describe the world of very small particles such as atoms, electrons and photons. Under large debate, the laws of quantum mechanics were developed, which predict that the state of these small particles (quantum particles) can be described by a complex-valued wavefunction, implying counter-intuitive particle-wave-like behavior. Quantum particles can be in two states at the same time (*superposition*), share a single quantum state with another quantum particle (*entanglement*) and their wavefunction is perturbed upon measurement.

While the laws of quantum mechanics caused confusion among these physicists, at the end of the century it was realized that quantum mechanics could be a game-changer in future information technology. Quantum algorithms were developed that predicted a great potential in computing power and first experiments based on the laws of quantum mechanics were performed on quantum systems such as single photons[2], nuclear magnetic resonance[3], atoms and ions[4], superconducting systems[5] and solid-state spins[6].

Quantum information technology builds on the idea that the building blocks of quantum computers, quantum bits (qubits), can replace classical bits to efficiently solve specific computational problems such as factorizing large numbers[7]. A quantum bit of information follows the laws of quantum mechanics; where a classical bit can take values of either '0' or '1', a quantum bit can be in any superposition of $|0\rangle$ and

$|1\rangle$. This results in a scaling law[8] for the number of degrees of freedom that can be simultaneously represented in an N-qubit system following 2^N.

Besides quantum computing, promising state-of-the-art research in quantum information technology is focussed on the realization of quantum networks[9,10], networks that connect nodes by means of quantum entanglement. These networks can be used to study both fundamental questions as well as future applications, such as fundamentally secure communication[11].

One of the main challenges in quantum information processing is the protection of quantum information against errors[12]. Correcting errors in quantum states is fundamentally challenging by three important consequences of the laws of quantum mechanics. First of all, a quantum state can not be copied[13], secondly, a measurement irreversably projects a quantum state and finally, quantum errors are intrinsically continuous[14].

Nevertheless, in the last years of the 20th century, the first protocols on the correction of errors were proposed by Peter Shor[15] and Andrew Steane[16]. This thesis will follow their steps from theory towards experimental implementations of quantum error correction. Following the protocols, a quantum state is protected by redundant encoding in multiple data qubits. Errors are detected by correlation measurements (stabilizer measurements) on the data qubits via ancillary qubits, and subsequently corrected. This thesis focusses on the experimental implementation of such quantum error correction codes in a quantum system based on spins in diamond.

1.2 A quantum register based on spins in diamond

The work presented in this thesis is based on the nitrogen vacancy (NV) color centre in diamond. This solid-state system with atomic-like properties is a promising building block for the implementation of quantum technology[17]. It combines the long coherence times of an isolated spin system[18,19] with the opportunities of the semiconductor industry[20]. The NV center supplies an electron spin system that can serve as an optical interface, suitable for exploration of remote quantum communication[21–23]. Moreover, the naturally available nuclear spins in the spin bath coupled to the NV electron spin provide a local quantum register of long-lived nuclear spins[19,24–36].

The NV electronic spin can be initialized and read out by optical means, even at ambient temperatures[37]. Moreover, at cryogenic temperatures (~ 4 K), the resonant excitation of spin-selective optical transitions can be used for high-fidelity single-shot readout and initialization of the electron spin state[38,39]. These properties make the NV centre a leading platform in remote quantum communication experiments.[21–23].

The manipulation of the NV electron spin using magnetic resonance techniques constitutes a robust control of the electron spin state as a quantum bit[24,40,41]. The dominant source of decoherence of the electron spin is the slowly fluctuating nuclear

spin bath. Dynamical decoupling techniques effectively suppress this noise, resulting in an improvement of the coherence times by orders of magnitude[42–45].

Although nuclear spins in the environment of the NV center are the main source of decoherence to the NV electron spin, recent work has shown detection and characterization of the long-lived nuclear spins via the NV center[26,35,36,46,47]. In Chs. 4,5 of this thesis, we show complete coherent control of these nuclear spins, turning them from a source of decoherence into a multi-qubit spin register. The control of such nuclear spins that are naturally available in the diamond lattice allows for the control of a long-lived spin register as a local node in diamond. In this thesis I present the implementation of quantum error correction codes based on multiple nuclear spins that are controlled as qubits via the NV electron spin.

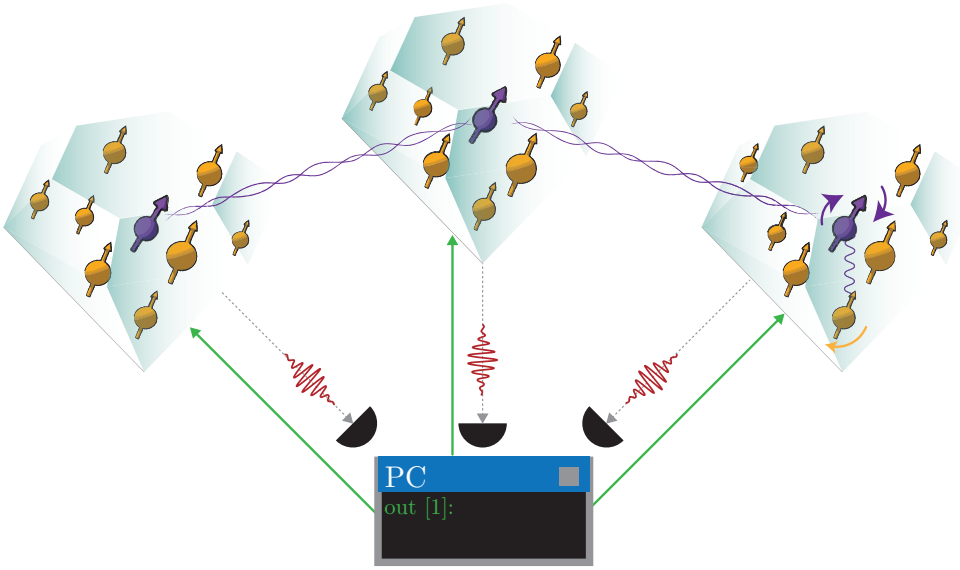


Figure 1.1 — Quantum error correction and quantum networks based on spins in diamond. Illustration of the envisioned implementation of quantum networks based on spins in diamond[10] with spin registers as local nodes. Each NV electron spin is surrounded by nuclear spins that can be individually controlled by dynamical decoupling of the electron spin[26,36]. The NV electron spin can be optically read out and classical feedback can be applied. Entangled networking links between distant NV centres are generated via photon interference and measurements[48].

1.3 Thesis overview

The structure of this thesis is as follows:

In **chapter 2** I present the elements of quantum error correction that are relevant for the results presented in this thesis. I will discuss quantum errors, quantum error correction codes and requirements for fault-tolerant quantum error correction. Furthermore, I will briefly discuss the experimental characterization of quantum error correction experiments.

Chapter 3 focusses on the NV centre and the spin register based on nuclear spins in the diamond lattice relevant for this thesis. I will discuss control, initialization and readout of the NV electron spin. Furthermore, I will describe the detection and control of nuclear spins as qubits. Finally, I will give an outline of the experimental setups used for this thesis.

Chapter 4 covers the implementation of an error correction protocol with spins in diamond at ambient temperatures. We show universal control over multiple nuclear spins via the electron spin. A quantum state is encoded in the NV electron spin and two nuclear spins. Errors are detected by reversing the encoding to the electron spin and corrected via a doubly-controlled operation.

In **chapter 5** we show the implementation of a repeated three-qubit quantum error correction code by stabilizer measurements and active feedback on a continuously encoded quantum state. An arbitrary quantum state is continuously encoded in three nuclear spins and errors are detected and corrected via the NV electron spin. The electron spin is used as ancilla qubit, enabled by its high-fidelity non-destructive readout at cryogenic temperatures.

Chapter 6 proposes experiments on quantum error detection and correction codes that can detect both bit-flip and phase-flip errors that will be feasible in the near future, based on the developed spin register and control methods. I will discuss the experimental implementation of a four-qubit quantum error detection scheme in which two logical qubits are encoded to detect general single-qubit errors. Finally, I will discuss a five-qubit quantum error correction scheme in which a general single-qubit errors can be corrected.

Finally, in **chapter 7** the main results of this thesis will be summarized and an outlook towards the implementation of extended quantum error correction codes and the exploration of quantum networks will be given.

1.4 Bibliography

[1] D. Gottesman. Quantum Error Correction Sonnet (1999).

[2] A. Aspect, P. Grangier and G. Roger. Experimental Realization of Einstein-Podolsky-Rosen-Bohm Gedankenexperiment: A New Violation of Bell's Inequalities. *Physical Review Letters* **49**, 91 (1982).

[3] I. L. Chuang, N. Gershenfeld and M. Kubinec. Experimental Implementation of Fast Quantum Searching. *Physical Review Letters* **80**, 3408 (1998).

[4] J. I. Cirac and P. Zoller. Quantum Computations with Cold Trapped Ions. *Physical Review Letters* **74**, 4091 (1995).

[5] J. Clarke and F. K. Wilhelm. Superconducting quantum bits. *Nature* **453**, 1031 (2008).

[6] R. Hanson and D. D. Awschalom. Coherent manipulation of single spins in semiconductors. *Nature* **453**, 1043 (2008).

[7] P. W. Shor. Polynomial-Time Algorithms for Prime Factorization and Discrete Logarithms on a Quantum Computer. *arXiv:quant-ph/9508027* (1995).

[8] R. P. Feynman. Simulating physics with computers. *International Journal of Theoretical Physics* **21**, 467.

[9] H. J. Kimble. The quantum internet. *Nature* **453**, 1023 (2008).

[10] N. H. Nickerson, Y. Li and S. C. Benjamin. Topological quantum computing with a very noisy network and local error rates approaching one percent. *Nature Communications* **4**, 1756 (2013).

[11] A. Ekert and R. Renner. The ultimate physical limits of privacy. *Nature* **507**, 443 (2014).

[12] M. H. Devoret and R. J. Schoelkopf. Superconducting Circuits for Quantum Information: An Outlook. *Science* **339**, 1169 (2013).

[13] W. K. Wootters and W. H. Zurek. A single quantum cannot be cloned. *Nature* **299**, 802 (1982).

[14] S. J. Devitt, W. J. Munro and K. Nemoto. Quantum error correction for beginners. *Reports on Progress in Physics* **76**, 076001 (2013).

[15] P. W. Shor. Scheme for reducing decoherence in quantum computer memory. *Physical Review A* **52**, R2493 (1995).

[16] A. M. Steane. Error Correcting Codes in Quantum Theory. *Physical Review Letters* **77**, 793 (1996).

[17] L. Childress and R. Hanson. Diamond NV centers for quantum computing and quantum networks. *MRS Bulletin* **38**, 134 (2013).

[18] G. Balasubramanian *et al.* Ultralong spin coherence time in isotopically engineered diamond. *Nature Materials* **8**, 383 (2009).

[19] P. C. Maurer *et al.* Room-Temperature Quantum Bit Memory Exceeding One Second. *Science* **336**, 1283 (2012).

[20] D. D. Awschalom, L. C. Bassett, A. S. Dzurak, E. L. Hu and J. R. Petta. Quantum Spintronics: Engineering and Manipulating Atom-Like Spins in Semiconductors. *Science* **339**, 1174 (2013).

[21] H. Bernien. *Control, measurement and entanglement of remote quantum spin registers in diamond*. PhD Thesis, Delft, University of Technology (2014).

[22] W. Pfaff. *Quantum measurement and entanglement of spin quantum bits in diamond*. PhD Thesis, Delft, University of Technology (2013).

[23] B. Hensen *et al.* Loophole-free Bell inequality violation using electron spins separated by 1.3 kilometres. *Nature* **526**, 682 (2015).

[24] F. Jelezko *et al.* Observation of Coherent Oscillation of a Single Nuclear Spin and Realization of a Two-Qubit Conditional Quantum Gate. *Physical Review Letters* **93**, 130501 (2004).

[25] L. Jiang *et al.* Coherence of an Optically Illuminated Single Nuclear Spin Qubit. *Physical Review Letters* **100**, 073001 (2008).

[26] T. H. Taminiau *et al.* Detection and Control of Individual Nuclear Spins Using a Weakly Coupled Electron Spin. *Physical Review Letters* **109**, 137602 (2012).

[27] M. V. G. Dutt *et al.* Quantum Register Based on Individual Electronic and Nuclear Spin Qubits in Diamond. *Science* **316**, 1312 (2007).

[28] P. Neumann *et al.* Multipartite Entanglement Among Single Spins in Diamond. *Science* **320**, 1326 (2008).

[29] P. Neumann *et al.* Single-Shot Readout of a Single Nuclear Spin. *Science* **329**, 542 (2010).

[30] A. Dréau, P. Spinicelli, J. R. Maze, J.-F. Roch and V. Jacques. Single-Shot Readout of Multiple Nuclear Spin Qubits in Diamond under Ambient Conditions. *Physical Review Letters* **110**, 060502 (2013).

[31] W. Pfaff *et al.* Unconditional quantum teleportation between distant solid-state quantum bits. *Science* **345**, 532 (2014).

[32] T. van der Sar *et al.* Decoherence-protected quantum gates for a hybrid solid-state spin register. *Nature* **484**, 82 (2012).

[33] G. Waldherr *et al.* Quantum error correction in a solid-state hybrid spin register. *Nature* **506**, 204 (2014).

[34] E. Kessler, I. Lovchinsky, A. Sushkov and M. Lukin. Quantum Error Correction for Metrology. *Physical Review Letters* **112**, 150802 (2014).

[35] A. Reiserer *et al.* Robust Quantum-Network Memory Using Decoherence-Protected Subspaces of Nuclear Spins. *Physical Review X* **6**, 021040 (2016).

[36] T. H. Taminiau, J. Cramer, T. v. d. Sar, V. V. Dobrovitski and R. Hanson. Universal control and error correction in multi-qubit spin registers in diamond. *Nature Nanotechnology* **9**, 171 (2014).

[37] F. Jelezko, T. Gaebel, I. Popa, A. Gruber and J. Wrachtrup. Observation of Coherent Oscillations in a Single Electron Spin. *Physical Review Letters* **92**, 076401 (2004).

[38] L. Robledo, H. Bernien, I. van Weperen and R. Hanson. Control and Coherence of the Optical Transition of Single Nitrogen Vacancy Centers in Diamond. *Physical Review Letters* **105**, 177403 (2010).

[39] L. Robledo, H. Bernien, T. v. d. Sar and R. Hanson. Spin dynamics in the optical cycle of single nitrogen-vacancy centres in diamond. *New Journal of Physics* **13**, 025013 (2011).

[40] G. D. Fuchs, V. V. Dobrovitski, D. M. Toyli, F. J. Heremans and D. D. Awschalom. Gigahertz Dynamics of a Strongly Driven Single Quantum Spin. *Science* **326**, 1520 (2009).

[41] M. W. Doherty *et al.* The nitrogen-vacancy colour centre in diamond. *Physics Reports* **528**, 1 (2013).

[42] G. de Lange. *Quantum control and coherence of interacting spins in diamond.* PhD Thesis, Delft, University of Technology (2012).

[43] C. A. Ryan, J. S. Hodges and D. G. Cory. Robust Decoupling Techniques to Extend Quantum Coherence in Diamond. *Physical Review Letters* **105**, 200402 (2010).

[44] B. Naydenov *et al.* Dynamical decoupling of a single-electron spin at room temperature. *Physical Review B* **83**, 081201 (2011).

[45] N. Bar-Gill, L. M. Pham, A. Jarmola, D. Budker and R. L. Walsworth. Solid-state electronic spin coherence time approaching one second. *Nature Communications* **4**, 1743 (2013).

[46] S. Kolkowitz, Q. P. Unterreithmeier, S. D. Bennett and M. D. Lukin. Sensing Distant Nuclear Spins with a Single Electron Spin. *Physical Review Letters* **109**, 137601 (2012).

[47] N. Zhao *et al.* Sensing single remote nuclear spins. *Nature Nanotechnology* **7**, 657 (2012).

[48] H. Bernien *et al.* Heralded entanglement between solid-state qubits separated by three metres. *Nature* **497**, 86 (2013).

Chapter 2

Elements of experimental quantum error correction

J. Cramer

The protection of quantum states against errors is a major challenge on the road towards large-scale quantum information processing. Quantum error correction codes protect quantum information against errors by redundant encoding in multiple data qubits. Errors are detected and corrected by stabilizer measurements and feedback. In this chapter I will discuss elements of the remarkable concept of quantum error correction that are relevant for the experiments presented in this thesis and for those planned in the near future. After briefly discussing the quantum nature of errors in quantum systems (Sec. 2.2), in Sec. 2.3 I will introduce the three-qubit bit-flip code and the smallest general quantum error correction code, in which a quantum state is encoded in five data qubits. I will discuss fault tolerance, a key requirement for scalable quantum error correction (Sec. 2.4) and experimental characterization methods for the implementation of quantum error correction codes in Sec. 2.5.

2.1 Introduction

Correcting errors is essential for the feasibility of quantum information processing. Quantum information is substantially influenced by its environment and both bit-flip and phase-flip errors continuously grow. Error correction can be a matter of redundancy, but the 'no-cloning'-theorem complicates this for quantum states; a quantum state can not simply be copied[1]. Furthermore, detecting errors by measurements of individual quantum states would immediately project these quantum states. The discovery of codes to correct errors in quantum states was therefore truly surprising[2–5].

In 1995 Peter Shor[2] and Andrew Steane[3] independently found a way to work around these seemingly deal-breaking obstacles. They came up with quantum error correction (QEC) codes: detecting and correcting errors in quantum states. These codes can be implemented such that the realization of (almost) noise-free quantum computations can be realized at the cost of acceptable overhead[6]. In an error-corrected quantum system, with an average error probability that is less than a critial value (the accuracy threshold), arbitrary long quantum computations can be reliably performed[7,8].

In this chapter, I will consider QEC codes based on stabilizer measurements and ancilla qubits. A general example is given in Fig. 2.1; a logical qubit is protected by

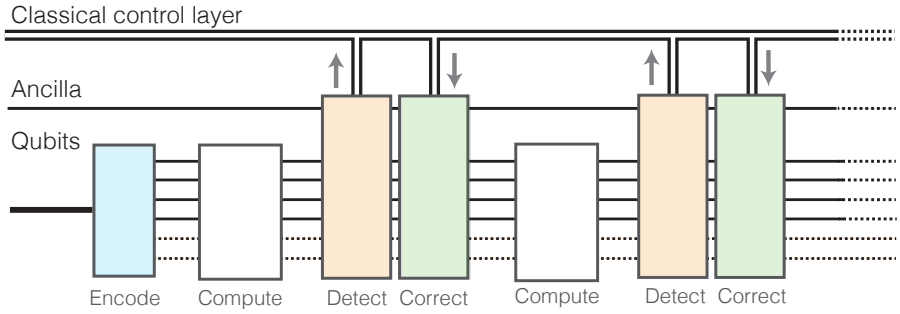


Figure 2.1 — General concept of quantum error correction based on stabilizer measurements. A logical qubit is protected by encoding in an entangled state of multiple data qubits. Errors occur on the data qubits due to uncontrolled interactions with the environment and due to finite precision in control operations ('compute'). Ancilla-based stabilizer measurements on the data qubits project and thereby effectively discretize the errors. The measurement outcomes of the stabilizer measurements contain information on the projected errors (the error syndrome), which is processed by a classical control layer to apply the feedback required to correct the detected error where needed. Rounds of error detection and correction can be repeated on the continuously encoded logical qubit.

redundantly encoding in multiple (physical) data qubits. The logical qubit is described by the logical code space which is defined by a set of stabilizer operators, and a logical operator defining the codewords, the logical eigenstates of the QEC code[9]. The stabilizer operators and logical operators are Kronecker products of single-qubit Pauli operators (X, Y, Z operations) and define the so-called 'Pauli frame'[10] of the logical qubit.

Errors are repeatedly detected by measuring the stabilizer operators via ancilla qubits. These stabilizer measurements project the continuous errors on the data qubits to discrete Pauli (X, Y or Z) operations on the data qubits. The resulting measurement outcomes form the error syndrome and are processed in a classical control layer, where the most probable error is determined[11]. Succesfully detected errors can be corrected where needed by adapting the Pauli frame or by single-qubit Pauli operations.

The overview given in this chapter is not intended to be a complete review of the theoretical foundations of QEC. Instead, this chapter gives an overview of relevant elements for the implementation of QEC in our experiments. I will briefly point out recent experimental considerations and will discuss the characterization of QEC experiments.

2.2 Quantum errors

Before discussing QEC methods, I will briefly discuss sources and types of errors. It is important to note that quantum errors can be continuous. For instance, in experimental quantum information amplitudes and phases can fluctuate over time. By the implementation of stabilizer measurements in QEC, all errors are discretized to X, Y or Z (Pauli) errors.

The types of errors are highly dependent on the specific physical system. Sources of errors such as imperfect measurement and initialization, loss and leakage eventually can all be brought back to coherent and incoherent error models[9]. Errors can be systematic and coherent, caused by imperfect knowledge of the experimental system. To a large extent such errors can be prevented by a better characterization of the full physical system and can finally be projected and corrected by QEC. Another important source of errors is the decoherence caused by uncontrolled coupling to the environment. This can be modeled as a qubit (partly) entangling to another, unknown, quantum system, which is then traced out, such that a pure state eventually ends up fully mixed.

2.3 Relevant error-correction codes

The work presented in this thesis covers experiments on the implementation of quantum error correction protocols with spins in diamond. In Ch. 4 the experimental imple-

mentation of a three-qubit measurement-free bit-flip code is presented, circumventing the challenging implementation of stabilizer measurements. In these experiments the encoding of the logical qubit is reversed to perform correction, to avoid the need for extra ancilla qubits but leaving the quantum state unprotected. In Ch. 5 repeated three-qubit phase-flip QEC by stabilizer measurements and real-time feedback is implemented on a continuously encoded logical qubit. Ch. 6 gives an outlook on general QEC codes, codes that correct for both single bit- and phase-flip errors. In this section we will discuss the basic principles of all these codes.

2.3.1 Bit-flip code

The smallest quantum error correction code, the three-qubit repetition code, corrects single-qubit errors around a single axis (X, Y or Z errors). This code relies on majority voting without projecting the individual qubit states[2]. A logical qubit is encoded in three data qubits. The code space is defined by two stabilizer operators and a third operator defines the codeword.

For example, when protecting the logical qubit against single-qubit bit-flip (X) errors, the data qubits are encoded in the logical qubit $\alpha\,|0\rangle_L + \beta\,|1\rangle_L = \alpha\,|000\rangle + \beta\,|111\rangle$. The codewords are defined by (for example) logical qubit operator ZII and the code space is defined by stabilizer operators ZZI and IZZ. The error syndrome is based on the outcomes of measurement of these stabilizer operators (Fig. 2.2a) and reveals information on the majority of the quantum states along the z-axis, without learning

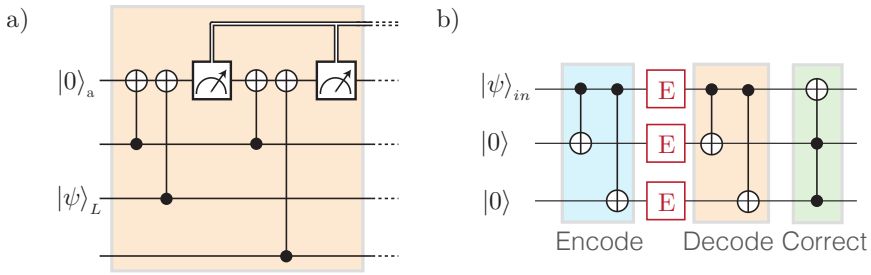


Figure 2.2 — Three-qubit quantum error correction codes, correcting for bit-flip errors. **a**, Detection of errors on a continuously encoded quantum state. Stabilizer measurements via the ancilla qubit compare the data qubits in the encoding to obtain the error syndrome. The measurement outcomes are classically processed to correct the detected error if needed. **b**, Measurement-free error correction code. A quantum state is encoded in three qubits. To correct for errors, the quantum state is decoded to a single qubit, leaving the system unprotected. The two remaining qubits contain information on the error. A doubly-controlled (Toffoli) gate corrects this error on the quantum state.

anything about the encoded nor the individual quantum states.

The three-qubit code does not protect a quantum state against errors around the other axes. For example, the bit-flip code does not correct for Z or Y errors, which can become logical errors. However, the experimental implementation of such a quantum error correction code will provide insight in the working and implementation of larger error-correction codes in similar systems.

2.3.2 Five-qubit quantum error correction

Protecting a qubit against general single-qubit errors (X, Y and Z errors) requires a minimum of five data qubits[12,13]. The code space is defined by four stabilizer operators and a fifth operator defines the codewords. In the five-qubit quantum error correction code considered here, these four stabilizer operators are measured via an ancilla qubit resulting in 16 possible error syndromes to be distinguished.

An example of a set of stabilizer operators defining the code space in the five-qubit code is given by the operators $IXZZX$, $XIXZZ$, $ZXIXZ$ and $ZZXIX$. Any encoded logical quantum state is an eigenstate of these operators. Finally, a fifth operator defines the logical eigenstates, the codewords $|0\rangle_L$ and $|1\rangle_L$, for example the operator $ZZZZZ$. In Ch. 6 we propose the experimental implementation of such five-qubit QEC based on spins in diamond.

2.3.3 Unencoding the logical quantum state

Circumventing the experimentally challenging stabilizer measurements and the need for extra ancilla qubits, first experiments implemented quantum error correction protocols based on reversing the encoding of (unencoding) the logical qubit[14–20] (Fig. 2.2b). A logical qubit is encoded in data qubits and ancilla qubits. After unencoding, the ancilla qubits contain information about the error on the data qubits. Errors can be corrected either in a measurement-free manner by a double-controlled gate (Toffoli gate), or by measuring the ancilla qubits and applying feedback to correct potential errors on the data qubits. Interestingly, in a measurement-free protocol, the quantum error is not discretized.

For example, using three qubits in total, two ancilla qubits and a single data qubit, one can correct for single-qubit bit-flip or phase-flip errors (Fig. 2.2b). The logical state is encoded in the three qubits and unencoded to the data qubit to detect and correct errors. The experimental implementation of this code is presented in Ch. 4. Expanding the system to a minumum of five qubits allows for the detection and correction of both bit- and phase-flip errors[12].

While such schemes are able to correct for errors on the encoded qubit, thus for errors that occur in between encoding and unencoding, the unencoded data qubit is unprotected during detection and correction of errors[8,21,22]. In physical systems,

errors can occur on all qubits (data and ancilla qubits) and at any time around any axis. Reversing the encoding of the logical quantum state to a single qubit to detect and correct errors leaves the quantum state unprotected: an error on the unencoded qubit results in uncorrectable errors.

2.3.4 Logical qubit operations

Universal control over the logical encoded qubit requires universal operations on the logical qubit. In the next section we will discuss the implementation of specific fault-tolerant logical operations. However, the implementation of fault-tolerant arbitrary operations on a logical qubit is a complex and challenging task which requires long gate sequences[23].

Arbitrary logical operations can be implemented in a not fault-tolerant manner via the ancilla qubit. Arbitrary rotations on the ancilla qubit can be tranferred to the logical qubit either via measurement of the ancilla qubit or by a unitary two-qubit circuit. Such operations are fundamentally not fault-tolerant as a single error on the ancilla qubit can propagate to the logical qubit, introducing incorrectable errors. In Fig. 2.3 examples of such logical operations are given.

2.4 Fault-tolerant quantum computing

The principle of fault tolerance states that information can be processed while preventing information loss. A practical and useful quantum information system tolerates (small) errors, which do not lead to computational errors. Such a system is a *fault-tolerant system*[22].

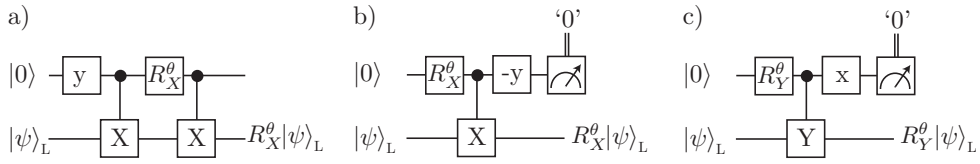


Figure 2.3 — Implementations of universal logical qubit operations. a, Deterministic arbitrary rotation around the x-axis. The operation R_x^θ on the ancilla qubit, a rotation around the x-axis with angle θ, is transferred onto the logical qubit. **b, c,** A chosen rotation R_X^θ (**b**) or R_Y^θ (**c**) is transferred from the ancilla qubit onto the logical qubit when the ancilla qubit is projected in '0'. For measurement outcome '1' the opposite rotation ($R_{X,Y}^{-\theta}$) is performed on the logical qubit. Arbitrary rotations around the z-axis can be constructed in a similar way.

In quantum circuits, errors can cascade, either by propagation through multi-qubit gates or by a faulty operation. Furthermore, errors can occur in measurements: an error on an ancilla qubit or a stabilizer measurement can result in errors in the classical data. This requires quantum error correction and operations to be designed such that errors do not evolve to logical errors: a single error remains a single error thoughout a circuit, which is then corrected by QEC. A fault-tolerant quantum computation consists of logical gates that do not spread errors[21,22].

A consequence of the fault-tolerance theory is the threshold theorem: if the error rates in quantum gates in a fault-torant quantum circuit are below the accuracy threshold an arbitrarily long quantum computation can be processed without significant information loss. To allow for a scalable quantum information system a strict threshold on the error-rate on the data qubits should be met[8]. Besides limitations on the system architecture, this threshold is a trade-off between the failure rate of a qubit (p) and the number of possible two-qubit error combinations (c) that can occur in a single-error correction cycle. For the codes discussed in this thesis, that correct for single-qubit errors, meeting the condition $cp < 1$ indicates that the failure rate of an encoded qubit can be made arbitrarily small by concatenation[4,6,8,9].

2.4.1 Fault-tolerant quantum operations

The most intuitive fault-tolerant operations that do not require any overhead are transversal operations. An intuitive example of such logical operations is available for the encoding in seven qubits (Steane code). A transversal single-qubit operation can be the logical X-gate: $X_L = XXXXXXX$, a sequence of elementary operations on the data qubits. Similarly a transversal logical two-qubit gate in this code such as the CNOT-operation can be constructed by bit-wise CNOT-operations between the data qubits of two logical qubits. A complete gate set in a fault-tolerant universal quantum computation will contain at least one non-transversal operation[24].

Two types of operations can be distinguished in quantum information processing. The first group of operations is the Clifford group, that maps Pauli operators to Pauli operators[4]. The set of Clifford operations is for example spanned by $\{H, S, \mathrm{CNOT}\}$, with $S^2 = Z$ a phase gate. If a quantum circuit only consists of operations from the Clifford group, the computation can be efficiently simulated by a classical computer[25]. For universal *quantum* computation, one extra operation in the gate set is required, e.g. the T-gate ($\pi/8$ phase rotation).

2.4.2 Error correction and feedback

The distinction between Clifford operations and non-Clifford operations in logical quantum systems is particularly important when considering the correction of detected errors[6,26,27]. Clifford operations map Pauli operators to Pauli operators. In QEC by stabilizer measurements, errors on the data qubits are projected to single Pauli

operations on the data qubits or the logical qubit. Therefore, in a quantum circuit containing only Clifford gates projected errors only toggle the classical interpretation of the final measurement outcome[6]. The classical information on the detected errors does not need to be available during the execution of the circuit as all information can be retrieved classically afterwards, according to the Gottesmann-Knill theorem[25].

This is not the case when considering universal fault-tolerant quantum computations. Non-Clifford operations map Pauli operations to Clifford operations[6,28]. If a quantum circuit contains non-Clifford operations, as required for universal quantum computations, detected errors propagate to Clifford operations that can not be classically corrected afterwards. Feedback is required to anticipate the detected errors, updating the Pauli frame. If an error is not corrected, future quantum operations can be affected and the error can propagate to complicated multi-qubit errors[6,26].

The process of the collection and interpretation of the error syndrome by stabilizer measurements may only be delayed by a constant amount of time[6,29]. If the processing to determine the updated Pauli frame is relatively slow, due to ancilla measurements and classical processing, one can continue performing stabilizer measurements protecting the qubits[29]. The delay should not result in a lower rate in error processing than the error detection rate as this leads to an increasing delay with respect to the computation[6].

2.5 Characterization of QEC

The goal of QEC is to realize a quantum processor that enables scalable universal quantum computing[30]. Reaching a break-even point for which a quantum processor with QEC realizes longer life times than any of the individual components is challenging as it requires a high level of performance in all elements. To characterize the performance of a quantum error correction protocol, figures of merit can be determined. Here, we will discuss the figures of merit that are used in the following chapters of this thesis.

2.5.1 Process fidelity

In QEC an arbitrary unknown quantum state should be protected during quantum computations. To succesfully protect such arbitrary quantum information, the process of a full QEC cycle should preserve the quantum state. Taking into account anticipated rotations of the Pauli frame, the process fidelity to the identity process χ_{00} on the expected final state is an important figure of merit. This is a measure of how well an arbitrary quantum state is protected against errors.

Following the definition of process tomography by Nielsen and Chuang[4], the process fidelity to the identity process is a function of the state fidelities of the six eigenstates

of the (logical) Pauli operators (X, Y and Z):

$$\chi_{00} = F_p = \frac{1}{4}(F_z + F_{-z} + F_x + F_{-x} + F_y + F_{-y} - 2) \tag{2.1}$$

where F_α is the state fidelity to the state $|\alpha\rangle$. When encoded in a logical quantum state, F_α is the logical state fidelity.

When characterizing the full QEC protocol by the process fidelity, it is difficult to separate state preparation and measurement (SPAM) errors from the actual process. To do so, other methods of characterization are required. The characterization of individual gate performances can for example be done by means of randomized benchmarking[31] or gate-set tomography[32,33]. The reliability of the stabilizer measurements in the detection of errors can be verified by the error syndrome detection as discussed in the next section.

2.5.2 Error syndrome detection

In the experimental implementation of QEC, the error syndrome detection and stabilizer measurement outcomes can be analyzed as function of error probability to verify the reliability of the error correction protocol. In this section we will discuss the characterization of stabilizer measurements on logical encoded states in three, four and five qubits, their expected dependency on the error probability and consequences of deviation from the theoretical expectations.

Errors on the data qubits are detected by measurement of a stabilizer operator that does not commute with the error operation: the measurement outcome switches sign ('clicks'). The stabilizer measurement outcomes can be characterized by analyzing the detection probability as a function of the error probability p_e. If only a single data qubit is affected by errors, the error detection probability of a non-commuting stabilizer measurement is theoretically linear in the error probability p_e. When errors occur simultaneously and with equal probability on all data qubits, protocol-dependent characteristics are obtained.

Theoretically, any stabilizer measurement outcome should be symmetric around $p_e = 0.5$. At $p_e = 0.5$ the encoded information is fully mixed, all information is erased and each stabilizer measurement can give both outcomes with equal probability. The probability that no error is detected ('no click') by any of the stabilizer measurements is therefore 1 over the number of possible error syndromes, e.g. for five qubits that is 1/16.

Assymmetry in the error-detection probability around $p_e = 0.5$ implies extra coherent rotations on the logical state. These rotations complicate the interpretation of the fidelity of the QEC code, and should be taken into account in the analysis. Assymmetry in the ancilla readout as well as initial errors in the logical state transform the error-detection curves symmetrically around $p_e = 0.5$. These values can be characterized in

initialization experiments and taken into account in simulating expected error-detection dependence for verification (Ch. 5).

In three-qubit QEC (Sec. 2.3.1), each stabilizer measurement is expected to detect an error ('click') with probability:

$$p_{\text{click}} = 2p_{\text{one error}} + 2p_{\text{two errors}} \tag{2.2}$$
$$= 2(p_e - p_e^2), \tag{2.3}$$

while the probability that none of the stabilizers detects an error ('no click') is

$$p_{\text{no click}} = p_{\text{no error}} + p_{\text{three errors}} \tag{2.4}$$
$$= 1 - 3(p_e - p_e^2). \tag{2.5}$$

Both curves are shown in Fig. 2.4a.

In the four-qubit error detection protocol (discussed in detail in Ch. 6) the probability that a stabilizer measurement 'clicks' (Fig 2.4b) becomes:

$$p_{\text{click}} = 2p_{\text{one error}} + 2p_{\text{three errors}} \tag{2.6}$$
$$= 4p_e - 12p_e^2 + 16p_e^3 - 8p_e^4. \tag{2.7}$$

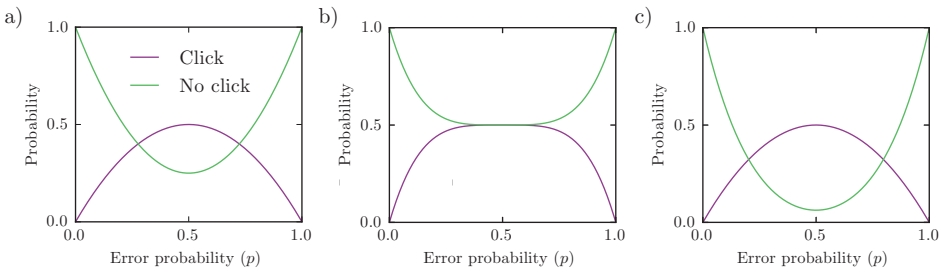


Figure 2.4 — Theoretical probability for a stabilizer measurement to detect an error ('click'), or for no detected errors ('no click') in three protocols for equal error probability on all data qubits in the encoding. For all protocols, at $p_e = 0.5$ the states are fully mixed, all information is erased and the probability that no error is detected is 1 over the number of possible syndromes. The probability for a stabilizer measurement to 'click' is 0.5, corresponding to a fully mixed state. Note that the curves do not nescessarily add up to one as we characterize detection curves for individual stabilizer measurements. **a**, For a three-qubit QEC protocol. **b**, For a four-qubit error-detection protocol. **c**, For a five-qubit QEC protocol.

Finally, for the five-qubit QEC protocol, the probability that a stabilizer measurement 'clicks' is (Fig 2.4c):

$$p_{click} = 2p_{\text{one error}} + 6p_{\text{two errors}} + 6p_{\text{three errors}} + 2p_{\text{four errors}} \tag{2.8}$$

$$= 2p_e + 4p_e^2 - 18p_e^3 + 18p_e^4 - 6p_e^5. \tag{2.9}$$

Experimental analysis of such error detection probability gives insight in the error detection fidelity[34,35] and possible assymmetries in the stabilizer measurements (Ch. 5). Furthermore, these curves can serve as verification to the behaviour expected by the initialization and detection fidelities. However, such experiments do not take into account the fidelity of the projected state after such stabilizer measturements, which can be characterized by process tomography or other characterization methods.

2.6 Conclusion

In this chapter I have given an overview of quantum error correction that is relevant to the work presented in this thesis. In the error-correction protocols I discussed, a logical qubit is protected by redundant encoding in multiple data qubits. Errors are detected and corrected by stabilizer measurements. Inevitable quantum errors are continous and are discretized to single-qubit rotations around the X, Y and Z-axes by these stabilizer measurements.

The smallest code to detect and correct for quantum errors is the three-qubit code. The experimental implementation of this code based on spins in diamond at room-temperature is presented in Ch. 4, where stabilizer measurements and extra ancilla qubits are circumvented by decoding the logical qubit to a single data qubit, which leaves the quantum state unprotected during the error correction. In Ch. 5 we present the experimental implementation of multiple rounds of quantum error correction by stabilizer measurements and real-time feedback, facilitated by non-destructive single-shot readout and long coherence times of the ancilla qubit at cryogenic temperatures.

In the three-qubit code, single-qubit errors around a single axis on the data qubits in the encoding are corrected and detected. To correct for general errors, a mimimum of five data qubits is required. A scalable quantum system requires fault-tolerance: a gate design in which errors do not cascade. In Ch. 6 a detailed proposal for the implementation of such a protocol with spins in diamond is given.

2.7 Bibliography

[1] W. K. Wootters and W. H. Zurek. A single quantum cannot be cloned. *Nature* **299**, 802 (1982).

[2] P. W. Shor. Scheme for reducing decoherence in quantum computer memory. *Physical Review A* **52**, R2493 (1995).

[3] A. M. Steane. Error Correcting Codes in Quantum Theory. *Physical Review Letters* **77**, 793 (1996).

[4] M. Nielsen and I. L. Chuang. *Quantum computation and quantum information.* Cambridge University Press, Cambridge (2000).

[5] N. D. Mermin. *Quantum computation and quantum information.* Cambridge University Press, Cambridge (2007).

[6] B. M. Terhal. Quantum Error Correction for Quantum Memories. *Reviews of Modern Physics* **87**, 307 (2015).

[7] J. Preskill. Reliable quantum computers. *Proceedings of the Royal Society of London A: Mathematical, Physical and Engineering Sciences* **454**, 385 (1998).

[8] D. Gottesman. An Introduction to Quantum Error Correction and Fault-Tolerant Quantum Computation. *arXiv:0904.2557 [quant-ph]* (2009).

[9] S. J. Devitt, W. J. Munro and K. Nemoto. Quantum error correction for beginners. *Reports on Progress in Physics* **76**, 076001 (2013).

[10] E. Knill. Quantum computing with realistically noisy devices. *Nature* **434**, 39 (2005).

[11] A. G. Fowler, D. Sank, J. Kelly, R. Barends and J. M. Martinis. Scalable extraction of error models from the output of error detection circuits. *arXiv:1405.1454 [quant-ph]* (2014).

[12] R. Laflamme, C. Miquel, J. P. Paz and W. H. Zurek. Perfect Quantum Error Correcting Code. *Physical Review Letters* **77**, 198 (1996).

[13] C. H. Bennett, D. P. DiVincenzo, J. A. Smolin and W. K. Wootters. Mixed State Entanglement and Quantum Error Correction. *Physical Review A* **54**, 3824 (1996).

[14] D. G. Cory *et al.* Experimental Quantum Error Correction. *Physical Review Letters* **81**, 2152 (1998).

[15] E. Knill, R. Laflamme, R. Martinez and C. Negrevergne. Benchmarking Quantum Computers: The Five-Qubit Error Correcting Code. *Physical Review Letters* **86**, 5811 (2001).

[16] J. Chiaverini *et al.* Realization of quantum error correction. *Nature* **432**, 602 (2004).

[17] P. Schindler *et al.* Experimental Repetitive Quantum Error Correction. *Science* **332**, 1059 (2011).

[18] M. D. Reed *et al.* Realization of three-qubit quantum error correction with superconducting circuits. *Nature* **482**, 382 (2012).

[19] G. Waldherr *et al.* Quantum error correction in a solid-state hybrid spin register. *Nature* **506**, 204 (2014).

[20] T. H. Taminiau, J. Cramer, T. v. d. Sar, V. V. Dobrovitski and R. Hanson. Universal control and error correction in multi-qubit spin registers in diamond. *Nature Nanotechnology* **9**, 171 (2014).

[21] P. W. Shor. Fault-tolerant quantum computation. *Proceedings of the 37th IEEE Symposium on foundations of computer science* (1996).

[22] D. Gottesman. A Theory of Fault-Tolerant Quantum Computation. *Physical Review A* **57**, 127 (1998).

[23] A. G. Fowler. Towards Large-Scale Quantum Computation. *arXiv:quant-ph/0506126* (2005).

[24] B. Eastin and E. Knill. Restrictions on Transversal Encoded Quantum Gate Sets. *Physical Review Letters* **102**, 110502 (2009).

[25] D. Gottesman. The Heisenberg Representation of Quantum Computers. *Proceedings of the XXII International Colloquium on Group Theoretical Methods in Physics* pp 32–43 (1999).

[26] A. J. Landahl, J. T. Anderson and P. R. Rice. Fault-tolerant quantum computing with color codes. *arXiv:1108.5738 [quant-ph]* (2011).

[27] E. Dennis, A. Kitaev, A. Landahl and J. Preskill. Topological quantum memory. *Journal of Mathematical Physics* **43**, 4452 (2002).

[28] D. Gottesman and I. L. Chuang. Demonstrating the viability of universal quantum computation using teleportation and single-qubit operations. *Nature* **402**, 390 (1999).

[29] D. P. DiVincenzo and P. Aliferis. Effective Fault-Tolerant Quantum Computation with Slow Measurements. *Physical Review Letters* **98**, 020501 (2007).

[30] Y. Tomita and K. M. Svore. Low-distance surface codes under realistic quantum noise. *Physical Review A* **90**, 062320 (2014).

[31] E. Knill *et al.* Randomized Benchmarking of Quantum Gates. *Physical Review A* **77** (2008).

[32] D. Greenbaum. Introduction to Quantum Gate Set Tomography. *arXiv:1509.02921 [quant-ph]* (2015).

[33] S. T. Merkel *et al.* Self-consistent quantum process tomography. *Physical Review A* **87**, 062119 (2013).

[34] D. Nigg *et al.* Quantum computations on a topologically encoded qubit. *Science* 1253742 (2014).

[35] A. D. Córcoles *et al.* Demonstration of a quantum error detection code using a square lattice of four superconducting qubits. *Nature Communications* **6**, 6979 (2015).

Chapter 3

The Nitrogen-Vacancy centre as quantum node

J. Cramer

In this chapter I will outline the relevant physical principles of the NV centre and its nuclear spin environment as well as the relevant building blocks of the experiments described in this thesis. First, I introduce the NV centre, focussing on its electronic and optical properties (Sec. 3.1). Next, I discuss the spin bath surrounding the NV centre. I introduce detection and control of single ^{13}C nuclear spins as qubits in Sec. 3.4. Finally I describe the relevant experimental methods that are applied throughout this thesis (Sec 3.5).

3.1 The NV centre in diamond

The Nitrogen Vacancy (NV) centre (Fig. 3.1) is a lattice defect in the diamond crystal lattice. A nitrogen atom (N) and a vacancy (V) substitute two adjacent diamond lattice sites (Fig. 3.2). In its neutral charge state (NV^0) this results in five unbound valence electrons (three from the carbon atoms, two from the nitrogen atom). The work in this thesis is based on the negatively charged NV^- state (for simplicity further denoted as NV), capturing one extra electron from the environment.

The NV centre is a promising platform for numerous applications including quantum information[1]. Its optical properties as single emitter have been applied in a wide range of quantum communication implementations such as quantum entanglement[2] and quantum teleportation[3] over macroscopic distances. The magnetic coupling of nuclear spins in the diamond lattice to the electron spin of the NV centre, allows to control these spins as individual quantum bits with long coherence times[4–7]. In this thesis I will mainly focus on this quantum register of nuclear spins.

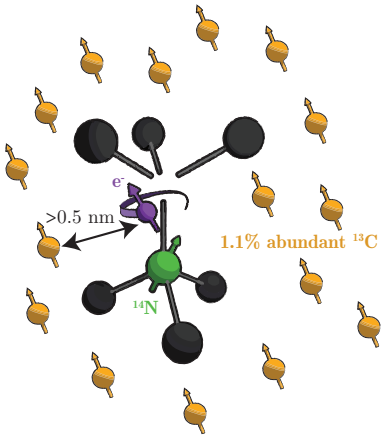


Figure 3.1 — Schematic image of the NV centre in diamond. The NV centre consists of a nitrogen atom (green) and an adjacent vacancy in the diamond lattice, resulting in a $S = 1$ electronic spin state (purple). The NV centre is mainly surrounded by spinless ^{12}C isotopes (black) in the diamond lattice. There is a 1.1% natural abundance of ^{13}C spins in the diamond lattice, which can be individually addressed via the NV electron spin.

3.2 Optical properties of the NV electron spin

The six valence electrons of the NV ground state occupy the molecular orbital levels as shown in Fig 3.2b. Spin-spin interactions lift the degeneracy of the electronic ground and excited state to a spin-triplet ($S = 1$) ground state ($a_1'^2 a_1^2 e^2$, $^3A_2$) and excited state ($a_1'^2 a_1^1 e^3$, ^3E) and multiple intermediate singlet levels. Upon optical excitation an electron can be transferred from the a_1 orbital to one of the e orbitals. The $^3A_2$ to ^3E transitions lie in the optical regime (1.945 eV, $\sim$ 637 nm) and are well within the diamond bandgap (5.5 eV, Fig. 3.2c).

An externally applied magnetic field along the NV axis introduces spin-dependent energy-level splittings in the optical ground and excited states. The $E'_{m_s=\pm1}$ levels and the $A_{1,2}$ split according to their $m_s = \pm1$ spin character while the $E_{x,y}$ ($m_s = 0$) are insensitive to the magnetic field, see Fig. 3.3b. The fine-structure of the energy levels in the optically excited state (^3E) are sensitive to strain[8,9] and magnetic field[9]. To first order, an externally applied electric field can induce crystal strain, splitting the levels as shown in Fig. 3.3c. For a more detailed review I refer to Doherty *et al.*[9] and Hensen[8].

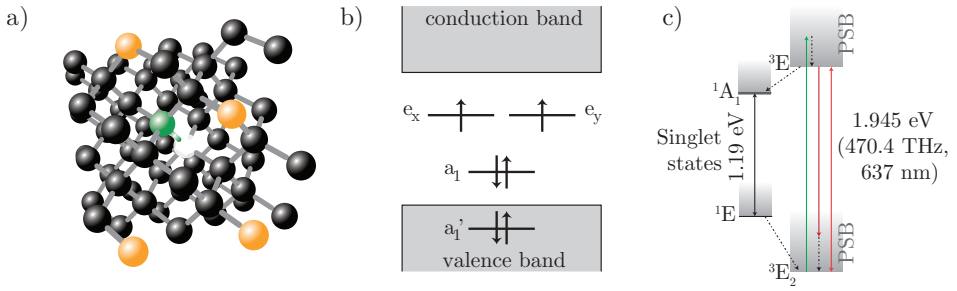


Figure 3.2 — Diamond crystal structure, electronic and optical properties of the NV centre. a, The NV centre is a defect in diamond, formed by a nitrogen atom (green) and an adjacent vacancy in the diamond lattice. This configuration results in 5 valance electrons. For the NV^- electronic ground state an extra electron is captured from the environment, resulting in a spin-1 system. There is a natural abundance (1.1%) of ^{13}C spins (orange) in the diamond lattice. **b**, The valence electrons in the NV^- ground state occupy the molecular orbitals in the electronic ground state of NV^-, following Pauli's exclusion principle. **c**, Electronic and optical properties of the NV centre. The electronic ground state is the spin-triplet with ^3A symmetry (triple degeneracy) and can be optically excited to the six excited states (^3E). Excitation and relaxation occur either resonantly or via the phonon-sideband (PSB), direct or via the singlet states, relaxation can go directly or via the singlet state. Figures adapted from Hensen[10], Gali[11] and Bernien[12].

3.2.1 Room-temperature optical addressing of the NV centre

At ambient conditions, the spin-triplet ground- and excited states of the NV centre are addressed off-resonantly (with laser light of $\lambda \approx 532$ nm) via the phonon-sideband. The NV centre either decays via ^3E to $^3A_2$ by emission of a photon, or (primarily non-radiatively) via one of the singlet-states between the ground and excited state (Fig. 3.3b).

The metastable spin-singlet states equally decay to all spin-levels[13], while the passage into the singlet-state is strongly spin-dependent: the coupling to the singlet states is stronger for the $m_s = \pm 1$ energy levels. Optical excitation into the phonon-sideband thus results in a spin-dependent photon-emission rate. The spin state of the NV centre can therefore be detected through the spin-dependent photo-luminescence rate[9,14] and will eventually result in initialization in the $m_s = 0$ spin state.

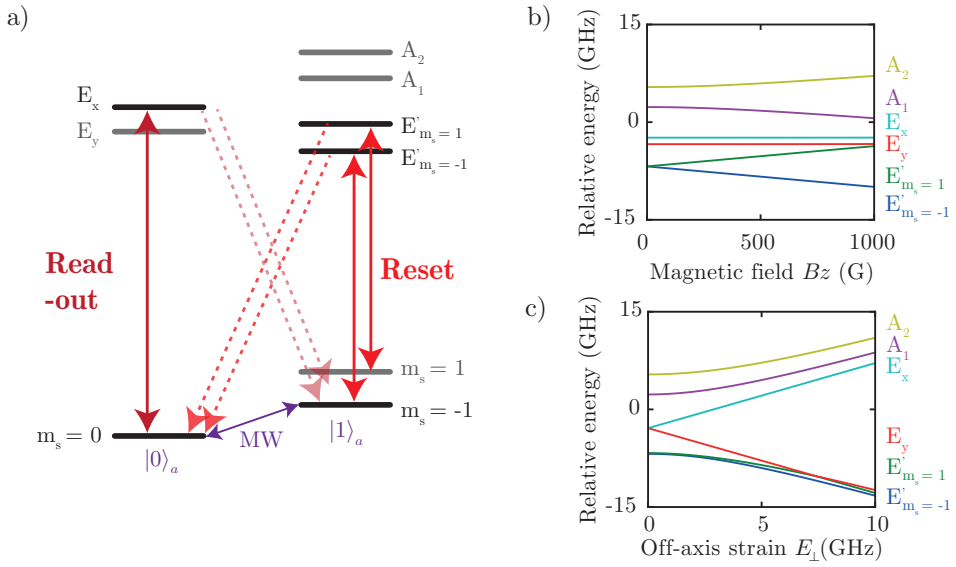


Figure 3.3 — The optical ground and excited state of the NV centre. **a**, The optical transitions used to resonantly read out and initialize (reset) the NV electron spin state. Solid lines indicate spin-preserving optical cycling, dashed arrows indicate non-spin-conserving decay. An AC current (MW) is used to control the electron spin state. **b**, Off-axis strain ($E_\perp$) dependence of the (^3E) excited state of the NV centre for $B_z = 20$ G. **c**, Magnetic-field dependence of the (^3E) excited state of the NV centre for 1 GHz strain. The energy-levels split conform their spin-character.

3.2.2 Fine-structure optically excited state

At cryogenic temperatures (~ 4 K) the optical transitions of the NV centre can be resonantly addressed[13,15]. The transitions from the three $^3A_2$ ground state levels to the six energy levels in the ^3E optically excited state can be resolved (Fig. 3.3), and spin-selectively addressed. These optical transitions are addressed in multiple ways in our experiments:

- Charge and resonance check: to verify if the NV centre is in the negative charge state NV^- and to verify if the laser frequencies are in resonance with the desired optical transitions.
- Initialization: the NV electron spin is initialized in the $m_s = 0$ state by resonantly exciting the $m_s = \pm 1$ optical levels to spin pump the population to the $m_s = 0$ spin state.
- Single-shot readout: Resonant excitation to readout the NV electron spin state in a single shot. The single-shot readout is similar to the initialization, resonantly exciting either the $m_s = 0$ or $m_s = \pm 1$ optical transitions. Due to optical cycling, photons are detected when the excited spin state is occupied. To avoid uncontrolled spin-flips due to spin mixing in the optically excited state, the readout can be stopped right after the detection of a photon.

Charge and resonance check

Before each experiment based on resonant excitation of the NV centre, it is verified if the NV centre is in the correct charge state (NV^-) and if the lasers used for initialization and readout are in resonance with the desired transitions (Fig. 3.4). During this charge and resonance (CR) check two red lasers are simultaneously turned on while the fluorescence is monitored. The number of detected photons is highest when one laser frequency is in resonance with a transition of the $m_s = 0$ ground state to an optically excited state, and one laser with a transition of the $m_s = \pm 1$ states to an optically excited state. Due to slight spin-mixing in the excited state, the NV electron spin would polarize in the opposite state if only one of the lasers is in resonance (Fig. 3.3a) and fluorescence would only be observed for the (NV^-) charge state.

When the number of detected photons is below a set threshold, two methods can be used to optimize the settings:

- When the CR check fails during an experimental run, a green (~ 532 nm) laser can repump the NV centre to its negatively charged state NV^- by exciting trapped charges in the environment. The green excitation furthermore induces spectral diffusion (variation in the optical energy transitions) as it affects the

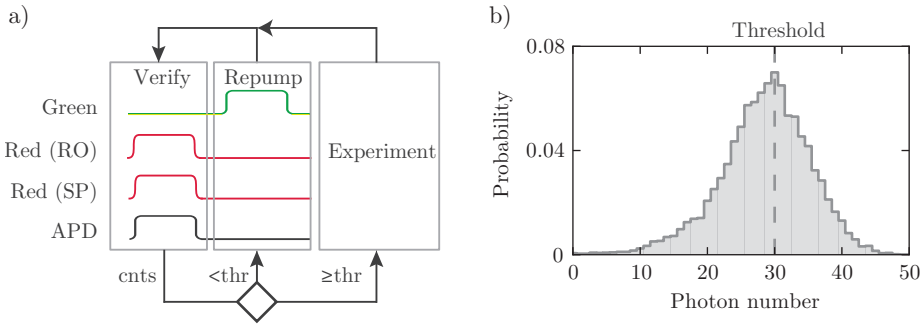


Figure 3.4 — Charge and resonance check, prior to experiment. **a**, Before each experimental sequence the charge and resonance check determines if the lasers are in resonance with the readout (RO) and spin pumping (SP) transitions as well as if the NV centre is in the negative (NV^-) charge state. **b**, Example of a photon number distribution during the CR check verification stage, conditioned on passing the previous CR check. Figure from Blok[16].

charge configuration in the NV environment, which causes a variation in the local electric field. If this effect is undesired, a 575 nm laser could be used to resonantly excite to the NV^- state[10].

- The laser frequencies can be adapted to find the optimal configuration (highest photo-luminescence rate) and thus the exact resonances. This is usually done before starting a set of experimental runs, to fine-tune to the optimal configuration.

Single-shot readout and initialization

We use the $m_s = 0$ optical transition to the optical excited level E_x or E_y (Fig. 3.3) to read out the electronic spin state. Due to spin-mixing in the excited state, continuous optical cycling causes uncontrolled spin-flips in the excited state, eventually pumping the spin-population to the $m_s = \pm 1$ spin states. To minimize this mechanism, for non-destructive readout of the electron spin, we can use a weak readout pulse and switch off the laser within ≈ 2 μs after a photon is detected[6].

The spin-mixing mechanism in the excited state is used to our advantage in initializing to the $m_s = 0$ state. By exciting the $m_s = \pm 1$ optical transition to $E'_{x,y}$ uncontrolled spin-flips in the excited state eventually pump the spin-population to the $m_s = 0$ spin state and thus initialize the electron spin in a well-defined state.

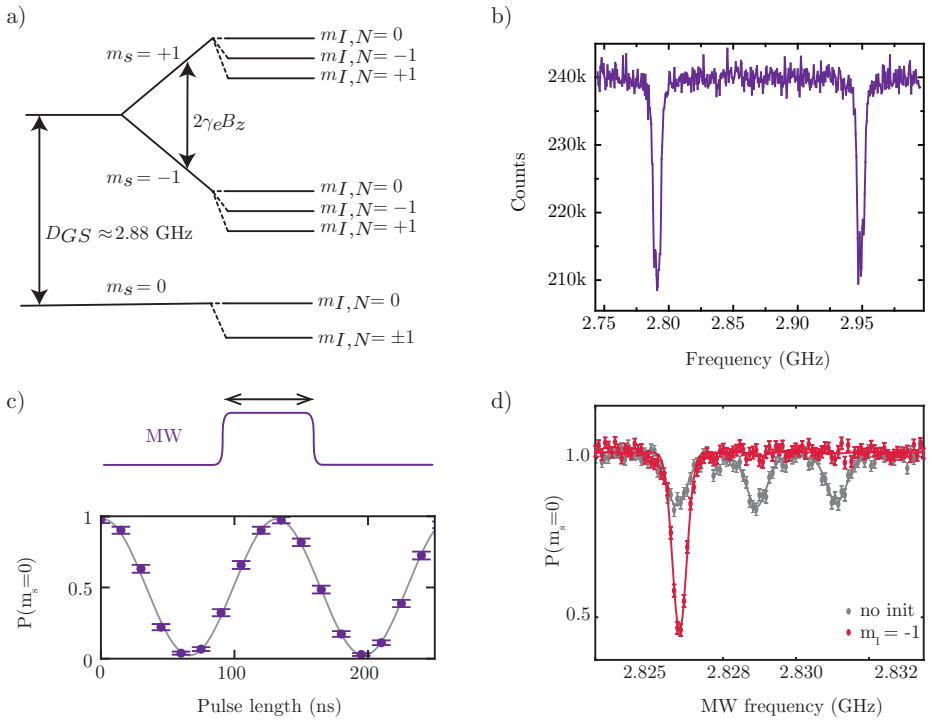


Figure 3.5 — NV electron spin manipulation. **a**, The ground state spin levels of the electron are split by the ground state splitting D_{GS} and the degeneracy of $m_s = \pm 1$ is lifted by an external magnetic field along the z-axis of the NV centre. The interaction of the NV electron spin to its nitrogen spin further splits the energy levels according to Eq. 3.2. **b**, Continuous-wave (CW) electron spin resonance experiment. Integrated photon detection obtained for CW green excitation, varying the frequency of CW AC current. The two observed dips correspond to the $m_s = 0 \leftrightarrow m_s = -1$ and the $m_s = 0 \leftrightarrow m_s = +1$ transitions. **c**, Coherent control of the electron spin as qubit is realized by varying the length of a microwave pulse in resonance with the desired electron spin transition. The solid line is a fit from which the Rabi frequency is determined (7.67 ± 0.02 MHz). **d**, Pulsed electron spin resonance experiment on the $m_s = 0 \leftrightarrow m_s = -1$ transition. The transition energy is dependent on the host nitrogen spin state. The nitrogen spin can be initialized in a defined spin state by a conditional rotation of the electron spin, followed by a measurement of the electron spin. Here, the red data-points show a pulsed electron spin resonance experiment after initialization of the nitrogen spin in $m_{I,N} = -1$. Figure adapted from De Lange[17] and Blok[16].

3.3 Properties of the ground state NV electronic spin state

In the orbital ground state of the NV centre, the $m_s = 0$ and $m_s = \pm 1$ spin levels are separated by the zero-field splitting $D_{GS} \approx 2.88$ GHz. The $m_s = \pm 1$ level degeneracy is lifted by an externally applied magnetic field $\mathbf{B} = B_x\hat{x} + B_y\hat{y} + B_z\hat{z}$ via the Zeeman interaction, see Fig. 3.5. The resulting Hamiltonian, neglecting strain-interaction and second-order spin-orbit interactions, is given by[9,18,19]:

$$H_e = D_{GS}S_z^2 + \gamma_e \mathbf{B} \cdot \mathbf{S}, \tag{3.1}$$

with $\mathbf{S} = S_x\hat{x} + S_y\hat{y} + S_z\hat{z}$ the Pauli spin matrices for a spin-1 system and $\gamma_e = 2.8025$ MHz/G the gyromagnetic ratio.

The electron spin levels in the orbital ground state are manipulated using electron spin resonance techniques[9,20,21]. To control the NV electron spin as a qubit, we choose two out of the three electron spin levels as our qubit states ($|0\rangle, |1\rangle$). An AC current at a frequency resonant with the energy difference between the addressed spin levels causes an oscillating magnetic field, resulting in coherent oscillations between these qubit states (Fig. 3.5a,c). Qubit rotation angles are chosen by calibrating amplitude and length of the applied microwave (MW) pulse.

3.3.1 The nitrogen host spin

The NV centres used in the experiments discussed in this thesis are based on a nitrogen atom of the most common isotope ^{14}N (natural abundance 99.64%), a spin-1 system[9,22]. The Hamiltonian for the electron-nitrogen system in the orbital ground state is[19]:

$$H_{e,N} = H_e - QI_{N_z}^2 + \gamma_n \mathbf{B} \cdot \mathbf{I_N} - A_\parallel S_z I_{N_z} - A_\perp (S_x I_{N_x} + S_y I_{N_y}), \tag{3.2}$$

with S_i, I_{N_i} the i-component of the spin-1 operators of the electron (S_i) and nitrogen (I_{N_i}) spins, $Q = 4.98$ MHz the quadrupolar splitting of the nitrogen spin, $\gamma_n = 0.3077$ kHz/G the nitrogen spin gyromagnetic ratio and $A_\parallel = 2.16$ MHz ($A_\perp = 2.1$ MHz) the parallel (perpendicular) component of the hyperfine interaction. As the electronic spin transitions are far off-resonant from the nuclear spin transitions in our experimental settings, we apply the secular approximation and the flip-flop terms (containing $S_x I_x$ and $S_y I_y$) can be neglected.

The hyperfine interaction $A_\parallel$ introduces a splitting of the electron spin transitions, that can be resolved in electron spin resonance experiments (Fig. 3.5d). In previous work, the nitrogen spin has been successfully used as a qubit, that can be initialized, controlled and read out[4]. In the work of this thesis the nitrogen spin is initialized by mapping its spin state on the electron spin and subsequent readout of the electron (Fig. 3.5d).

3.3.2 Electron spin coherence

The NV electron spin is a long-lived quantum system, with its dominant source of errors caused by dephasing[21,23]. The phase-coherence is strongly dependent on the microscopic environment of the NV centre. In bulk diamond, where the defect is relatively far from the diamond surface, the dominant source of decoherence for the electron spin are the nuclear spins in the spin bath[21,24]. These spins cause a fluctuating magnetic field, affecting the energy level splitting of the electron spin and thus leading to dephasing on a timescale T_2^*. The dephasing time T_2^* is measured through a Ramsey experiment as shown in Fig. 3.6a. The dephasing time is, depending on the studied NV centre and its environment, typically in the order of several μs and can be extended by isotopically purifying the diamond sample[7,16,25].

The electron spin phase coherence can be protected by making it insensitive to quasi-static fluctuations of the spin bath by dynamical decoupling techniques[21]. The spin state is periodically inverted by regularly spaced π-pulses, resulting in a repeated sequence of the form $\tau - \pi - 2\tau - \pi - \tau$. The signal revives for $\tau = k\tau_L$ with k an integer, $\tau_L = 2\pi/\omega_L$ and ω_L the Larmor frequency of the nuclear ^{13}C spins. Using decoupling pulses with symmetrized alternating phases (e.g. $XY8$) we correct for pulse errors[21,26]. Figure 3.6b shows that, by increasing the number of pulses up to 2048, a coherence time of $T_{DD} = 0.37(1)$ s can be obtained[24]. These long coherence times allow for high fidelity control in the work presented in this thesis.

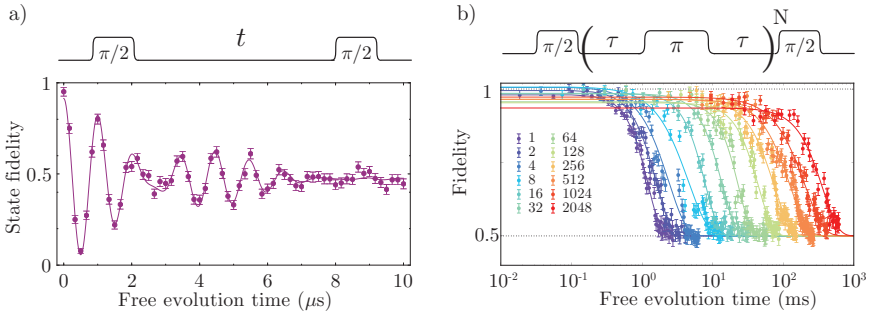


Figure 3.6 — Electron coherence in Ramsey type experiment and under dynamical decoupling. a, The electron dephasing time T_2^* is measured in a Ramsey experiment where a superposition state freely precesses for time t. The dephasing time of this NV centre is $T_2^* = 4.6(2)$ μs. The beating in the signal is caused by the coupling to a close-by ^{13}C nuclear spin with a hyperfine coupling strength of 191(5) kHz. The host nitrogen spin is initialized in this experiment. **b**, Figure from Bakker[24]. Dynamical decoupling of the NV electron spin, fidelity versus free evolution time t with number of decoupling pulses varied from 1 to 2048. Solid lines are fits to $F = 0.5 + A\exp[-(t/T_{DD})^n]$.

3.4 Weakly coupled spins as qubits in a quantum register

While the NV electron spin is mainly surrounded by spinless ^{12}C atoms, there are nuclear ^{13}C spins in its environment. In the diamond samples used in the presented work, there is a 1.1% natural abundance of ^{13}C spin-$\frac{1}{2}$ nuclear spins (Fig. 3.1). Each NV centre is therefore surrounded by a unique spin bath, which is mainly responsible for the dephasing of the electron spin (Sec. 3.3.2). The implementation of dynamical decoupling on the electron spin extends the electron spin coherence time[21] and is the basis of the detection and control of individual ^{13}C nuclear spins in the spin bath. These nuclear spins have long coherence times[7,18,24] and can be individually controlled as quantum bits[4,27].

The work presented in this thesis is based on a quantum register of weakly coupled ^{13}C spins in the environment of the NV centre. The detection and control methods are based on the work by Taminiau *et al.*[5]. Here, I will discuss the interaction Hamiltonian, the detection, characterization and control of these ^{13}C nuclear spins as individual qubits.

3.4.1 Interaction Hamiltonian

The ^{13}C spins considered here are not resolved in spin-resonance experiments on the NV electron spin; the linewidth of an ESR experiment is much larger than the hyperfine interaction between the electron and ^{13}C spin ($\sqrt{2}/(\pi T_2^*) \ll |A|$). Due to the relatively large distance between the NV electron spin and the nuclear spins, we neglect the contact hyperfine interaction[19] such that only the dipolar coupling plays a role in the interaction between the NV electron spin and a single ^{13}C spin, which with appropriate basis rotation becomes:

$$H_{e,N,C} = H_{e,N} + \gamma_c \mathbf{B}\cdot\mathbf{I_C} + \frac{\mu_0\gamma_e\gamma_c\hbar}{4\pi r^3}[\mathbf{S}\cdot\mathbf{I}_C - 3(\mathbf{S}\cdot\hat{r})(\mathbf{I}\cdot\hat{r})], \tag{3.3}$$

where $\mu_0 = 4\pi \times 10^{-7}$ N/A^2 is the vacuum permeability, $\gamma_C = 1.0705$ kHz/G the gyromagnetic ratio of ^{13}C nuclear spins and $\mathbf{r}$ the relative position of the nuclear spin with respect to the NV centre.

Following the secular approximation and choosing the xz-plane such that $\mathbf{r} = \sin(\theta)\hat{x} + \cos(\theta)\hat{z}$, we obtain:

$$\begin{aligned} H_{e,N,C} &= H_{e,N} + \gamma_c \mathbf{B}\cdot\mathbf{I_C} + \frac{\mu_0\gamma_e\gamma_c\hbar}{4\pi r^3}[(1-3\frac{z^2}{r^2})S_zI_z - 3\frac{|x|z}{r^2}S_zI_x] \\ &= H_{e,N} + \omega_L I_z + A_\parallel S_z I_z + A_\perp S_z I_x \end{aligned} \tag{3.4}$$

where ω_L is the Larmor frequency of the ^{13}C nuclear spin in the applied magnetic field (assumed in z-direction) and $\mathbf{A} = A_\perp\hat{x} + A_\parallel\hat{z}$ the hyperfine interaction between the nuclear spin and the NV electron spin. The ^{13}C spin Hamiltonian can now be

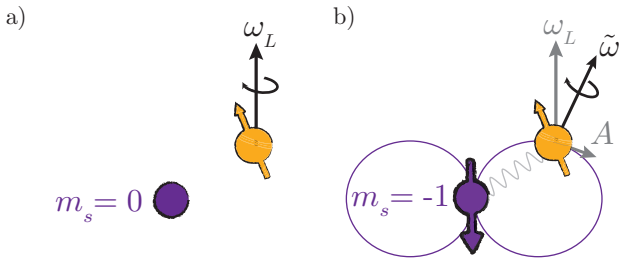


Figure 3.7 — Effect of hyperfine interaction between NV electron spin (purple) and ^{13}C nuclear spin (orange). a, When the electron spin state is $m_s = 0$, the nuclear spin precesses around an axis parallel with the magnetic field with precession frequency $\omega_L = \gamma_C B_z$, the dipolar interaction is effectively turned off. **b**, When the electron spin state is $m_s = -1$, the hyperfine interaction between the electron spin and the nuclear spin effectively tilts the ^{13}C rotation axis to $\boldsymbol{\omega} = \boldsymbol{\omega}_L + \mathbf{A}$ and thus changes the frequency ($\tilde{\omega} = \sqrt{(\omega_L - A_\parallel)^2 + A_\perp^2}$). (For the electron spin in $m_s = +1$, the parallel component of the hyperfine interaction ($A_\parallel$) switches sign.)

written as:

$$H_C = |m_s = 0\rangle \langle m_s = 0| H_0 + |m_s = -1\rangle \langle m_s = -1| H_{-1} + |m_s = +1\rangle \langle m_s = +1| H_{+1} \tag{3.5}$$

with m_s the electron spin state and

$$H_0 = \omega_L I_z, \tag{3.6}$$

$$H_{\pm 1} = (\omega_L \pm A_\parallel) I_z \pm A_\perp I_x. \tag{3.7}$$

The Hamiltonian H_0 is only dependent on the externally applied magnetic field, while $H_{\pm 1}$ are dependent on the parallel and perpendicular terms of the hyperfine interaction, as follows from Eq. 3.4 (see Fig. 3.7).

3.4.2 Detection and characterization of nuclear spins

Nuclear spins in the spin bath of a NV centre are detected and characterized by dynamical decoupling of the NV electron spin. Each NV centre in diamond is surrounded by a unique local environment of ^{13}C spins because each nuclear spin is probabilistically located in the diamond lattice, resulting in a ^{13}C-dependent hyperfine interaction $\mathbf{A}$.

The spin-dependent hyperfine interaction results in spin-dependent resonant interaction to the NV electron spin under dynamical decoupling. When decoupling the electron spin between the $m_s = 0 \leftrightarrow m_s = -1$ spin states, the ^{13}C nuclear spin

evolution operators corresponding to a NV decoupling unit ($\tau - \pi - 2\tau - \pi - \tau$) that are conditional on the initial electron input state can be described by:

$$V_0 = \exp[-iH_0\tau]\exp[-iH_{-1}2\tau]\exp[-iH_0\tau], \tag{3.8}$$
$$V_1 = \exp[-iH_{-1}\tau]\exp[-iH_0 2\tau]\exp[-iH_{-1}\tau]. \tag{3.9}$$

These evolution operators can be written as single-qubit rotations:

$$\begin{aligned} V_0 &= \exp[-i\phi(\mathbf{I}\cdot\hat{\mathbf{n}}_{\mathbf{0}})], \\ V_1 &= \exp[-i\phi(\mathbf{I}\cdot\hat{\mathbf{n}}_{-\mathbf{1}})], \end{aligned} \tag{3.10}$$

where $\hat{\mathbf{n}}_{\mathbf{m_s}}$ is the rotation axis dependent on the initial spin state of the electron spin (m_s). These rotation axes are dependent on the decoupling time τ (Fig. 3.8) allowing us to design desired operations on the nuclear spins by choosing appropriate τ, N for the decoupling sequences.

The local environment of ^{13}C spins is first detected by dynamical decoupling while sweeping τ [5,28,29]. We prepare the NV electron spin in an equal superposition of two spin states, e.g. in $|x\rangle = \frac{1}{\sqrt{2}}(|0\rangle + |1\rangle)$ with $|0\rangle = |m_s = 0\rangle$ and $|1\rangle = |m_s = -1\rangle$. The electron is then decoupled by $N/2$ repetitions of a decoupling unit ($\tau - \pi - 2\tau - \pi - \tau$) and finally the x-component of the electron spin qubit is measured, see Fig. 3.9b. Sharp periodic resonances in the obtained signal correspond to coherent interaction between the electron spin and individual ^{13}C spins in the spin bath (Fig. 3.9b).

The interaction of the NV electron spin with a single nuclear spin results in a dynamical decoupling spectroscopy signal given by:

$$S(\tau, N) = \mathrm{Re}\{\mathrm{Tr}[U_0 U_{-1}]\} \tag{3.11}$$

with $U_{m_s} = V_{m_s}^{N/2}$. Taking n ^{13}C nuclear spins into account, only assuming interaction to the electron spin, the signal results in [5]:

$$S(\tau, N) = \prod_{j=0}^{n} S_j(\tau, N) \tag{3.12}$$

where $S_j(\tau, N)$ is the signal if spin j would be the only ^{13}C spin in the environment of the NV electron spin.

The decoupling signal S for varying τ and N reveals information on the hyperfine coupling parameters $\mathbf{A}_j$ for individual nuclear spins. The experimentally obtained signal can be reconstructed by simulations to estimate the hyperfine coupling parameters of nuclear spins in the NV electron spin environment (see Fig. 3.10).

For $|A_\perp| \ll \omega_L$ the X and Z components of the rotation axes $\hat{\mathbf{n}}_{\mathbf{0}}$ and $\hat{\mathbf{n}}_{\mathbf{1}}$ show sharp resonances in τ, where the nuclear spin undergoes an X-rotation which can be

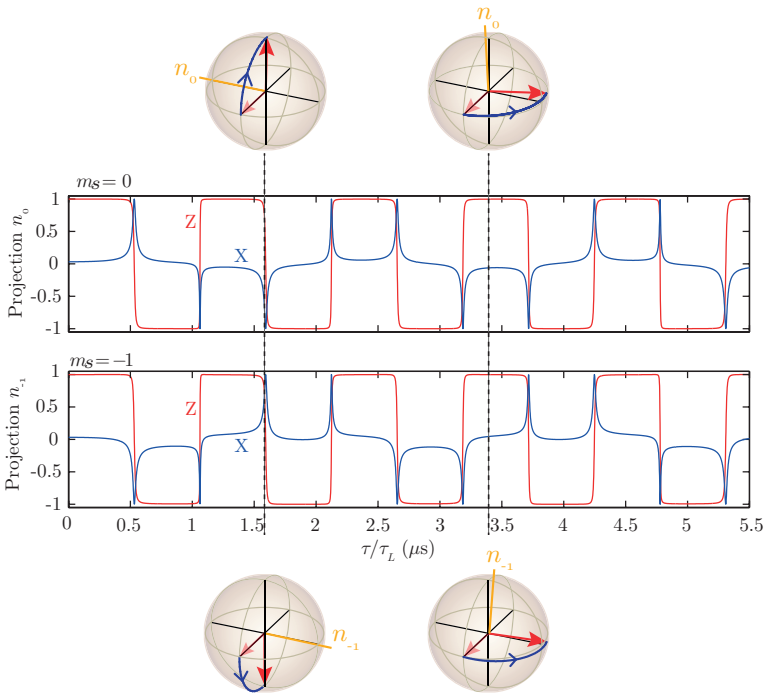


Figure 3.8 — Example of nuclear dynamics for a single ^{13}C spin interaction with the electron spin. The X and Z projections of the net rotation axes $\mathbf{n_0}$ ($\mathbf{n_{-1}}$) of the nuclear spin for dynamical decoupling on the NV electron spin, initially starting in $m_s = 0$ ($m_s = -1$). The first dashed section and connected Bloch spheres show an effective conditional rotation of the nuclear spin. The second dashed section indicates a τ-value for which the nuclear spin undergoes a simple Z-rotation independent on the electron spin state.

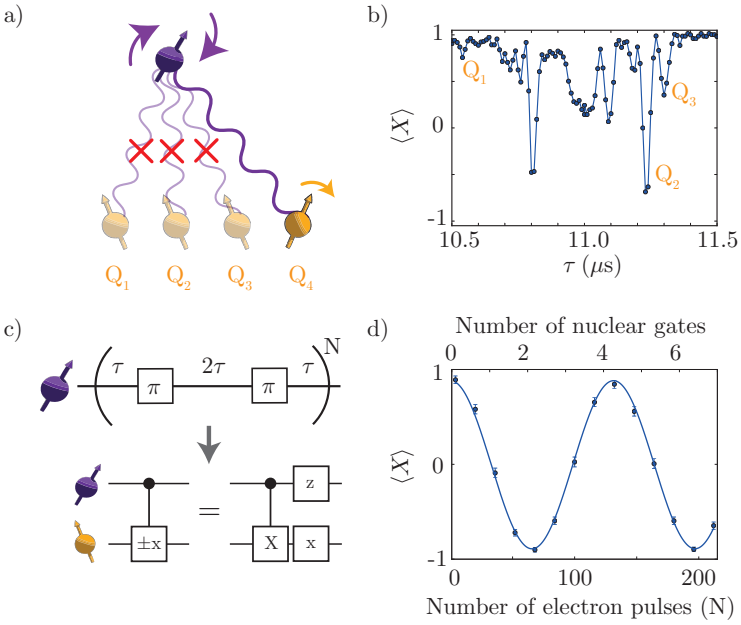


Figure 3.9 — Detection and control of single ^{13}C spins in the spin bath of the NV electron spin. **a**, Decoupling the electron spin at specific decoupling times τ results in effective dynamical decoupling of the NV electron spin from the spin bath, while enhancing the interaction to a single ^{13}C in the bath, allowing for selective operations on individual nuclear spins. **b**, Data for varying τ in a decoupling experiment with $N = 32$ pulses on the electron state $|x\rangle$. The sharp resonances indicate interaction to a single ^{13}C spin (3 spins are pointed out here). **c**, Example of a gate on a single ^{13}C spin, implemented via the NV electron spin. For repeated decoupling elements with τ in resonance with the hyperfine interaction to the addressed nuclear spin, a controlled operation on this spin is performed: a $\pi/2$ rotation around the $\pm x$ axis dependent on the initial electron spin state. **d**, Varying the number of pulses (N) on the electron spin on such a resonance results in coherent oscillations of the nuclear spin, indicated by coherent oscillations of $\langle X \rangle$ of the electron spin.

conditional or unconditional on the initial state of the electron spin. In dynamical decoupling spectroscopy, at such resonance, the signal S for a single nuclear spin coherently oscillates dependent on N (Eq. 3.11). At other values of τ the nuclear spin undergoes a simple unconditional Z-rotation (Fig. 3.8).

3.4.3 Control and operations

The resonant interaction between the NV electron spin and single ^{13}C nuclear spins is employed to control these nuclear spins individually as qubits. This requires for initialization, control and readout of the individual nuclear spins.

Operations on nuclear spins are obtained by dynamical decoupling of the NV electron spin. In most (τ, N)-configurations, dynamical decoupling results in an unconditional Z-rotation of the nuclear spins (Fig. 3.8). The rotation frequency is calibrated and tracked throughout experiments for each individual spin. When the rotation axes (Eq. 3.10) of a single nuclear spin $\hat{n}_{m_s} = n_x\hat{x} + n_z\hat{z}$ fulfill the condition $n_x > n_z$, (un)conditional rotations of this nuclear spin to the equator plane can be obtained. The exact resonance condition ($n_z = 0$) occurs periodically. The nuclear spin evolution is approximated by the rotation matrix:

$$R_{\hat{n}}(\theta) = \begin{bmatrix} \cos(\theta/2) - i\sin(\theta/2)n_z & \mp i\sin(\theta/2)n_x \\ \mp i\sin(\theta/2)n_x & \cos(\theta/2) + i\sin(\theta/2)n_z \end{bmatrix}, \tag{3.13}$$

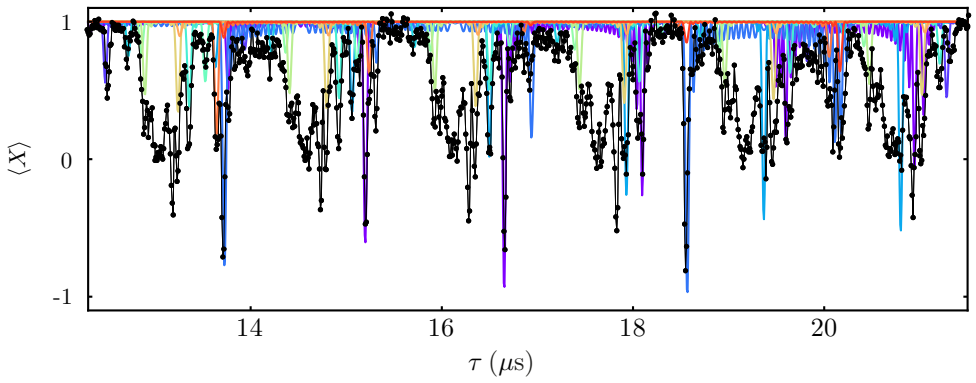


Figure 3.10 — Detection of single ^{13}C spins by dynamical decoupling spectroscopy. Data (black lines and datapoints) for varying τ in a decoupling experiment with $N = 32$ pulses on the electron state $|x\rangle$. The sharp resonances indicate interaction to a single ^{13}C spin. The 13 colored lines are estimated signals for the interaction between a single ^{13}C spin and the NV electron spin. The estimated hyperfine interactions are based on a larger dataset than shown here.

with θ dependent on the number of pulses N. A universal set of gates on a nuclear spin requires rotations around the Z-axis and operations that take the computational states $|0\rangle$ and $|1\rangle$ to two orthogonal states in the equator plane. Following Eq. 3.13, this requires $|n_x| > 1/\sqrt{2}$.

Initialization and readout of the nuclear spin state, as well as correlation measurements on multiple ^{13}C states are obtained by employing controlled operations between the electron and nuclear spins. The evolution of nuclear spins is dependent on the electron spin state, but insensitive to optical excitation of the NV electron (Ch. 4), as long as the NV electron spin state is known throughout the full experiment. This allows for preservation of the nuclear spin state under non-destructive readout of the NV electron spin state. In Chs. 4,5 initialization and readout of the nuclear spins will be discussed in detail.

3.5 Experimental methods

The experimental work presented in this thesis covers both experiments at room-temperature and cryogenic temperature. In the confocal microscope setup at room-temperature (Fig. 3.12), diamond samples are characterized[12,16] and experiments as discussed in Ch. 4 are performed. At liquid helium temperatures ($\sim$ 4 K), the NV electron spin can be non-destructively read out in a single-shot, a key ingredient for the experiments discussed in Ch. 5. In Fig. 3.13 the experimental setup for such experiments is shown.

3.5.1 Diamond samples

The work in this thesis is based on NV centres in high-purity type IIa CVD-grown diamond. The sample used in the experiments described in Ch. 4 has a $\langle 100 \rangle$ crystal orientation, while the experiments of Ch. 5 are performed on a $\langle 111 \rangle$ crystal oriented diamond, with the advantage that an NV centre with the N-V axis perpendicular to the diamond surface plane can be selected. The diamond samples are supplied by *Element Six*. An example image of such a sample, processed for our experimental purposes, is shown in Fig. 3.11.

Fabrication on the diamond samples is required for our experimental purposes. A detailed description of the processing is given by Bernien[12]. After detecting and selecting 6-10 NV centres in a characterization setup, solid-immersion lenses (SILs) are fabricated around the NV locations, by milling away diamond by a focussed ion beam (FIB, Fig. 3.11a). This enhances the collection efficiency of the NV emission by reducing the total internal reflection (Fig. 3.11b). To further enhance the collection efficiency an anti-reflective coating[3] is deposited on the surface of the sample used in Ch. 5.

By electron-beam lithography, a gold stripline is fabricated over the surface of the

diamond sample, closely passing the fabricated SILs. Via this stripline, AC currents to control the electron spin state are applied. Gold gate-electrodes are fabricated near the NV centres to apply static electric fields, allowing to tune the strain in the NV-centre, fine-tuning the NV optical resonances[10,12]. These gates are not used in this work.

3.5.2 Experimental spin control

The NV electron spin state is controlled by AC currents applied in resonance with the electron spin level transitions ($m_s = 0 \leftrightarrow m_s = +1$ and $m_s = 0 \leftrightarrow m_s = -1$) both in pulsed and continuous-wave experiments (Fig. 3.5). The AC currents are generated by (*Rohde and Schwartz SMBV100A*) vector sources. Pulse sequences are generated on an arbitrary waveform generator (AWG, *Tektronix AWG5014*), controlling frequency, amplitude and phase of the pulses by IQ- and pulse-modulation. Electron Rabi frequencies in the order of MHz are typically obtained (Fig. 3.5).

In the experiments described in this thesis a moderate magnetic field of a few hundred Gauss is applied along the NV z-axis. For a sample with $\langle 100 \rangle$ crystal orientation a three-coil water-cooled vector magnet is used, allowing for tilted magnetic fields. A sample with $\langle 111 \rangle$ crystal orientation is used in experiments at cryogenic temperatures. A permanent magnet placed on *Attocube* ANPxyz101-steppers (range $\sim 5 \times 5 \times 5$ mm^3) is used to align the required magnetic field.

3.5.3 Resonant readout and initialization - cryogenic temperatures

At cryogenic temperatures the electron spin levels can be resonantly addressed, allowing for high-fidelity (non-destructive) single-shot readout of the electron spin state. The

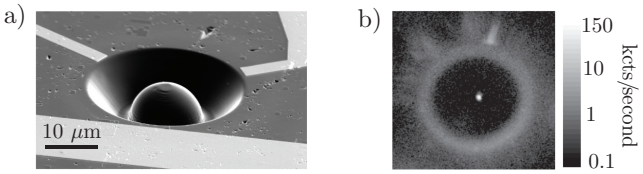


Figure 3.11 — Electron and confocal microscope image of the surface of a diamond sample after fabrication for experimental purposes. **a**, Scanning electron-microscope image of a solid-immersion lens (SIL) in the diamond surface. Close to the SIL there are a gold stripline for applying AC pulses to control the NV electron spin state and gold gates to apply DC voltages. **b**, Scanning confocal microscope image of the SIL with green laser light. The bright spot shows the emission of the NV centre in the PSB. Figure taken from Bernien[12].

readout, initialization and charge-resonance check require two red lasers (~ 637 nm) in resonance with optical transitions of the electron spin. A green laser (~ 532 nm) is used to initialize the NV centre in the NV^- state. A schematic of the setup is shown in Fig. 3.13.

In the Janis bath cryostat used for the low-temperature experiments described in this thesis, the sample is placed on *Attocube* ANPxyz101-steppers (range $\sim 5 \times 5 \times 5$ mm^3) and the objective on *Attocube* ANSxyz50-scanners (range $\sim 30 \times 30 \times 4.3$ μm^3), allowing for precision alignment of the NV centre in the optical path.

3.5.4 Real-time feedback

In experiments with sequential measurements such as quantum error correction, real-time updates of the experimental sequence are desired. Dependent on a measurement outcome, the upcoming gates can be adapted, for example to correct for detected errors. This effectively branches the experiment in multiple paths.

In the experiments presented in this thesis, such branching and real-time updates are implemented employing the AWG and ADwin. The pulse-sequences are pre-programmed in the AWG, including specific elements corresponding to different branches. After a measurement, the ADwin analyses the measurement outcome ('click' or 'no click') and sends a 'event-jump' trigger to the AWG for one of the outcomes. The AWG continues to its next sequence element when no trigger was received, or 'jumps' to the preprogrammed corresponding sequence element.

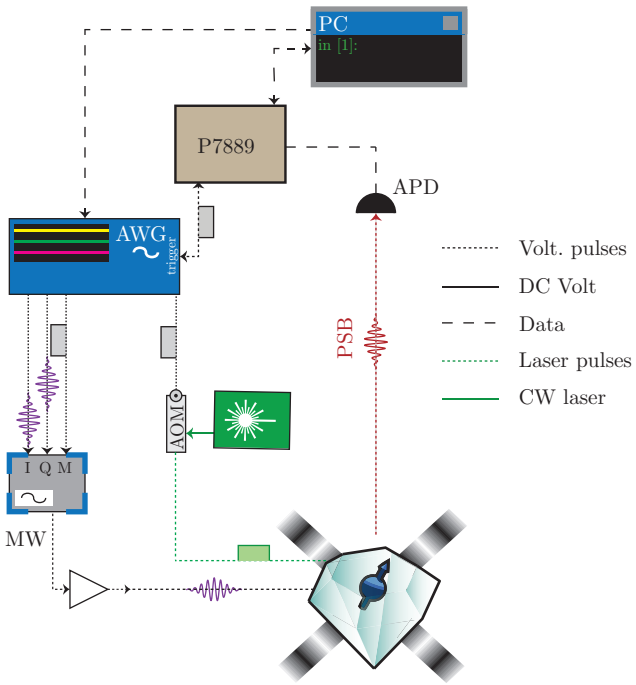


Figure 3.12 — Schematic of confocal microscope setup and electronics to control spins in diamond at room temperature. A green (532 nm) laser modulated by an acousto optical modulator (AOM), is used to excite the NV centre, emitted light in the phonon-sideband (PSB, red) is detected via an avalanche photo diode (APD) and a fast counter (P7889). The AWG provides the IQ and digital modulation of the microwave source, whose output is amplified before the signal is sent to the sample. A vector magnet allows for flexibility in the orientation of the magnetic field. Figure adapted from De Lange[17] and Pfaff[30].

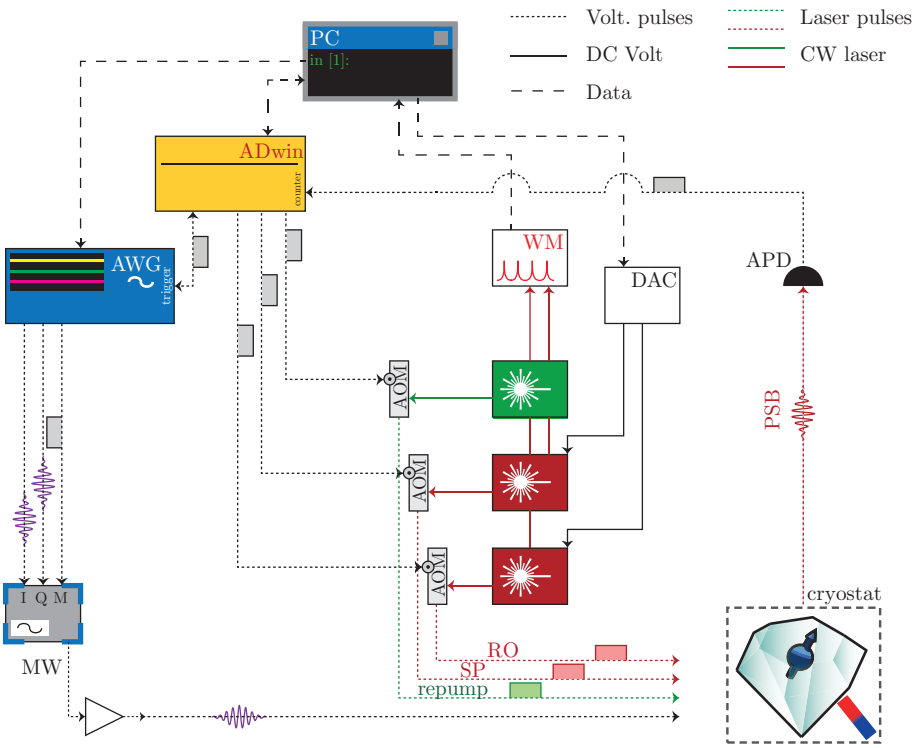


Figure 3.13 — Schematic of measurement and control setup at cryogenic temperatures. A PC programs the control loop on a integrated micro-controller (*ADwin*) and pulse sequences on an arbitrary waveform generator (AWG; *Tektronix AWG 5014*). Sequences on the AWG are triggered from the ADwin, and the AWG notifies the ADwin when sequences are completed. The ADwin generates laser pulses for charge re-pumping (repump), electron spin pumping (SP), and electron spin readout (RO) via accousto-optical modulators. Laser frequencies are monitored with a wave meter (WM, *Highfinesse WS6*), and controlled using DAC modules on the frequency modulation inputs of the lasers. Laser power is modulated using acousto optical modulators (AOMs). Microwave pulses are generated by a vector source (*Rohde & Schwarz SMBV100A*). The AWG controls frequency and timing of these pulses via IQ- and pulse modulation. Spin manipulation signals are amplified (*Amplifier Research 20S1G4* or *40S1G4*) before feeding to the sample. Phonon-sideband (PSB) is detected with an avalanche photodiode (APD). Detection events are registered by the counting module of the ADwin. Figure adapted from Pfaff[30].

3.6 Bibliography

[1] L. Childress and R. Hanson. Diamond NV centers for quantum computing and quantum networks. *MRS Bulletin* **38**, 134 (2013).

[2] B. Hensen *et al.* Loophole-free Bell inequality violation using electron spins separated by 1.3 kilometres. *Nature* **526**, 682 (2015).

[3] W. Pfaff *et al.* Unconditional quantum teleportation between distant solid-state quantum bits. *Science* **345**, 532 (2014).

[4] T. van der Sar *et al.* Decoherence-protected quantum gates for a hybrid solid-state spin register. *Nature* **484**, 82 (2012).

[5] T. H. Taminiau *et al.* Detection and Control of Individual Nuclear Spins Using a Weakly Coupled Electron Spin. *Physical Review Letters* **109**, 137602 (2012).

[6] M. S. Blok *et al.* Manipulating a qubit through the backaction of sequential partial measurements and real-time feedback. *Nature Physics* **10**, 189 (2014).

[7] P. C. Maurer *et al.* Room-Temperature Quantum Bit Memory Exceeding One Second. *Science* **336**, 1283 (2012).

[8] B. Hensen. *Measurement-based quantum computation with the nitrogen-vacancy centre in diamond.* MSc Thesis, Delft, University of Technology (2011).

[9] M. W. Doherty *et al.* The nitrogen-vacancy colour centre in diamond. *Physics Reports* **528**, 1 (2013).

[10] B. Hensen. *Quantum nonlocality with spins in diamond.* PhD Thesis, Delft, University of Technology (2016).

[11] A. Gali, M. Fyta and E. Kaxiras. Ab initio supercell calculations on nitrogen-vacancy center in diamond: Electronic structure and hyperfine tensors. *Physical Review B* **77**, 155206 (2008).

[12] H. Bernien. *Control, measurement and entanglement of remote quantum spin registers in diamond.* PhD Thesis, Delft, University of Technology (2014).

[13] L. Robledo, H. Bernien, T. v. d. Sar and R. Hanson. Spin dynamics in the optical cycle of single nitrogen-vacancy centres in diamond. *New Journal of Physics* **13**, 025013 (2011).

[14] A. Gruber *et al.* Scanning Confocal Optical Microscopy and Magnetic Resonance on Single Defect Centers. *Science* **276**, 2012 (1997).

[15] L. Robledo *et al.* High-fidelity projective read-out of a solid-state spin quantum register. *Nature* **477**, 574 (2011).

[16] M. S. Blok. *Quantum measurement and real-time feedback with a spin register in diamond*. PhD Thesis, Delft, University of Technology (2015).

[17] G. de Lange. *Quantum control and coherence of interacting spins in diamond*. PhD Thesis, Delft, University of Technology (2012).

[18] F. Jelezko *et al.* Observation of Coherent Oscillation of a Single Nuclear Spin and Realization of a Two-Qubit Conditional Quantum Gate. *Physical Review Letters* **93**, 130501 (2004).

[19] A. Schweiger and G. Jeschke. *Principles of pulse electron paramagnetic resonance*. Oxford University Press, Oxford (2005).

[20] G. D. Fuchs, V. V. Dobrovitski, D. M. Toyli, F. J. Heremans and D. D. Awschalom. Gigahertz Dynamics of a Strongly Driven Single Quantum Spin. *Science* **326**, 1520 (2009).

[21] G. d. Lange, Z. H. Wang, D. Ristè, V. V. Dobrovitski and R. Hanson. Universal Dynamical Decoupling of a Single Solid-State Spin from a Spin Bath. *Science* **330**, 60 (2010).

[22] M. W. Doherty, N. B. Manson, P. Delaney and L. C. L. Hollenberg. The negatively charged nitrogen-vacancy centre in diamond: the electronic solution. *New Journal of Physics* **13**, 025019 (2011).

[23] A. Jarmola, V. M. Acosta, K. Jensen, S. Chemerisov and D. Budker. Temperature- and Magnetic-Field-Dependent Longitudinal Spin Relaxation in Nitrogen-Vacancy Ensembles in Diamond. *Physical Review Letters* **108**, 197601 (2012).

[24] M. Bakker. *Frozen core spin dynamics in diamond*. MSc Thesis, Delft, University of Technology (2015).

[25] G. Balasubramanian *et al.* Ultralong spin coherence time in isotopically engineered diamond. *Nature Materials* **8**, 383 (2009).

[26] Z.-H. Wang, G. de Lange, D. Ristè, R. Hanson and V. V. Dobrovitski. Comparison of dynamical decoupling protocols for a nitrogen-vacancy center in diamond. *Physical Review B* **85**, 155204 (2012).

[27] W. Pfaff *et al.* Demonstration of entanglement-by-measurement of solid-state qubits. *Nature Physics* **9**, 29 (2013).

[28] S. Kolkowitz, Q. P. Unterreithmeier, S. D. Bennett and M. D. Lukin. Sensing Distant Nuclear Spins with a Single Electron Spin. *Physical Review Letters* **109**, 137601 (2012).

[29] N. Zhao *et al.* Sensing single remote nuclear spins. *Nature Nanotechnology* **7**, 657 (2012).

[30] W. Pfaff. *Quantum measurement and entanglement of spin quantum bits in diamond*. PhD Thesis, Delft, University of Technology (2013).

Chapter 4

Universal control and error correction in multi-qubit spin registers in diamond

T. H. Taminiau, J. Cramer, T. van der Sar, V. V. Dobrovitski and R. Hanson

Quantum registers of nuclear spins coupled to electron spins of individual solid-state defects are a promising platform for quantum information processing[1–13]. Pioneering experiments selected defects with favourably located nuclear spins having particularly strong hyperfine couplings[4–10]. For progress towards large-scale applications, larger and deterministically available nuclear registers are highly desirable. Here we realize universal control over multi-qubit spin registers by harnessing abundant weakly coupled nuclear spins. We use the electron spin of a nitrogen-vacancy centre in diamond to selectively initialize, control and read out carbon-13 spins in the surrounding spin bath and construct high-fidelity single- and two-qubit gates. We exploit these new capabilities to implement a three-qubit quantum-error-correction protocol[14–17] and demonstrate the robustness of the encoded state against applied errors. These results transform weakly coupled nuclear spins from a source of decoherence into a reliable resource, paving the way towards extended quantum networks and surface-code quantum computing based on multi-qubit nodes[11,18,19].

The results in this chapter have been published in *Nature Nanotechnology* **9**, 171-176 (2014).

4.1 Introduction

Electron and nuclear spins associated with defects in solids provide natural hybrid quantum registers[3–12]. Fully-controlled registers of multiple spins hold great promise as building blocks for quantum networks[18] and fault-tolerant quantum computing[19]. The defect electron spin enables initialization and readout of the register and coupling to other (distant) electron spins[11,18], whereas the nuclear spins provide well-isolated qubits and memories with long coherence times[8,9,11]. Previous experiments relied on selected defects having nuclear spins with strong hyperfine couplings that exceed the inverse of the electron spin dephasing time ($1/T_2^*$). With these strongly coupled spins, single-shot readout[9,10,20–22] and entanglement[9,11] were demonstrated. However, the number of strongly coupled spins varies per defect and is intrinsically limited, so that universal control has so far been restricted to two-qubit registers[4,7] and the required control of multi-qubit registers has remained an open challenge.

Here we overcome this challenge by demonstrating universal control of *weakly coupled nuclear spins* (unresolved hyperfine coupling $\ll 1/T_2^*$). We use the electron spin of single nitrogen-vacancy (NV) centres in room-temperature diamond to selectively control multiple carbon-13 (^{13}C) nuclear spins in the surrounding spin bath (Fig. 4.1a). With this new level of control we realize multi-qubit registers by constructing high-fidelity unconditional and electron-controlled gates, implementing initialization and readout, and creating nuclear-nuclear entangling gates through the electron spin. Finally, we demonstrate the power of this approach by implementing the first quantum-error-correction protocol with individual solid-state spins.

4.2 Detection and control of weakly coupled nuclear spins in diamond

We have used dynamical decoupling spectroscopy[23–25] to characterize the nuclear spin environment of a total of three NV centres, including one with an additional strongly coupled ^{13}C spin (Fig. 4.5). To demonstrate the generality of our approach to create multi-qubit registers, we have realized initialization, control and readout of three weakly coupled ^{13}C spins for each NV centre studied (Figs. 4.6-4.8). Below we consider one of these NV centres in detail and use two of its weakly coupled ^{13}C spins to form a three-qubit register for quantum error correction (Fig. 4.1a).

Our control method exploits the dependence of the nuclear spin quantization axis on the electron spin state due to the anisotropic hyperfine interaction (see 4.5.2 for hyperfine parameters), so that no radio-frequency driving of the nuclear spins is required[7,23–28] (see Ch. 3). All nuclear gates are implemented by pulse sequences of the form $(\tau-\pi-2\tau-\pi-\tau)^{N/2}$ where π is a microwave pi-pulse on the electron spin, 2τ is the inter-pulse delay and N is the total number of pulses in the sequence. Each nuclear spin is controlled by precisely choosing τ in resonance with that spin's particular

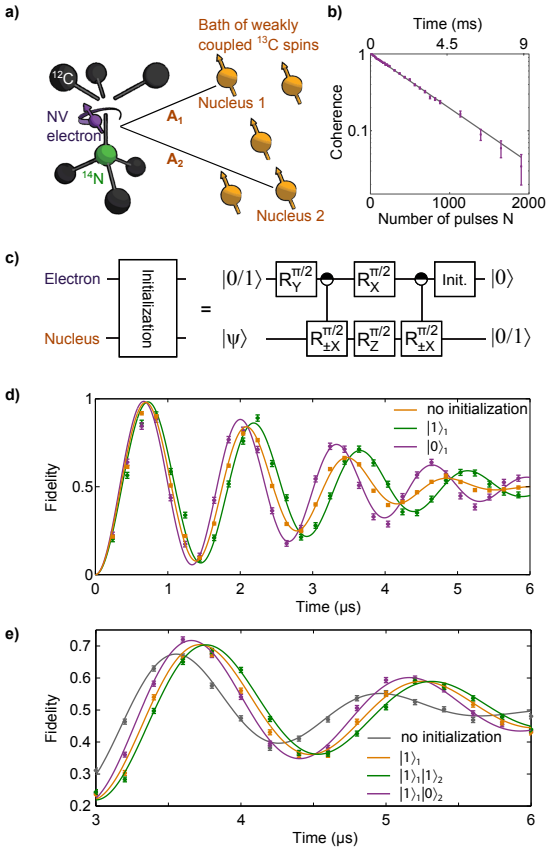


Figure 4.1 — Definition and initialization of the quantum registers. a, Quantum register formed by the nitrogen-vacancy (NV) electron spin ($S = 1$; $|0\rangle = |m_s = 0\rangle, |1\rangle = |m_s = -1\rangle$) and weakly coupled ^{13}C nuclear spins ($I = 1/2$; state $|\psi\rangle_i$ and hyperfine interaction A_i for nuclear spin i, see Sec. 4.5.1 for values). All gates on nuclear spins are implemented by sequences of N pi-pulses on the electron spin spaced by a time 2τ (Sec. 4.5.2). **b**, The electronic coherence as a function of the total sequence length. The number of pi-pulses N is increased for fixed $\tau = 2\pi/\omega_L$, which is representative for our gates. $\omega_L = 2\pi \cdot 431$ kHz is the ^{13}C Larmor frequency. The $1/e$ time is $T_{\text{coh}} = 2.86(4)$ ms. **c**, Nuclear spin initialization by swapping the electron state, $|0/1\rangle = |0\rangle$ or $|1\rangle$, onto the nuclear spin. The controlled gates ($R_{\pm X}^{\pi/2}$) are X-rotations by $\pi/2$ with a direction conditional on the electron spin state (Sec. 4.5.2). The final electron spin re-initialization by a 2 μs laser pulse (labelled "Init.") preserves the nuclear spin polarization (T_1 values under illumination: 2.5(3) ms for nuclear spin 1 and 1.2(2) ms for nuclear spin 2, Fig. 4.25). **d**, Electron Ramsey measurements without nuclear spin initialization and with nuclear spin 1 initialized in $|0\rangle_1$ or $|1\rangle_1$, and **e**, with nuclear spin 1 initialized in $|1\rangle_1$ and nuclear spin 2 in $|0\rangle_2$ or $|1\rangle_2$. All error bars and uncertainties in this work are 1 s.d.

hyperfine interaction. The target spin, the type of gate (conditional or unconditional) and the rotation axis (X- or Z-rotation) are determined by the value of τ; the total rotation angle is determined by N (Sec. 4.5.2). Crucially, these sequences at the same time decouple the electron from the other nuclear qubits and the environment[7]; these decoherence-protected gates are selective and allow the full electron coherence time $T_{\rm coh}$ to be exploited ($T_{\rm coh} = 2.86(4)$ ms, Fig. 4.1b). The gates are thus not limited by the electron spin dephasing time $T_2^* = 3.3(1)$ μs or Hahn echo time T_2 and do not require strong coupling.

To initialize the nuclear spins we first prepare the electron spin in $m_s = 0$ by optical pumping (Sec. 4.6.2), then swap the electron state onto the nuclear spin, and finally re-initialize the electron spin (Fig. 4.1c). We characterize the nuclear initialization by preparing the electron spin in a superposition state and letting it evolve in a Ramsey-type experiment. Without initialization a single-frequency oscillation with a Gaussian decaying envelope is observed, confirming that the NV centre feels a decohering bath of weakly coupled spins (Fig. 4.1d). Initializing the nuclear spins in the $|0\rangle(|1\rangle)$ state (Fig. 4.1d and e), we increase (decrease) the oscillation frequency because the magnetic field at the electron is enhanced (reduced) due to the hyperfine interaction. The oscillations also persist longer as quasistatic fluctuations of the two nuclear spins are suppressed[29], increasing the electronic dephasing time to $T_2^* = 4.0(2)$ μs. Initializing spin 1 has a more pronounced effect because spin 1 has a larger parallel component of the hyperfine interaction ($A_\parallel^1 = 2\pi \cdot 78.2(8)$ kHz) than spin 2 ($A_\parallel^2 = 2\pi \cdot 32(3)$ kHz). From such measurements, we obtain state initialization fidelities of $F_1 = 0.91(2)$ and $F_2 = 0.88(5)$ for nuclear spin 1 and 2 respectively (see 4.5.1).

We next demonstrate the measurement of the individual nuclear spin states and verify that we observe two distinct ^{13}C spins by performing nuclear free-evolution experiments (Fig. 4.2a-d). The oscillations in the expectation values for the X and Y Pauli operators $\langle X\rangle$ and $\langle Y\rangle$ show that the nuclear spins states are successfully read out. The precession frequencies, $\bar{\omega} = 2\pi \cdot 470(1)$ kHz for nuclear spin 1 (Fig. 4.2c) and $\bar{\omega} = 2\pi \cdot 449(2)$ kHz for nuclear spin 2 (Fig. 4.2d), are different and agree with the average of $\omega_0 = \omega_L$ (for $m_s = 0$) and $\omega_1 \approx \omega_L + A_\parallel$ (for $m_s = -1$), as expected because the electron spin is continuously flipped. $\omega_L = 2\pi \cdot 431$ kHz is the bare nuclear Larmor frequency. These results confirm that we selectively address the two targeted weakly coupled ^{13}C spins.

Universal control requires both conditional and unconditional gates, while maintaining a high degree of coherence for all qubits in the register. To characterize our gates, we initialize the nuclear spins, prepare the electron spin either in $m_s = 0$ or in $m_s = -1$ and apply a gate with a variable number of pulses. For the conditional gate, $\langle Y\rangle$ oscillates in anti-phase for the two electron states: the nuclear spin rotates around the X–axis in a direction that depends on the initial electron state (Fig. 4.2e). In contrast, for the unconditional gate the rotation direction is independent of the electron state (Fig. 4.2f). The slow decay of the oscillations indicates that high control

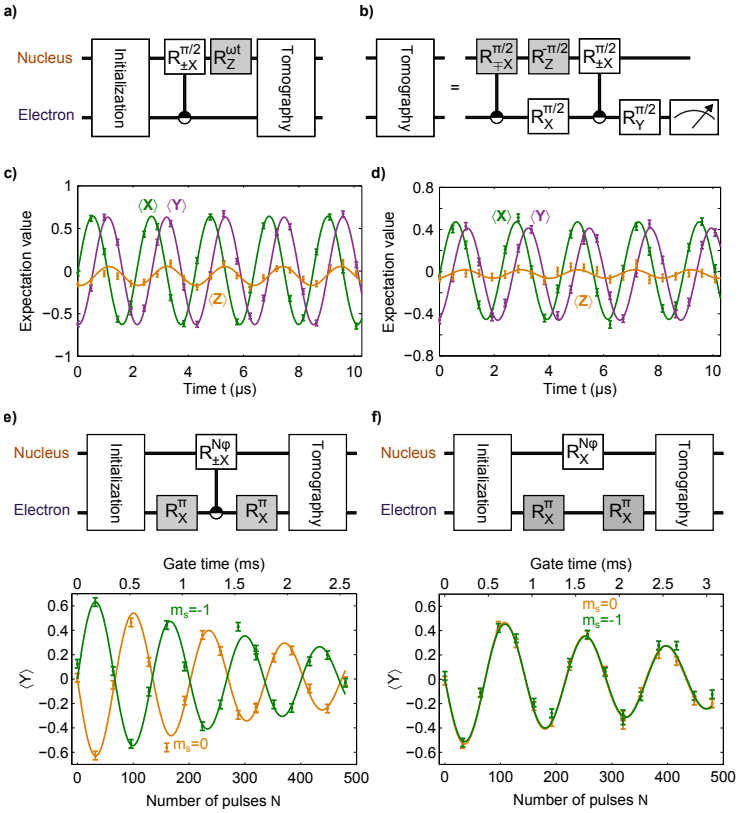


Figure 4.2 — Individual nuclear spin control and readout. **a**, Sequence for nuclear-spin free-precession experiments. The Z-rotation is implemented by a pulse sequence with off-resonant inter-pulse delay (τ=0.12 μs) with a variable number of pulses N. **b**, Nuclear spin state tomography is performed by mapping the expectation values of the Pauli operators $\langle X\rangle$, $\langle Y\rangle$ and $\langle Z\rangle$ onto the electron spin and reading out the electron (shaded gates are optional basis rotations). Note that the signs of the first controlled operation and the phase gate are corrected with respect to the publication. **c-d**, Measurement of $\langle X\rangle$, $\langle Y\rangle$ and $\langle Z\rangle$ as function of the free-evolution time. The oscillations in $\langle X\rangle$ and $\langle Y\rangle$ confirm the selective control and readout of the targeted nuclear spins. The amplitude yields a combined readout and initialization fidelity of 0.82(1) for spin 1 in **c** and 0.72(1) for spin 2 in **d**. Curves are sinusoidal fits. See Figs. 4.6-4.8 for a complete data set with three nuclear spins for each of the three NV centres studied, demonstrating the generality of the control method. **e**, Characterization of the conditional gate for nuclear spin 1. The nuclear spin rotates about the X-axis with opposite directions for $m_s = 0$ (without shaded gates) and $m_s = -1$ (with shaded gates). Time for a $\pm\pi/2$-rotation: 170 μs. **f**, Unconditional gate for nucleus 1; the rotation is independent of the electron state. Time for a $\pi/2$-rotation: 254 μs. See Fig. 4.11 for gates on nuclear spin 2. Results are not corrected for initialization or readout fidelities.

fidelities are possible ($F \sim 0.96$ for a single-qubit nuclear $\pi/2$-rotation), enabling us to explore multi-gate sequences that implement nuclear-nuclear gates and quantum error correction.

To realize quantum gates between the nuclear spins[27,30], whose mutual interaction is negligible, we use the electron spin as a quantum bus. We first verify that both nuclear spins can be prepared and read out in the same experiment by initializing the spins in an eigenstate and performing state tomography by mapping the two-qubit correlations onto the electron spin (Fig. 4.3a). We then implement entangling gates through an electron controlled gate on nuclear spin 2 and a subsequent coherent SWAP gate between the electron and nuclear spin 1 (Fig. 4.2b). The tomography reveals strong correlations between the nuclear spins with near-zero single-qubit expectation values, a clear signature of an entangling gate. Despite the 167 electron operations over 986 μs required to implement the five nuclear X-rotations, the fidelity with the target state is 0.66(3) (initialization and readout corrected), demonstrating that the gate can take a pure input state into an entangled state of nuclear spins.

4.3 Three-qubit error correction

Finally, we implement a quantum-error-correction protocol that protects a quantum state from bit-flip errors by encoding it in a 3-qubit state and correcting errors through majority voting (Fig. 4.4a). Such protocols have been realized with nuclear magnetic resonance[14,15], trapped ions[16] and superconducting qubits[17], but have so far been out of reach for individual solid-state spins due to a lack of multi-qubit control. We compose this protocol from one- and two-qubit gates (Fig. 4.4b) and separately confirm that the constructed doubly-controlled gate flips the state around the X-axis only if the control qubits (nuclear spins) are in $|1\rangle_1 |1\rangle_2$ (Fig. 4.4c).

We first characterize the effect of errors on each qubit individually. The applied errors are rotations around the X-axis by an angle θ with a random sign (50% clockwise, 50% anticlockwise) and therefore represent a decoherence-type process with a strength determined by θ. We prepare 6 input states: $|Z\rangle = |0\rangle$, $|-Z\rangle = |1\rangle$, $|\pm Y\rangle = (|0\rangle \pm |1\rangle)/\sqrt{2}$ and $|\pm Y\rangle = (|0\rangle \pm i\,|1\rangle)/\sqrt{2}$, measure the corresponding fidelities F with the output states and calculate the process fidelity F_p with the identity process:

$$F_p = \frac{(F_x + F_{-x} + F_y + F_{-y} + F_z + F_{-z})}{4} - \frac{1}{2}$$

Without error correction, errors on the data qubit (electron spin) are expected to result in an oscillation about $F_{p0} = (F_x + F_{-x})/4$ because only the $|\pm x\rangle$ states are unaffected by the applied errors. With error correction, however, the experimental process fidelity always remains above $F_{p0} = 0.293(1)$, even for a completely randomizing error ($\theta = \pi/2$), indicating that the state is partly recovered (Fig. 4.4d). If one of the ancilla qubits (nuclear spins) is also flipped, an oscillation about F_{p0} is observed; the error

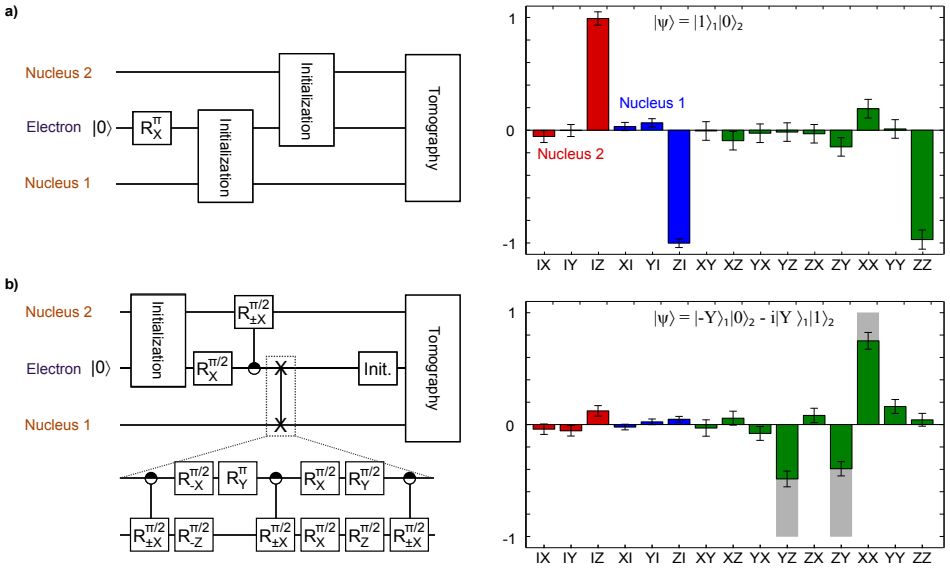


Figure 4.3 — Two-qubit control and nuclear-nuclear entangling gate. **a**, The nuclear spins are prepared in $|1\rangle_1 |0\rangle_0$ and two-qubit tomography is performed by mapping the 15 combinations of the identity and Pauli operators onto the electron spin (Sec. 4.6.2). After correction for single-qubit initialization and readout fidelities by renormalizing to the maximum values in Fig. 4.2c and 2d, the state fidelity with the target state is $F = 0.99(3)$, indicating that the sequential initialization and two-qubit readout are accurate. **b**, Entangling gate between nuclear spins by coherently swapping the state of the electron onto nuclear spin 1. The nuclear spin coherence is preserved during electron spin re-initialization (a 2 μs laser pulse); T_2^* values under illumination are 51(7) μs and 0.35(9) ms for nuclear spin 1 and 2 respectively (Sec. 4.6.7). The grey bars depict the target state. Note that the target state in the original publication[31] missed a phase.

correction is effectively turned off because the protocol cannot correct two-qubit errors.

To quantitatively determine the effectiveness of the error correction we analyze it in terms of the three probabilities p_n that an applied error on qubit n is successfully corrected and a decoherence/depolarization process during the error-correction protocol itself (Sec. 4.5.4). The model accurately fits the data and gives $p_1 = 0.89(2)$, $p_2 = 0.63(1)$ and $p_3 = 0.84(2)$ for errors on nucleus 1, the electron and nucleus 2 respectively. Crucially, the average probability $\langle p_n \rangle = (p_1 + p_2 + p_3)/3 = 0.786(9)$ is well above 2/3, demonstrating that the process is robust against applied single-qubit errors and that the entropy associated with the errors is successfully shuttled to the ancilla qubits.

We further demonstrate the robustness by applying errors simultaneously on all three qubits (Fig. 4.4e). Without error correction, i.e. without doubly-controlled gate, a linear dependence is observed and a fit to the expected form gives $\langle p_n \rangle = 0.67(3)$ in excellent agreement with $\langle p_n \rangle = 2/3$ expected for no robustness to errors. With error correction a markedly slower initial decay and a non-linear behaviour with $\langle p_n \rangle = 0.84(3)$ is obtained. This suppression of the linear dependence is a key characteristic of quantum error correction.

The deviation from $\langle p_n \rangle = 1$ is mainly due to imperfect nuclear initialization, which might be improved by repeated initialization steps (Fig. 4.13) or projective measurements[9,21]. We calculate $\langle p_n \rangle = 0.94(2)$ for ideal initialization fidelity (Fig. 4.16). Without applied errors, decoherence and depolarization during the protocol itself (300 electron operations for 10 nuclear spin gates over 1.8 ms) result in a process fidelity of 0.431(2), corresponding to an average decrease of the state fidelity to 0.93 for one gate (Sec. 4.6.5). For only the encoding and decoding steps the process fidelity is 0.728(4). The main source of infidelity is electron decoherence ($T_{\mathrm{coh}} = 2.86(4)$ ms, Fig. 4.1b), which is likely phonon-induced[32] and limits the average fidelity per gate to 0.97. Nuclear spin dephasing further reduces the fidelity to 0.94, close to the observed value (Sec. 4.6.5). The electronic coherence time is greatly increased at cryogenic temperatures, at which $T_{\mathrm{coh}} = 14$ ms (single NV)[18] and $T_{\mathrm{coh}} = 0.6$ s (ensembles)[32] have already been reported. Nuclear spin dephasing can be mitigated by decoupling nuclear-nuclear interactions (T_2 measurements in Fig. 4.23). With such future improvements, our results can be used to protect entangled states of solid-state spins.

4.4 Discussion

In conclusion, we have established universal control over weakly coupled nuclear spins that were previously regarded as a source of decoherence. These results provide multiple qubits per defect with high certainty and are compatible with control of the intrinsic nitrogen spin and potential strongly coupled ^{13}C spins. Our techniques can be applied to a wide variety of other electron-nuclear spin systems[2,3,10,12]. The resulting reliable multi-qubit registers can be combined with recently demonstrated coherent coupling between (distant) electron spins[11,18] to realize novel surface-code quantum-computation architectures that use four qubits per defect node[19] and extended quantum networks for long-distance quantum communication.

4.5 Methods

4.5.1 Diamond sample and hyperfine interactions

We use a room-temperature type IIa diamond with 1.1% of ^{13}C grown by chemical vapor deposition (*ElementSix*). We apply a magnetic field of $B_z \approx 403$ G along the

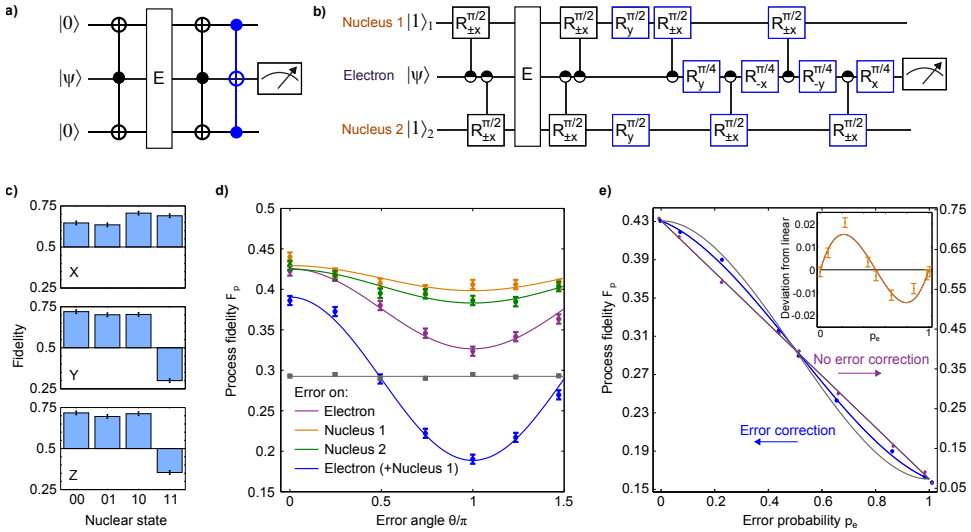


Figure 4.4 — Implementation of 3-qubit quantum error correction. **a**, Bit-flip quantum-error-correction protocol. The state $|\psi\rangle$ is encoded in an entangled state using two ancilla qubits. Potential errors E are detected by decoding and are corrected based on a doubly-controlled NOT gate. **b**, Our implementation of the quantum-error-correction protocol in **a**. The doubly-controlled gate (blue) is constructed using 4 controlled gates as the final ancilla states are irrelevant. The experiment consists of 308 electron operations in 1.8 ms (excluding initialization). **c**, Characterization of the doubly-controlled gate (blue gates in **b** only). The average output fidelities for $|\pm X\rangle$, for $|\pm Y\rangle$ and for $|\pm Z\rangle$ are shown for the four ancilla basis states. The average process fidelity with the targeted action is $F_p = 0.534(5)$. **d**, Process fidelity for errors applied to nucleus 1, to nucleus 2, or to the electron spin (with and without additional flip of nuclear spin 1). Grey data and fit are $F_p 0 = (F_x + F_(- x))/4$, which sets the average value for the expected oscillations if no errors are corrected. **e**, Process fidelity for errors simultaneously applied to all three qubits with error probability p_e. Purple: without error correction. Blue: with error correction. Grey: for ideal robustness against errors. Error bars are given by the symbol size (typical standard deviation 0.002). Inset: deviation of the error correction data from a linear curve. All curves in **d** and **e** are fits to the model in Sec. 4.5.4.

NV symmetry axis (Z-axis), yielding a ^{13}C Larmor frequency $\omega_L = 2\pi \cdot 431$ kHz. The electronic dephasing time T_2^* is 3.3(1) μs. The hyperfine interaction for nuclear spin i is given by $A_i = A_\parallel^i \hat{z} + A_\perp^i \hat{x}$ (Fig. 4.1a), with $A_\parallel$ the component parallel to the magnetic field and $A_\perp$ the perpendicular component. The values determined by dynamical decoupling spectroscopy[23] are $A_\parallel^1 = 2\pi \cdot 78.2(8)$ kHz and $A_\perp^1 = 2\pi \cdot 30(1)$

kHz for nuclear spin 1, and $A_{\parallel}^2 = 2\pi \cdot 32(3)$ kHz and $A_{\perp}^2 = 2\pi \cdot 44(2)$ kHz for nuclear spin 2 (Fig. 4.6). Because $A_{\parallel}, A_{\perp} < (2\sqrt{2})/T_2^* = 2\pi \cdot 136(1)$ kHz the nuclear spins are weakly coupled to the electron spin and the hyperfine splittings are unresolved.

4.5.2 Nuclear gate design

In a suitable rotating frame, the Hamiltonian with a single nuclear spin can be written:

$$\hat{H} = |0\rangle\langle 0|\hat{H}_0 + |1\rangle\langle 1|\hat{H}_1$$

with $\hat{H}_0 = \omega_L \hat{I}_Z$ and $\hat{H}_1 = (\omega_L + A_{\parallel})\hat{I}_Z + A_{\perp}\hat{I}_X$ and with $|0\rangle$ and $|1\rangle$ the $m_s = 0$ and $m_s = -1$ electron states, respectively. Nuclear spin gates are performed by applying sequences of the type $(\tau - \pi - 2\tau - \pi - \tau)^{N/2}$ on the electron spin (Rabi frequency 31.25 MHz). Because we set $\omega_L \gg A_{\perp}$, sharp periodic resonances occur at:

$$\tau \approx k\pi/(2\omega_L + A_{\parallel}), \tag{4.1}$$

with integer k (Sec. 4.6.5). At these values a nuclear X-rotation is performed (assuming $A_{\perp} \neq 0$). For odd k the direction of the rotation is conditional on the electron spin (e.g. the $R_{\pm X}^{\pi}/2$ gates), for even k it is unconditional ($R_X^{\pi/2}$ gates). We use values of k for which the resonances of the different spins do not overlap. For the conditional gates we take $\tau = 2.656$ μs ($k = 5$), $N = 32$ for spin 1 and $\tau = 3.900$ μs ($k = 7$), $N = 18$ for spin 2. For the unconditional gates we use $\tau = 3.186$ μs ($k = 6$), $N = 40$ for spin 1 and $\tau = 2.228$ μs ($k = 4$), $N = 64$ for spin 2. Z-rotations are implemented by choosing τ off-resonant: for values of τ that do not satisfy the above resonance condition the nuclear spins precess unconditionally around the Z-axis with frequency $\bar{\omega} = \omega_L + A_{\parallel}/2$. Detailed simulations of the nuclear spin dynamics are available in Sec. 4.6.5.

4.5.3 Nuclear spin initialization

The electron Ramsey measurements in Fig. 4.1d and 1e are analysed in two ways:
(1) The measurements are separately fit to $F = \frac{1}{2} - \frac{1}{2}e^{-(t/T_2^*)^2}\cos(\delta t)$, in which T_2^* is a measure for the dephasing time set by the entire spin bath and δ is the detuning. The external magnetic field stability of better than 2 mG over the total integration time (∼2 hours), required to measure the increase in T_2^* compared to without nuclear spin initialization, was achieved by post selecting from a larger measurement set.
(2) Using the hyperfine components $A_{\parallel}^1$ and $A_{\parallel}^2$, the measurements are fit to:

$$\begin{aligned} F = &\frac{1}{2} - \frac{1}{2}e^{-(\tau/T_2^{**})^2} F_1 F_2 \cos(((\delta + (A_{\parallel}^1 + A_{\parallel}^2)/2)t) \\ &+ F_1(1-F_2)\cos(((\delta + (A_{\parallel}^1 - A_{\parallel}^2)/2)t)) \\ &+ (1-F_1)(F_2)\cos((\delta + (-A_{\parallel}^1 + A_{\parallel}^2)/2)t) \\ &+ (1-F_1)(1-F_2)\cos((\delta - (A_{\parallel}^1 + A_{\parallel}^2)/2)t)). \end{aligned}$$

$T_2^{**} = 4.5(3)$ μs is the electronic dephasing due to the rest of the spin bath, i.e. not including the two spins under study. To accurately determine the nuclear spin initialization fidelities F_1 and F_2 we use a different data set that is averaged over a longer time and is given in Fig. 4.13.

4.5.4 Quantum error correction analysis

The applied errors realize the quantum map:

$$E(\rho, \theta) = \cos^2(\theta/2) I\rho I + \sin^2(\theta/2) X\rho X \tag{4.2}$$

in which ρ is the initial density matrix and I is the identity operator (error characterization in Sec. 4.6.8). We analyze the error-correction protocol by separating depolarization during the encoding, decoding and error-correction steps from the robustness of the encoded state to applied errors, which is characterized by the three probabilities p_n that an error applied on qubit n is successfully corrected (derivation in Sec. 4.6.8). The process fidelity for a single-qubit error (Fig. 4.4d) is then given by:

$$F_p(\theta) = F_{p0} + A_{YZ}[p_n + (1 - p_n)\cos(\theta)], \tag{4.3}$$

where $F_{p0} = (F_x + F_{-x})/4$ and $A_YZ = (F_y + F_{-y} + F_z + F_{-z} - 2)/4$ characterize the additional depolarization and are given by the average fidelities without applied errors. Equation (1) contains a constant due to the $|\pm X\rangle$ states, which are unaffected by the applied error, and a sum of successful ($p_n = 1$) and unsuccessful ($p_n = 0$) error correction for the $|\pm Y\rangle$ and $|\pm Z\rangle$ states. For errors simultaneous on all three qubits (Fig. 4.4e), the process fidelity becomes:

$$F_p(p_e) = F_{p0} + A_{YZ}[1 - 3p_e + 3p_e^2 - 2p_e^3 + 3(2\langle p_n\rangle - 1)(p_e - 3p_e^2 + 2p_e^3)],$$

with $p_e = \sin^2(\theta/2)$ the error probability. In general this equation describes a third order polynomial. For ideal error correction ($\langle p_n\rangle = 1$) the linear term vanishes, whereas without robustness to errors, $\langle p_n\rangle = 2/3$, the result is strictly linear. The inversion symmetry about $p_e = 0.5$ observed both theoretically and experimentally ensures that the nonlinear behavior is not due to spurious coherent rotations.

4.6 Supporting material

4.6.1 Setup and sample

The experimental setup and sample are described in detail in the supplementary information of Van der Sar *et al.*[7] and in Ch. 3 of this thesis. We used a type-IIa chemical vapour deposition grown diamond with a 1.1% natural abundance of carbon-13 (Element 6). Solid immersion lenses were fabricated on top of the nitrogen vacancy (NV) centres to enhance the collection efficiency[33]. The electron spin is

controlled by microwaves through an on-chip stripline (Rabi frequency of 31.25 MHz). A magnetic field of $B_z \approx 403$ G was applied along the NV symmetry axis using three electromagnets. At this magnetic field the intrinsic NV nitrogen-14 spin is polarized due to an excited-state anti-crossing[34,35].

4.6.2 Electron spin initialization and readout

This section discusses the electron spin initialization, re-initialization and readout. In particular it analyzes how the imperfect spin and charge state initialization affect the outcomes of the different type of experiments performed.

4.6.3 Experimental

The electron spin is initialized in the $m_s = 0$ state by a 532 nm (~ 150 μW) laser pulse (typically 2-4 μs) and read out through its spin-dependent time-resolved fluorescence. In all experiments we measure the difference signal $\Delta_f = S_f - \tilde{S_f}$ between the fluorescence signal S_f for the final state and the fluorescence signal $\tilde{S}_f$ for the final state with a pi-pulse applied just before readout ($m_s = 0$ to $m_s = -1$ transition). The obtained value is then normalized by dividing it by the same difference signal right after initialization: $\Delta_i = S_i - \tilde{S}_i$, where S_i is without pi-pulse and $\tilde{S}_i$ with pi-pulse. The final normalized contrast C is:

$$C = \frac{S_f - \tilde{S}_f}{S_i - \tilde{S}_i} = \frac{\Delta_f}{\Delta_i}. \tag{4.4}$$

This method directly measures the contrast between $m_s = 0$ and $m_s = -1$ states. Note that $-1 \leq C \leq 1$ and that the result is independent of the population in other states, such as $m_s = +1$, that are not affected by the microwave pi-pulse. The reported expectation values directly correspond to C, the measured fidelities are obtained from $F = C/2 + 1/2$.

Initial electron state

The electronic initialization involves both spin states ($m_s = -1, 0, +1$) and charge states (NV^- and NV^0). The initial state ρ_i is:

$$\rho_i = p_1\rho_0 + p_2\rho_m + p_3\rho_s + p_4\rho_c, \tag{4.5}$$

with $p_1 + p_2 + p_3 + p_4 = 1$, and in which ρ_0 is the desired $m_s = 0$ state, ρ_m is the completely mixed state of $m_s = 0$ and $m_s = -1$, ρ_s represents the other spins states (here $m_s = +1$) and ρ_c other charge states (here NV^0).

The precise values for p_1, p_2, p_3 and p_4 are unknown. For this NV centre the spin-state initialization fidelity was previously reported to be $F_s = \frac{p_1 + p_2/2}{p_1 + p_2 + p_3} > 0.95$ under

similar conditions[7]. The NV^- charge-state initialization fidelity $F_c = p_1 + p_2 + p_3$ is unknown here, but values of ~ 0.7 have been reported for other NV centres[36].

The available initial population is given by p_1. Ideally, measurements of $C = \frac{\Delta_f}{\Delta_i}$ directly reflect the actual polarization so that $-p_1 \leq C \leq p_1$. Because only the ρ_0 term in Eq. 4.5 is affected by microwave pulses only this term yields signal (non-zero Δ), so that the normalization signal always is $\Delta_i = D_0 p_1$, with D_0 an unknown proportionality constant. Next we determine the obtainable final signal Δ_f for two types of experiments: experiments that do not re-initialize the electron to create additional polarization in the nuclear spin register and those that do.

First consider experiments where only a single electron initialization step is used, i.e. experiments that do not transfer polarization to the nuclear spins before resetting the electron spin. In this case the maximum value of Δ_f simply is $D_0 p_1$ and the maximum contrast is $C_{max} = \frac{D_0 p_1}{D_0 p_1} = 1$. Due to the calibration, the final measured contrast is independent of p_1 and therefore does not take into account the charge and spin initialization fidelities.

Experiments with nuclear spin initialization

Now consider experiments in which the electron spin polarization is transferred to a nuclear spin, the electron is re-initialized, and finally the electron is used to measure the nuclear spin state. The result Δ_f depends on the correlations of the spin (charge) state after the re-initialization step with the spin (charge) state before it. We assume the spin states before and after re-initialization are uncorrelated, and derive the result Δ_f for both uncorrelated (no memory) and maximally positive correlations (ideal memory) for the charge state.

The state of the initialized electron and a single nuclear spin in a completely mixed state is:

$$\rho = \rho_{electron} \otimes \rho_{nucleus} = p_1(\rho_0 \otimes \rho_m) + p_2(\rho_m \otimes \rho_m) + p_3(\rho_s \otimes \rho_m) + p_4(\rho_c \otimes \rho_m), \quad (4.6)$$

swapping the electron and nuclear spin states gives:

$$\rho = p_1(\rho_m \otimes \rho_0) + p_2(\rho_m \otimes \rho_m) + p_3(\rho_s \otimes \rho_m) + p_4(\rho_c \otimes \rho_m), \quad (4.7)$$

as the SWAP gate has no effect on the erroneous electron spin (ρ_s) and charge (ρ_c) states. The electron spin initialization p_1 is thus directly transferred to the nuclear spin.

We re-initialize the electron spin and assume that the electron spin initialization is independent of the nuclear spin state. First consider the case of no correlations (no memory) for the charge state, so that the electron is completely re-initialized. The state in Eq. 4.7 becomes:

$$\rho = (p_1\rho_0 + p_2\rho_m + p_3\rho_s + p_4\rho_c) \otimes (p_1\rho_0 + (1 - p_1)\rho_m). \quad (4.8)$$

Reading out the nuclear spin with the electron spin only yields non-zero signal for both the electron and nuclear spins in the pure state ρ_0, so that:

$$\Delta_f = D_0 p_1^2, \quad C_{max} = p_1, \tag{4.9}$$

which shows that the maximum contrast C_{max} is reduced by a factor p_1 and thus that the experiment faithfully reflects the actual nuclear spin state, including a reduced fidelity due to the imperfect electron spin and charge initialization.

If the electron re-initialization does not change the charge state, Eq. 4.7 after electron re-initialization becomes:

$$\rho = p_1 \left(\frac{p_1\rho_0 + p_2\rho_m + p_3\rho_s}{p_1+p_2+p_3} \right) \otimes \rho_0 + (p_2+p_3) \left(\frac{p_1\rho_0 + p_2\rho_m + p_3\rho_s}{p_1+p_2+p_3} \right) \otimes \rho_m + p_4 \rho_c \otimes \rho_m \tag{4.10}$$

Again taking into account that no difference signal is obtained if either the electron or the nuclear spin is not in state ρ_0:

$$\Delta_f = \frac{p_1^2}{p_1+p_2+p_3}, \quad C_{max} = \frac{p_1}{p_1+p_2+p_3} \tag{4.11}$$

The result now accurately reflects the spin state initialization, but is independent of the charge state initialization.

The high nuclear initialization fidelity obtained here ($F \approx 0.9$, Fig. 4.1), indicates that the charge state initialization fidelity is high (> 0.90) or that the measurements are not sensitive to it (i.e. the re-initialization laser pulse has low probability to change the charge state). The same value gives a lower limit of the electron spin initialization $F = p_1/2 + 1/2 \geq 0.90$, as the swap gate for initialization and the nuclear spin readout have limited fidelities as well.

In conclusion, as in previous room temperature experiments, the charge state is not rigourously initialized nor proven to be fully reflected in the measurement outcomes. Therefore the measured state fidelities do not give the actual purity of the states and no entanglement can be proven to be present. Nevertheless the (entangling) gates and protocols developed and studied in this work can be accurately investigated through their action on the prepared states. Note that methods to initialize the charge state have been developed at room temperature[11,36] and that pure entangled states have been reported at cryogenic temperatures using simultaneous spin and charge initialization[9].

4.6.4 Characterization and control for three NV centres

To demonstrate that harnessing weakly coupled spins makes multiple qubits available for each defect with high certainty, we have controlled three weakly coupled nuclear spins for each of the three NV centres studied. This section contains the

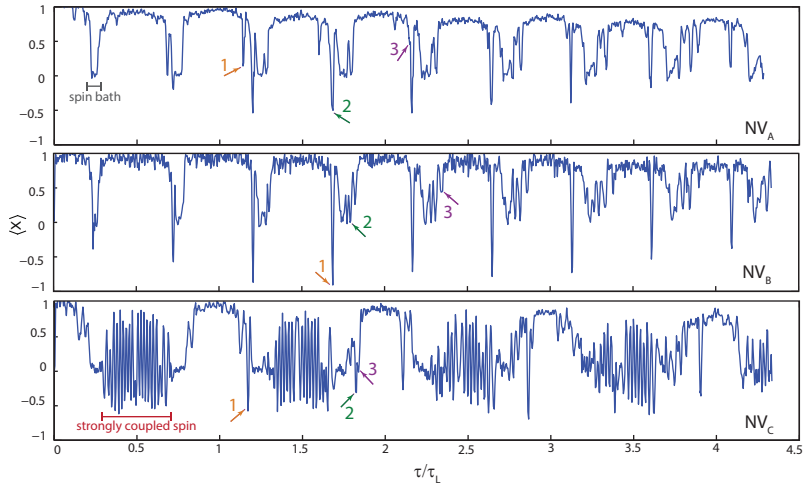


Figure 4.5 — Characterization of the nuclear spin environment for the three NV centres studied. Dynamical decoupling spectroscopy[23] for NV_A, NV_B and NV_C. The electron spin is prepared in a coherent superposition state ($|X\rangle = \frac{1}{\sqrt{2}}(|0\rangle + |1\rangle)$) and a dynamical decoupling sequence with 32 pi-pulses of the form $(\tau - \pi - 2\tau - \pi - \tau)^{16}$ is applied with variable interpulse delay 2τ before measuring $\langle X\rangle$. Sharp periodic resonances (dips) in the signal indicate an entangling operation of the electron spin with individual ^{13}C spins in the spin bath[23]. The arrows indicate the 9 different ^{13}C nuclear spins, and the values of τ used, for which we implemented initialization, control and readout (see Figs. 4.6 for NV_A, 4.7 for NV_B and 4.8 for NV_C). The experiments in the main text use nuclear spin 1 and 2 of NV_A. τ_L is the bare Larmor period.

characterization of the NV centres and the nuclear-spin free-evolution experiments that demonstrate the initialization, control and readout of the nuclear spins.

Characterization of the nuclear spin environment

We use dynamical decoupling spectroscopy[23] to characterize the nuclear spin environment of a total of three NV centres: NV_A, which is studied in the main text, and the two additional centres NV_B and NV_C (Fig. 4.5). The resulting curves provide characteristic fingerprints of the nuclear spin environments of the NV centre.

NV_A and NV_B show qualitatively similar behavior (Fig. 4.5). Both curves contain periodic broad collapses of the signal (echo collapses) due to the spin bath at $\tau/\tau_L = m/4$ with odd m, as well as distinct sharp periodic dips due to the resonances of individual ^{13}C nuclear spins that become visible at larger τ (examples are marked by the numbered arrows)[23]. However, the positions and strengths of the resonances

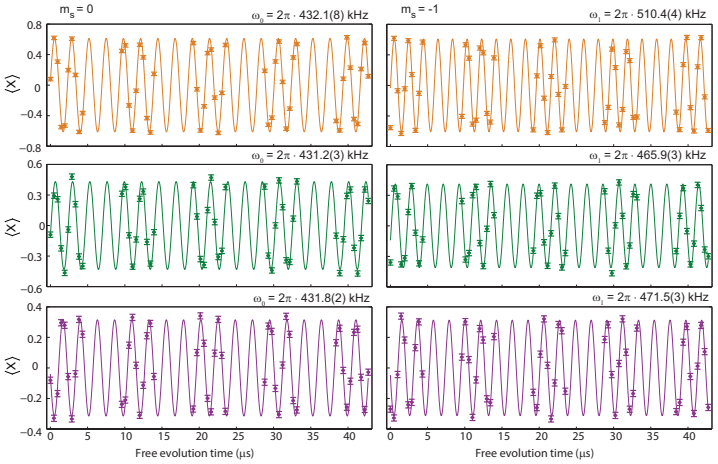


Figure 4.6 — Control of three weakly coupled nuclear spins for NV$_A$. Experiments as in Fig. 4.2, but with the electron spin in $m_s = 0$ (left) or $m_s = -1$ (right). The values for τ used for spin 1 (orange), spin 2 (green) and spin 3 (purple) are marked in Fig. 4.5. Note that nuclear spin 1 and nuclear spin 2 are the two spins studied in detail and used for implementing the quantum-error-correction protocol.

differ strongly as the the distribution of nuclear spins near each NV centre is unique. In addition to a bath of weakly-coupled ^{13}C spins NV$_C$ shows a rapidly oscillating component in the signal due to the presence of a nuclear spin with a strong hyperfine interaction (hyperfine interaction of $2\pi \cdot 453$ kHz and therefore strongly coupled).

Control of 3 weakly coupled nuclear spins per NV centre

For each of the three NV centres in Fig. 4.5 we select three nuclear spins. For each spin we select a resonance that is well separated from the other qubits and the rest of the bath (marked in the figure by arrows) in order to construct a conditional gate (see subsection 'Nuclear gate design'). We use this gate to realize initialization, control and direct readout and perform nuclear free precession experiments (see Figs. 2a-d). We prepare the electron spin in $m_s = 0$ or $m_s = -1$. For $m_s = 0$ all spins precess with $\omega_0 = \omega_L$, as expected. The unique precession frequencies $\omega_1 \approx \omega_L + A_\parallel$ for $m_s = -1$ confirm that in each case three different ^{13}C spins are controlled and that these spins have weak hyperfine interactions (Figs. 4.6, 4.7 and 4.8).

These results demonstrate the control of three weakly-coupled nuclear spins for each NV centre studied. Our decoherence-protected gates therefore make several nuclear spins available per defect centre with a high certainty, in stark contrast to the highly probabilistic nature of the presence of strongly coupled ^{13}C spins. The fact that the

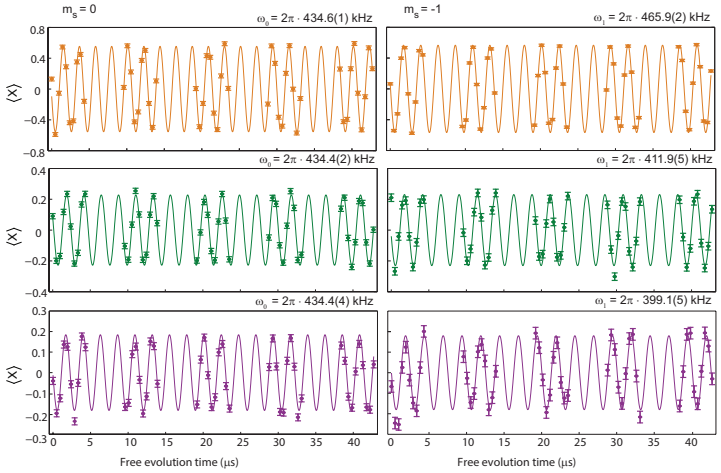


Figure 4.7 —Control of three weakly coupled nuclear spins for NV$_B$. Experiments as in Fig. 4.2, but with the electron spin in $m_s = 0$ (left) or $m_s = -1$ (right). The values for τ used for spin 1 (orange), spin 2 (green) and spin 3 (purple) are marked in Fig. 4.5.

gates can be applied in the presence of strongly coupled nuclear spins, including the intrinsic Nitrogen and nearby ^{13}C nuclear spins, indicates that quantum registers with over 5 nuclear spins are now well within reach (see e.g. NV$_C$ in Fig. 4.5).

4.6.5 Nuclear spin dynamics and gates

Hyperfine parameters

We obtain the hyperfine parameters for the NV centre used in the main text (NV$_A$) following Taminiau *et al.*[23]. We first select a well-isolated resonance dip in Fig. 4.5 and identify the resonance order k, and the ^{13}C spin that the resonance belongs to, using the periodicity of the resonances. We then determine the parallel $A_\parallel$ and the perpendicular $A_\perp$ components of the hyperfine interaction by fitting a small part of the curve around the resonance to the theory[23]. The hyperfine parameters for the three nuclear spins for NV$_A$ are given in Table 4.1. The two nuclear spin qubits in the main text are spin 1 and 2.

Nuclear gate design

With an appropriate rotation of the coordinate axes, the Hamiltonian of the NV electron spin and a single ^{13}C spin is:

$$\hat{H} = A_\parallel \hat{S}_z \hat{I}_z + A_\perp \hat{S}_z \hat{I}_x + \omega_L \hat{I}_z = |0\rangle\langle 0|\hat{H}_0 + |1\rangle\langle 1|\hat{H}_1, \tag{4.12}$$

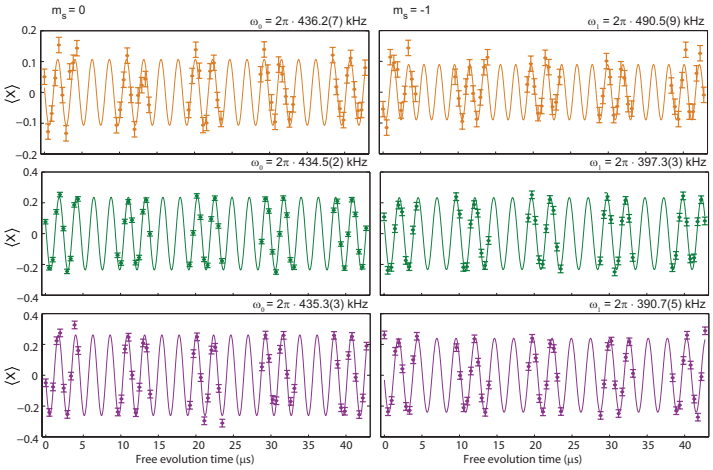


Figure 4.8 —Control of three weakly coupled nuclear spins for NV$_C$. Experiments as in Fig. 4.2, but with the electron spin in $m_s = 0$ (left) or $m_s = -1$ (right). The values for τ used for spin 1 (orange), spin 2 (green) and spin 3 (purple) are marked in Fig. 4.5.

Nuclear spin	$A_\parallel$ (kHz)	$A_\perp$ (kHz)
1	78.2(8)	30(1)
2	32(3)	44(2)
3	41.2(4)	19.2(7)

Table 4.1 —Hyperfine parameters for the three ^{13}C spins for NV$_A$. $A_\parallel$ is the component parallel to the applied magnetic field (along the NV symmetry axis). $A_\perp$ is the perpendicular component. This NV centre was studied previously[23].

where $\hat{S}_i$ ($\hat{I}_i$) are the electron (nuclear) spin operators, $\omega_L = 2\pi \cdot 431$ kHz is the nuclear Larmor frequency (applied magnetic field $B_z \approx 403$ G). The nuclear spin evolution thus depends on the electron spin state: $\hat{H}_0$ if the electron is in $m_s = 0$ (state $|0\rangle$), and $\hat{H}_1$ if the electron is in $m_s = -1$ (state $|1\rangle$), with

$$\hat{H}_0 = \omega_L \hat{I}_z, \quad \text{and} \quad \hat{H}_1 = (A_\parallel + \omega_L)\hat{I}_z + B_\perp \hat{I}_x. \tag{4.13}$$

All nuclear gates are implemented by applying a sequence of periodic pulses on the electron spin:

$$(\tau - \pi - 2\tau - \pi - \tau)^{N/2}, \tag{4.14}$$

with τ a free evolution time, π a pi-pulse on the electron and N the total number of pulses. We symmetrize the decoupling sequence by alternating pi-pulses around the X and Y axis (base sequence $X - Y - X - Y - Y - X - Y - X$, which is then

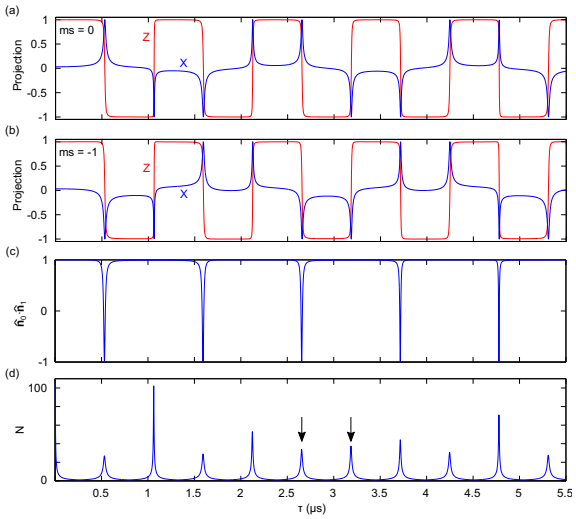


Figure 4.9 —Simulations of the nuclear dynamics for spin 1. a,b, The X and Z projections of **(a)** $\hat{\mathbf{n}}_0$ (the net rotation axis for initial electron state $m_s = 0$) and of (b) $\hat{\mathbf{n}}_1$ (initial electron state $m_s = -1$). The Y projection is 0. **c,** The inner product $\hat{\mathbf{n}}_0 \cdot \hat{\mathbf{n}}_1$ of the the two rotation axis indicates if the gate is unconditional (parallel axes, $\hat{\mathbf{n}}_0 \cdot \hat{\mathbf{n}}_1 = 1$) or conditional (anti-parallel axes, $\hat{\mathbf{n}}_0 \cdot \hat{\mathbf{n}}_1 = -1$). **d,** The number of pulses N required for a $\pi/2$-rotation. The total gate duration is given by $2N\tau$. The two arrows mark the values for τ for the conditional and unconditional gates for this spin.

repeated). The nuclear evolution operators for the basic sequence ($N = 2$) are:

$$\hat{V}_0 = \exp\left[-i\hat{H}_0\tau\right]\exp\left[-i\hat{H}_1 2\tau\right]\exp\left[-i\hat{H}_0\tau\right] \quad (4.15)$$

$$\hat{V}_1 = \exp\left[-i\hat{H}_1\tau\right]\exp\left[-i\hat{H}_0 2\tau\right]\exp\left[-i\hat{H}_1\tau\right], \quad (4.16)$$

for $m_s = 0$ and $m_s = -1$ respectively.

The conditional operators $\hat{V}_0$ and $\hat{V}_1$ can be represented as:

$$\hat{V}_0 = \exp\left[-i\phi(\hat{\mathbf{I}} \cdot \hat{\mathbf{n}}_0)\right] \quad (4.17)$$

$$\hat{V}_1 = \exp\left[-i\phi(\hat{\mathbf{I}} \cdot \hat{\mathbf{n}}_1)\right], \quad (4.18)$$

which illustrates that the net evolution is a rotation by an angle ϕ around an axis $\hat{\mathbf{n}}_i$ that depends on the initial state of the electron spin: $\hat{\mathbf{n}}_0$ for $m_s = 0$ and $\hat{\mathbf{n}}_1$ for $m_s = -1$. The rotation angle ϕ is independent of the electron spin input state[23]. Next, we show that both conditional and unconditional rotations can be constructed by choosing τ. Figure 4.9 shows the dynamics for nuclear spin 1. Because $\omega_L \gg A_\perp$, the X and Z components of the rotation axes $\hat{\mathbf{n}}_0$ (Fig. 4.9a) and $\hat{\mathbf{n}}_1$ (Fig. 4.9b) show sharp resonances, for which the nuclear spin undergoes an X-rotation. These

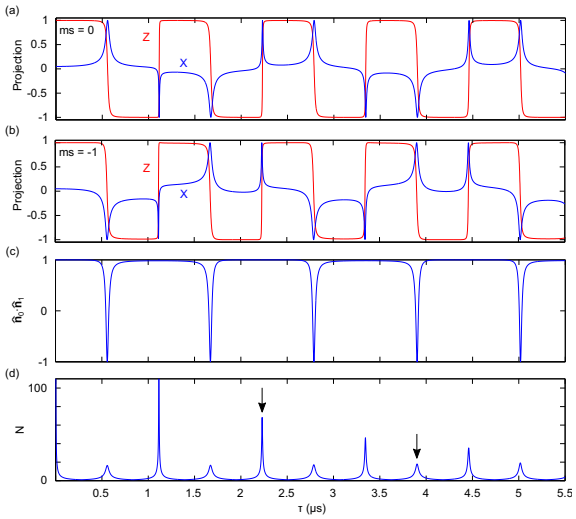


Figure 4.10 —Simulations of the dynamics for nuclear spin 2. See description in Fig. 4.9.

resonances occur for:

$$\tau \approx \frac{k\pi}{2\omega_L + A_\parallel}, \tag{4.19}$$

with integer k. The X-rotation is conditional for the odd resonances (odd k, anti-parallel rotation axes: $\hat{\mathbf{n}}_0 \cdot \hat{\mathbf{n}}_1 = -1$) and unconditional for the even resonances (even k, parallel axes: $\hat{\mathbf{n}}_0 \cdot \hat{\mathbf{n}}_1 = 1$) (Fig. 4.9c). For all other values of τ the nuclear spin undergoes a simple Z-rotation independent of the electron spin state ($\hat{\mathbf{n}}_0 \cdot \hat{\mathbf{n}}_1 = 1$). The electron and nuclear spin are then effectively decoupled from each other. The number of pulses N required for a $\pi/2$ rotation are shown in Fig. 4.9 as a function of τ. The dynamics for spin 2 are similar (Fig. 4.10), but the resonances occur for different values of τ due to the difference in $A_\parallel$.

The values for τ and N for the gates used in this work are given in Tab. 4.2 and the values for τ are also indicated in Figs. 4.9d and 4.10d.

The sharp resonances enable the universal control of a selected nuclear spin, while decoupling the electron spin from all other nuclear spin qubits and the rest of the environment. The gates are thus selective, not limited by the electron T_2^* [7,37] and do not require strong coupling.

Nuclear gate characterization

To characterize the conditional and unconditional gates we study the effect of the gates on an initialized nuclear spin state, as a function of the number of electron spin

		τ (μs)	N	Total time (μs, rounded)
Spin1:	$R^e_X(\pi/2)$	2.656	32	170
	$R_X(\pi/2)$	3.186	40	255
	$R_Z(\pi/2)$	2.058	4	16
Spin2:	$R^e_X(\pi/2)$	3.900	18	140
	$R_X(\pi/2)$	2.228	64	285
	$R_Z(\pi/2)$	2.100	2	8

Table 4.2 —Gate parameters. $R_\alpha(\theta)$ is a rotation of the nuclear spin around Bloch-sphere axis α by an angle θ. For gates marked R^e the rotation direction is controlled by the electron spin state, for all other gates the direction is unconditional.

pulses in the gate. Figures 2e and 2f give the Y-projections for both gates for nuclear spin 1. Figure 4.11 gives the complete set of measurements, including the gates for nuclear spin 2 and the Z-projections that confirm that the gates are conditional and unconditional rotations around X.

Theoretical gate fidelities

To investigate the theoretical fidelity of the gates and the crosstalk of the gates to the other spin qubits, we apply the gates to a small set of initial states and calculate the fidelity with the ideal final state (Tab. 4.3). In general the resulting state fidelities for our two qubits (spin 1 and 2) are high (> 0.995). Even though spin 3 is not used as a qubit in the main text, it is considered here because its $A_\parallel$ value is similar to the value for spin 2. As a result the conditional gate on spin 2 also rotates spin 3, potentially leading to extra loss of electron coherence. These fidelities do not take into account the rest of the spin bath nor phonon-induced decoherence and depolarization.

The calculations use the experimental discretization precision (2 ns steps for τ). Nevertheless, the difference between the value used and the optimal value of τ can be different in the experiment and the calculation, as the values for the hyperfine interaction and the magnetic field used in the calculation might be slightly off. In the worst case the discretization reduces the fidelities for the X-rotations by ~ 0.005. Off-resonant rotations such as Z-rotations are not affected by this.

4.6.6 Nuclear initialization fidelity

The nuclear initialization fidelity is determined from Ramsey-type experiments as described in the main text. The measurements in Figs. 1f and 1g are post selected on small magnetic field drifts so that the absolute increase of T_2^* can be determined. For the initialization fidelity we use an average over a longer measurement that constantly switches between the different initialization conditions (Fig. 4.12). This approach has the advantage that the initialization fidelity can be determined more accurately and

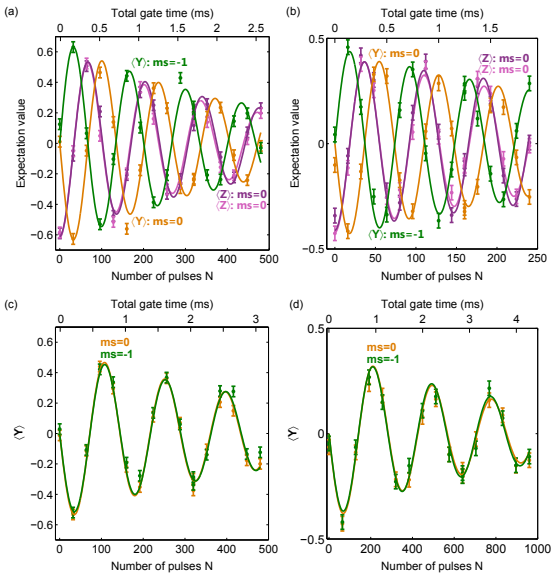


Figure 4.11 —Gate characterization. Action of the conditional **(a-b)** and unconditional **(c-d)** gates for both nuclear spin 1 **(a,c)** and nuclear spin 2 **(b,d)**. Measurement schemes in Figs. 2e and 2f. The Z-projection shows that the spin undergoes a Rabi oscillation and the Y-projection shows that the orientation of the rotation is either conditional **(a,b)** or unconditional on the electron state **(c,d)**. Not corrected for initialization or readout fidelities.

that the influence of magnetic field fluctuations averages out, but it is not suited for measurements of the absolute increase of T_2^*, as significant magnetic field fluctuations over the extended measurement time decrease T_2^*.

In these experiments we repeat the initialization step four times when switching between initialization conditions to ensure maximum initialization fidelity. Once initialized in one of the states, a single initialization step before each repetition of the measurement is sufficient because these measurements leave the nuclear state mostly intact. We find $F_1 = 0.91(2)$ for nuclear spin 1 and $F_2 = 0.88(5)$ for nuclear spin 2 (Fig. 4.12).

Although the initialization protocol ideally needs only a single application, Fig. 4.13 shows that repeated applications do further increase the polarization before saturating after approximately 2 steps. In the implementation of the quantum error correction protocol (Fig. 4.4) only a single initialization step was used, and the sequence does not preserve the nuclear polarization, so that the initialization fidelities are lower than those obtained from Fig. 4.12. The results in Fig. 4.13 yield an initialization fidelity for these experiments of $F_1 \approx F_2 \approx 0.82$.

Target	Gate	Fidelity spin 1	Fidelity spin 2	Fidelity spin 3
Spin 1	$R^e_X(\pm\pi/2)$	0.9976	0.9997	0.9959
	$R_X(\pi/2)$	0.9981	0.9999	1.000
	$R^Z(\pi/2)$	0.9994	0.9992	0.9999
Spin 2	$R^e_X(\pm\pi/2)$	1.000	0.9999	0.9630
	$R_X(\pi/2)$	1.000	0.9987	0.9975
	$R_Z(\pi/2)$	0.9993	0.9971	0.9993

Table 4.3 —Theoretical fidelities. The state fidelity with the ideal state after application of the gates. The first collumn gives the target spin for the gate. The second column gives the type of gate. Conditional X-rotation: $R^e_X(\pm\pi/2)$. Unconditional X- and Z-rotations: $R_X(\pi/2)$ and $R_X(\pi/2)$. The electron spin always starts in $m_s = 0$. For the target spin the X-rotations are applied to $|0\rangle$ and the Z-rotations to $|X\rangle$. For the not-targeted spins all gates are applied to $|0\rangle$ and the ideal operation is a Z-rotation that has no effect. All numbers are rounded to four digits.

4.6.7 Two-qubit tomography

Two-qubit tomography (Fig. 4.3) is performed by mapping two-qubit correlations onto the electron spin before reading out the electron. Figure 4.14a shows the general principle and Fig. 4.14b shows our implementation.

4.6.8 Quantum error correction

This section discusses the application and characterization of the errors, gives the derivation of the theoretical analysis used in the main text, and gives the complete set of state fidelity results used to derive the process fidelities in the main text (Fig. 4.4).

Error implementation

The quantum error correction scheme corrects both coherent errors of the type $R_X(\theta)$, i.e. a rotation around the X-axis by angle θ or the quantum map:

$$\epsilon_c(\rho, \theta) = [\cos(\theta/2)I + i\sin(\theta/2)X]\rho[\cos(\theta/2)I - i\sin(\theta/2)X] \tag{4.20}$$

and non-unitary, decoherence-type, operations given by the quantum map:

$$\epsilon_d(\rho, \theta) = \cos^2(\theta/2)I\rho I + \sin^2(\theta/2)X\rho X \tag{4.21}$$

Errors on the electron spin are directly created by a microwave pulse that implements $R_X(\theta)$. In half the experiments a positive rotation $R_X(+\theta)$ is applied and in the

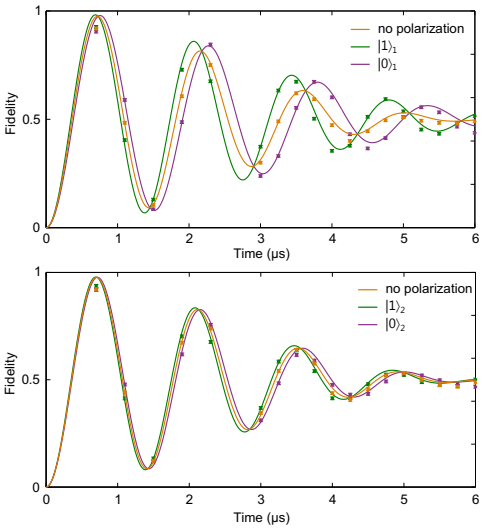


Figure 4.12 —Data set for the determination of the nuclear spin initialization fidelity. Electron spin free evolution measurements with and without nuclear spin initialization. Top: nuclear spin 1, fidelity $F_1 = 0.91(2)$. Bottom nuclear spin 2, fidelity $F_2 = 0.88(5)$. The three curves are measured in a single experiment that is long enough to average over the magnetic field fluctuations, reducing T_2^* to 3.1(1) μs.

other half a negative rotation $R_X(-\theta)$. The final result is the average over the two measurements, so that the implemented error is of the form of Eq. 4.21.

Errors on the nuclear spins are implemented through the electron spin. First the error is applied to the electron spin. Then the initialization gate transfers the error to the nuclear spin state. This operation gives the same result as applying $\epsilon_d(\rho, \theta)$ on an initialized nuclear spin state. Figure 4.15 shows the resulting fidelity with $|Z\rangle = |0\rangle$ for both nuclear spins as a function of the error pulse amplitude. The observed oscillation around $F = 1/2$ confirms the expected application of the error.

Theoretical analysis

We analyze the quantum error process as a combination of imperfect majority voting and a general decoherence/depolarization process. We assume the following two properties: (1) that applied errors have no effect on the $|\pm X\rangle$ states and (2) that the probabilities that the error correction (majority voting) is successful for errors applied to qubit 1, qubit 2 or qubit 3 are given by p_1, p_2 and p_3 respectively. In the above statement an error is defined relative to the other two qubits; simultaneous errors on qubit 2 and qubit 3 are recognized by the majority voting as an error on qubit 1. These probabilities then completely describe the effectiveness of the error

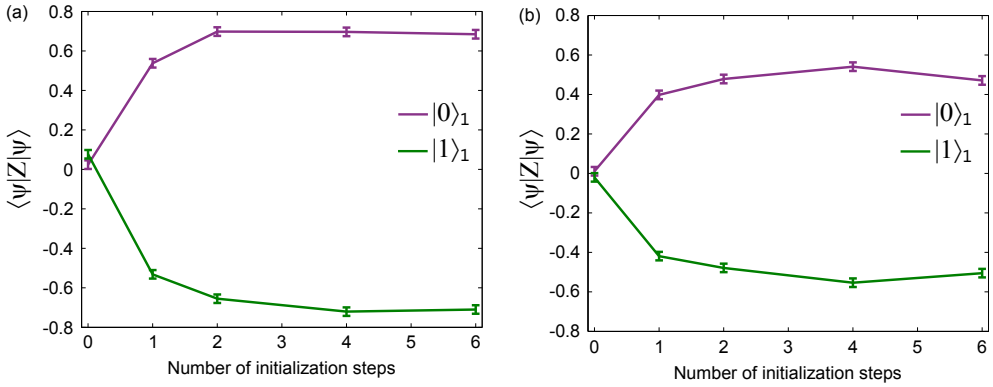


Figure 4.13 —Increased initialization fidelity through multiple initialization steps. The measured expectation value $\langle Z\rangle = \langle\psi|Z|\psi\rangle$ for the nuclear spin state $|\psi\rangle$ as a function of the number of initialization steps. The nuclear spin is either initialized on $|0\rangle$ or $|1\rangle$. **a,** Nuclear spin 1. **b,** Nuclear spin 2. Data not corrected for initialization or readout fidelities.

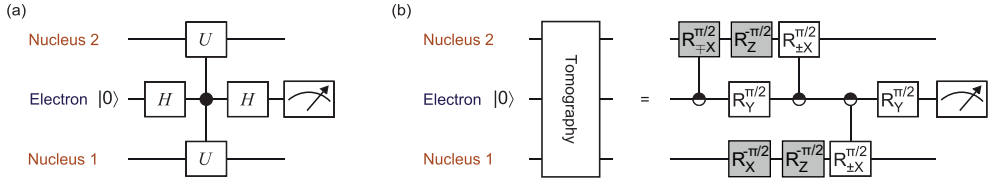


Figure 4.14 —Two-qubit tomography. We measure the expectation values of the different combinations of the nuclear two-qubit pauli operators using the electron spin. **a,** General readout scheme to measure $\langle UU\rangle$, with U a unitary operator and H the Hadamard gate. **b,** Our implementation. The shaded gates are optional basis rotations. Note that the signs of the first two operations on both nuclear spins are corrected with respect to the publication.

correction process against errors occuring on the encoded state (for an ideal case $p_1 = p_2 = p_3 = 1$).

In each experiment we prepare 6 input states $|\alpha\rangle$:

$$|Z\rangle = |0\rangle\,, \tag{4.22}$$
$$|-Z\rangle = |1\rangle\,, \tag{4.23}$$
$$|X\rangle = \frac{1}{\sqrt{2}}(|0\rangle + |1\rangle), \tag{4.24}$$
$$|-X\rangle = \frac{1}{\sqrt{2}}(|0\rangle - |1\rangle), \tag{4.25}$$
$$|Y\rangle = \frac{1}{\sqrt{2}}(|0\rangle + i\,|1\rangle), \tag{4.26}$$
$$|-Y\rangle = \frac{1}{\sqrt{2}}(|0\rangle - i\,|1\rangle), \tag{4.27}$$

and measure the expectation values:

$$C_\alpha = \langle\psi_\alpha|\alpha|\psi_\alpha\rangle, \tag{4.28}$$

where $|\psi_\alpha\rangle$ is the output state for input state $|\alpha\rangle$, and $\alpha = Z,\ -Z,\ Y,\ -Y,\ X$, or $-X$. The fidelities of the output states with the input states are given by:

$$F_\alpha = C_\alpha/2 + 1/2. \tag{4.29}$$

We label the 8 possible combinations of (applied) errors that can occur with j. For example: $j = 000$ implies no error, $j = 100$ is an error on qubit 1, etc. The obtained

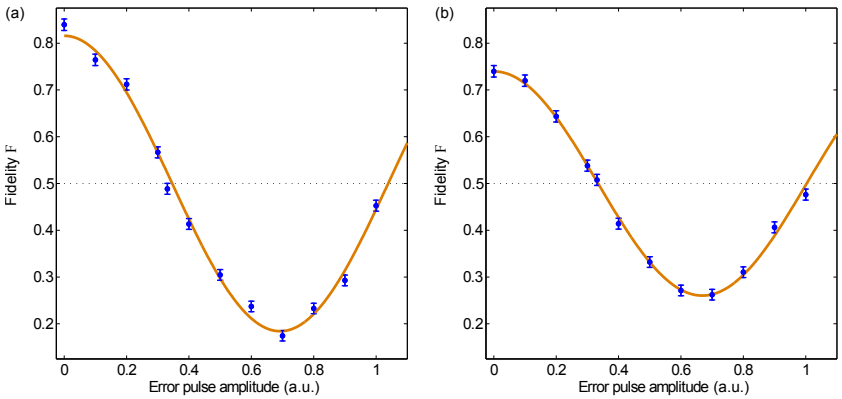


Figure 4.15 —Characterization of the nuclear spin errors. Fidelity F of the final nuclear state with $|Z\rangle = |0\rangle$ as a function of the amplitude of the error pulse applied on the electron. **a,** For nuclear spin 1. **b,** For nuclear spin 2. Lines are fits to the expected cosine behavior around fidelity 0.5. The measurements are not corrected for readout or initialization fidelities.

signal for error combination j and input state $|\alpha\rangle$ is C_α^j. Using the above assumptions all possible results can be described by the probabilities p_1, p_2 and p_3 together with the obtained signals when no error is applied $C_{\pm Z}^{000}$, $C_{\pm Y}^{000}$ and $C_{\pm X}^{000}$. All possible values based on the above error correction model are given in Tab. 4.4.

Signal for error j	$\|\pm Z\rangle$	$\|\pm Y\rangle$	$\|\pm X\rangle$
C_α^{000}	$C_{\pm Z}^{000}$	$C_{\pm Y}^{000}$	$C_{\pm X}^{000}$
C_α^{001}	$(2p_3-1)C_{\pm Z}^{000}$	$(2p_3-1)C_{\pm Y}^{000}$	$C_{\pm X}^{000}$
C_α^{010}	$(2p_2-1)C_{\pm Z}^{000}$	$(2p_2-1)C_{\pm Y}^{000}$	$C_{\pm X}^{000}$
C_α^{100}	$(2p_1-1)C_{\pm Z}^{000}$	$(2p_1-1)C_{\pm Y}^{000}$	$C_{\pm X}^{000}$
C_α^{011}	$-(2p_1-1)C_{\pm Z}^{000}$	$-(2p_1-1)C_{\pm Y}^{000}$	$C_{\pm X}^{000}$
C_α^{101}	$-(2p_2-1)C_{\pm Z}^{000}$	$-(2p_2-1)C_{\pm Y}^{000}$	$C_{\pm X}^{000}$
C_α^{110}	$-(2p_3-1)C_{\pm Z}^{000}$	$-(2p_3-1)C_{\pm Y}^{000}$	$C_{\pm X}^{000}$
C_α^{111}	$-C_{\pm Z}^{000}$	$-C_{\pm Y}^{000}$	$C_{\pm X}^{000}$

Table 4.4 —Action of the error correction protocol. C_α^j is the signal obtained for input state $|\alpha\rangle$ and error combination j. p_n is the probability that an error on qubit n is successfully corrected.

Single-qubit errors

For a variable strength error on one of the qubits the final fidelity for inputs $|\pm Y\rangle$ and $|\pm Z\rangle$ is given by a weighted sum of the two corresponding values in Tab. 4.4:

$$F_\alpha(\theta) = \frac{\cos^2(\theta/2)}{2} C_\alpha^{klm} + \frac{\sin^2(\theta/2)}{2} C_\alpha^{k'l'm'} + 1/2, \tag{4.30}$$

in which klm and $k'l'm'$ identify the applied error combination. For example, for the variable error applied to qubit 2 and no error to qubits 1 and 3, we have $klm = 000$ and $k'l'm' = 010$. For $|\pm X\rangle$ the signal is simply constant:

$$F_{\pm X}(\theta) = C_{\pm X}^{000}/2 + 1/2. \tag{4.31}$$

In Fig. 4.4d two different types of errors are applied: (1) just a variable error on qubit n and (2) a variable error on qubit 2 and a full flip on qubit 1. For a variable error on qubit n ($n = 1, 2, 3$) and input $|\pm Y\rangle$ or $|\pm Z\rangle$ Eq. 4.30 simplifies to:

$$F_\alpha(\theta) = \frac{C_\alpha^{000}}{2}(p_n + (1-p_n)\cos(\theta)) + 1/2, \tag{4.32}$$

in agreement with the interpretation of the values p_n as the probability that an error on qubit n is successfully corrected. For the variable error on qubit 2 and a full flip on qubit 1 we find:

$$F_\alpha(\theta) = \frac{C_\alpha^{000}}{2}(p_1 - p_3 + (p_1 + p_3 - 1)\cos(\theta)) + 1/2, \tag{4.33}$$

which is of the same form as Eq. 4.32 and shows that for $p_1 = p_3$ a cosine around fidelity 1/2 is obtained; the error correction is effectively switched of.

The process fidelity F_p of the error correction process with the identity is:

$$F_p(\theta) = \frac{F_Z(\theta) + F_{-Z}(\theta) + F_X(\theta) + F_{-X}(\theta) + F_Y(\theta) + F_{-Y}(\theta)}{4} - 1/2, \tag{4.34}$$

in which the F_α are given by Eqs. 4.30 and 4.31. For a single applied error this simplifies to:

$$F_p(\theta) = F_{p0} + A_{YZ}(p_n + (1 - p_n)\cos(\theta)), \tag{4.35}$$

in which $F_{p0} = (F_X + F_{-X})/4$ and $A_{YZ} = (F_Y(0) + F_{-Y}(0) + F_Z(0) + F_{-Z}(0) - 2)/4$. Note that all the different fidelities without error get grouped into two constants, one related to the average fidelity of the $|\pm X\rangle$ states and one related to the average fidelity of the $|\pm Y\rangle$ and $|\pm Z\rangle$ states without applied errors.

Ancilla initialization fidelity

We now discuss how our description accounts for imperfect ancilla initialization. As C_α^{000} is the signal without additional errors being applied, or additional errors occuring to the already encoded state, errors in the ancilla initialization are not included in θ. Instead, imperfect ancilla initialization reduces the probability that applied errors are corrected, i.e. it decreases the values p_n.

The effect of the initialization fidelities F_1 and F_2 of the two ancilla qubits (here qubit 1 and 3) is that the measured values $C_\alpha'^{ij}$ are now combinations of the C_α^j values in Tab. 4.4 following:

$$\begin{bmatrix} C_\alpha'^{0k0} \\ C_\alpha'^{0k1} \\ C_\alpha'^{1k0} \\ C_\alpha'^{1k1} \end{bmatrix} = \begin{bmatrix} F_1F_2 & F_1(1-F_2) & (1-F_1)F_2 & (1-F_1)(1-F_2) \\ F_1(1-F_2) & F_1F_2 & (1-F_1)(1-F_2) & (1-F_1)F_2 \\ (1-F_1)F_2 & (1-F_1)(1-F_2) & F_1F_2 & F_1(1-F_2) \\ (1-F_1)(1-F_2) & (1-F_1)F_2 & F_1(1-F_2) & F_1F_2 \end{bmatrix} \begin{bmatrix} C_\alpha^{0k0} \\ C_\alpha^{0k1} \\ C_\alpha^{1k0} \\ C_\alpha^{1k1} \end{bmatrix} \tag{4.36}$$

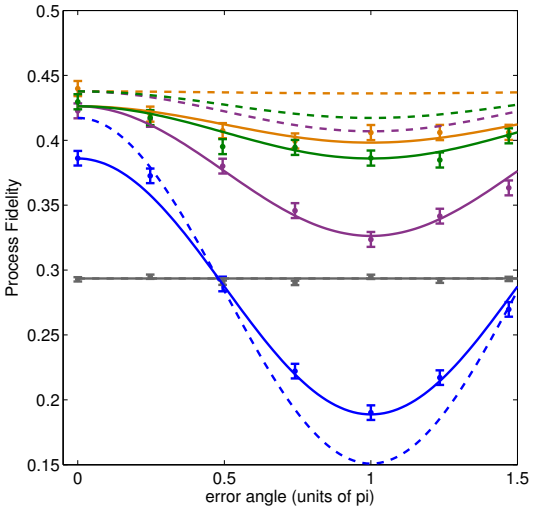


Figure 4.16 —Effect of initialization on the error correction. Process fidelity for selectively applied errors with error angle θ as in Fig. 4.4d. Solid lines are a fit to the model including Eq. 4.36 . The dashed lines are the expected results for ideal initialization of the two nuclear ancillas ($F_1 = F_2 = 1$).

We take $F_1 = F_2 = 0.82$ as an estimate for the initialization fidelities (Fig. 4.13). The resulting fits are shown in Fig. 4.16 (solid lines) and yield $p_n = 0.93(3), 0.89(3), 0.99(3)$ and $\langle p_n \rangle = (p_1 + p_2 + p_3)/3 = 0.94(2)$. These are the values p_n expected for ideal initialization. We calculate the expected result for ideal initialization by using the same values for p_n but setting $F_1 = F_2 = 1$ (dashed lines, Fig. 4.16). The imperfect initialization has two effects on the measured curves. First it strongly affects the success probability of the error correction. Second, it lowers the overall maximum fidelity slightly. This is a weak effect because it requires wrong preparation of both ancillas at the same time and is therefore proportional to $(1 - F_1)(1 - F_2)$.

We now derive explicit equations for the dependence of the error correction probabilities p_n on the ancilla initialization. For simplicity we set $F_1 = F_2 = F$ and assume that this is the only imperfection by setting $C_\alpha^{klm} = 1$ if $k + l + m \leq 1$ (maximum 1 error) and $C_\alpha^{klm} = -1$ if $k + l + m \geq 2$ (more than 1 error). The observed values $C_\alpha'^{klm}$ are given by Eq. 4.36 and the values for p_n can then be derived from Tab. 4.4. We find for the data qubit:

$$p_2 = \frac{-2F + 1}{2F^2 - 4F + 1} \tag{4.37}$$

and for the ancilla qubits:

$$p_1 = p_3 = \frac{-F}{2F^2 - 4F + 1}. \tag{4.38}$$

Errors on different types of qubits thus respond differently to the ancilla initialization fidelity. In particular note that without initialization, $F = 0.5$, $p_2 = 0$ and $p_1 = p_3 = 1$. The average value is given by:

$$\langle p_n \rangle = \frac{-4F + 1}{6F^2 - 12F + 3}. \tag{4.39}$$

This value monotonously decreases from 1 (perfect error correction) to 2/3 (no error correction) as the initialization fidelity goes from $F = 1$ (perfect initialization) to $F = 0.5$ (no initialization).

Simultaneous errors

The process fidelity F_p for simultaneous errors is given by:

$$\begin{aligned} F_p(p_e) =& (1 - 3p_e + 3p_e^2 - p_e^3)F_p^{000} && (4.40)\\ &+ p_e(1 - p_e)^2(F_p^{001} + F_p^{010} + F_p^{100}) && (4.41)\\ &+ p_e^2(1 - p_e)(F_p^{011} + F_p^{101} + F_p^{110}) && (4.42)\\ &+ p_e^3 F_p^{111}, && (4.43) \end{aligned}$$

with $p_e = \sin(\theta/2)^2$ the error probability and F_p^{klm} the process fidelity for applied error klm, i.e.:

$$F_p^{klm} = 1/4 \left(1 + \frac{C_X^{klm} + C_{-X}^{klm}}{2} + \frac{C_Y^{klm} + C_{-Y}^{klm}}{2} + \frac{C_Z^{klm} + C_{-Z}^{klm}}{2}\right). \tag{4.44}$$

with C_α^{klm} as given in Tab. 4.4 we obtain:

$$F_p(p_e) = F_{p0} + A_{YZ}\left[1 - 3p_e + 3p_e^2 - 2p_e^3 + 3(2\langle p_n \rangle - 1)(p_e - 3p_e^2 + 2p_e^3)\right], \tag{4.45}$$

The experiment is completely described by just 3 parameters: the offset F_{p0} (due to the average $|\pm X\rangle$ fidelity without applied errors), the amplitude A_{YZ} (due to the average $|\pm Y, Z\rangle$ fidelity without applied errors) and the average error correction probability $\langle p_n \rangle$.

Complete state fidelity data set

The complete set of state fidelities used to derive the process fidelities for errors applied to one of the qubits at a time (main text Fig. 4.4d) is shown in Fig. 4.17. The complete sets of state fidelities used to obtain the process fidelities for simultaneously applied errors (Fig. 4.4e of the main text) are given in Fig. 4.18a (without error correction) and Fig. 4.18b (with error correction).

4.6.9 Decoherence and depolarization

In this section we analyze the different decoherence mechanisms in the three-qubit register.

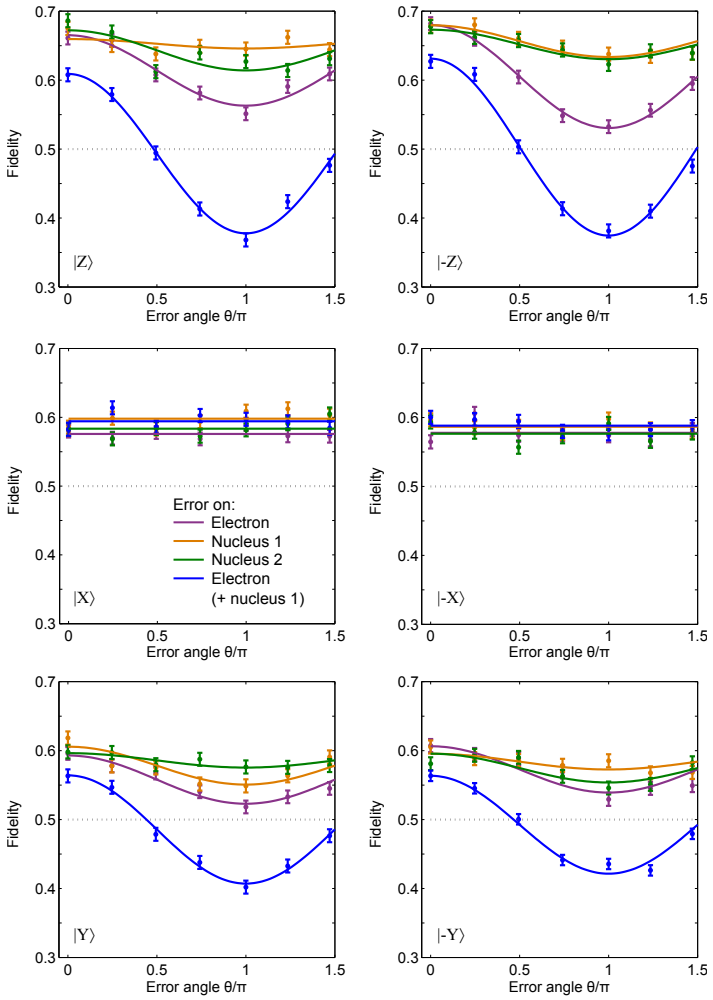


Figure 4.17 —Complete set of state fidelities for selectively applied errors. State fidelity for the 6 input states $|Z\rangle, |-Z\rangle, |X\rangle, |-X\rangle, |Y\rangle$ and $|-Y\rangle$, for 4 different combinations of errors and as a function of the error angle θ. We apply $\epsilon_d(\rho, \theta)$ to each of the three qubits separately and a combination of $\epsilon_d(\rho, \theta)$ to the electron and $\epsilon_d(\rho, \pi)$ to Nucleus 1. Lines are fits to Eqs. 4.31-4.33.

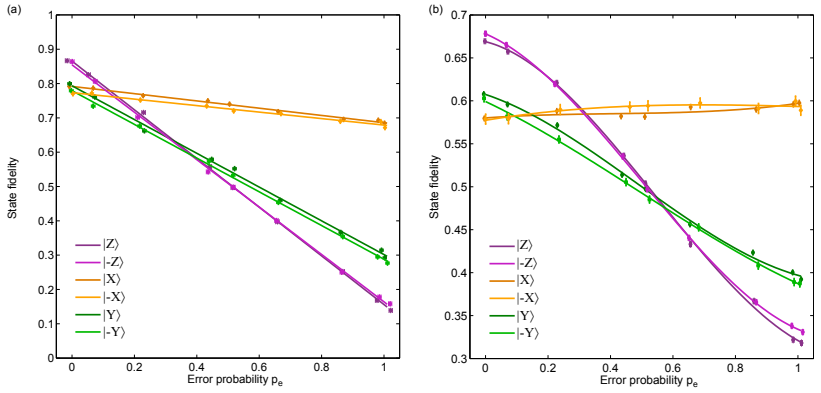


Figure 4.18 —a, State fidelities for the 6 input states as a function of the error probability without error correction. Lines are linear fits to the data. **b,** State fidelities for the 6 input states as a function of the error probability with error correction. Lines are 3^{rd} order polynomial fits to the data.

Electron depolarization "T_1"

The electronic depolarization (longitudinal relaxation or T1-type process) due to phonon interactions plays an important role at these room temperature experiments. To measure the depolarization rates we prepare one of the three states $m_s = -1$, $m_s = 0$ and $m_s = +1$ and let the system relax for a time t. We then apply a pi-pulse on the $m_s = 0$ transition (for the state starting in $m_s = 0$ nothing is done) before reading out the electron. The results are fit to a 3-level model that yields three rates between the different levels (Fig. 4.19). We find: $\Gamma_{0,-1} = 71(3)$ s^{-1}, $\Gamma_{0,+1} = 51(2)$ s^{-1} and $\Gamma_{-1,+1} = 133(3)$ s^{-1}. In this three level system no unique "T_1" value can be defined. Nevertheless, a separate analysis of each of the curves gives $1/e$ times of 3.24(9) ms ($m_s = -1$), 5.11(7) ms ($m_s = 0$, which is often reported as the T_1 value) and 3.91(6) ms ($m_s = +1$). We verified that the same rates were obtained with a 4 times lower laser output power, indicating that transitions induced by background illumination are negligible.

Electron decoherence T_{coh}

To measure the electronic coherence time under dynamical decoupling T_{coh} the electron spin is prepared along X. We then apply a decoupling sequence with $\tau = 2\pi/\omega_L = 2.324$ μs and measure the spin projection along X. The total time is varied by varying the number of pulses N in the sequence. The result is shown in Fig. 4.20. The green line marks the limit given by phonon-induced depolarization of the electron spin. It is given by the total decay rate out of the $m_s = 0$ and $m_s = -1$ levels: $\Gamma_{0,-1} + \Gamma_{0,+1}/2 + \Gamma_{-1,+1}/2$. The additional decoherence observed experimentally is consistent with previous reports[32] and is likely due to phonon-induced dephasing, as much longer coherence times were reported at low temperatures[18,32]. The expected signal without phonon-induced dephasing and depolarization is given by:

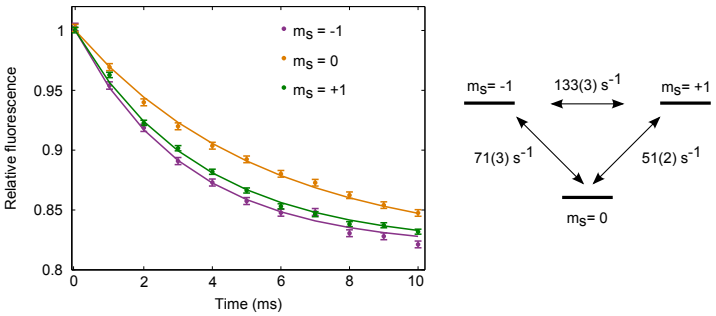


Figure 4.19 —Electron depolarization data and fit to three-level model. The fluorescence of the final electron readout is shown relative to the fluorescence for $m_s = 0$ preparation. The fits additionally use the measured fluorescence for $m_s = -1$ and $m_s = +1$ preparation.

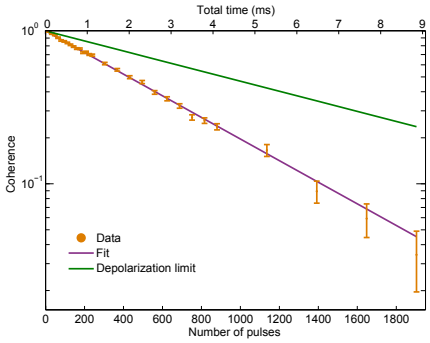


Figure 4.20 —Decoherence of the electron spin under dynamical decoupling. We apply a decoupling sequence to input state $|X\rangle$ and measure the final state along X. The interpulse delay τ is $2\pi/\omega_L$, in the same range as used for the nuclear gates. Purple: Exponential fit to the data that gives $T_{coh} = 2.86(4)$. Green: expected value due to electron depolarization alone.

$$S = e^{-\left(\frac{2\tau}{T_2}\right)^n N}, \tag{4.46}$$

with the spin echo time $T_2 = 251(7)$ μs. With $n = 3$ this gives an estimated decay time of ~ 700 ms, indicating that decoupling from the spin bath is not the limiting factor here.

Nuclear dephasing $T_2^\star$

We measure the nuclear dephasing time $T_2^\star$ by preparing the nuclear spin in a superposition and the electron spin in $m_s = 0$, and let the system evolve for variable time. The electron spin is then reset to $m_s = 0$ before the nuclear spin is measured along an axis that creates an effective detuning of approximately 1 kHz. We obtain $T_2^\star = 2.7(2)$ ms for nuclear spin 1

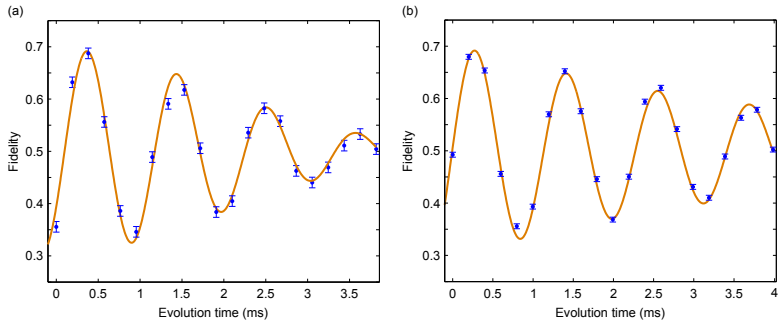


Figure 4.21 —Nuclear dephasing time $T_2^\star$. a, For nuclear spin 1. $T_2^\star = 2.7(2)$ ms, simultaneously measured electron $T_2^\star = 3.4(1)$ μs. **b,** For nuclear spin 2. $T_2^\star = 4.4(5)$ ms, simultaneously measured electron $T_2^\star = 3.18(8)$ μs. Fits are sine functions with a decaying envelope $e^{(-t/T_2^\star)^\delta}$. Spin 1: $\delta = 2$, spin 2: $\delta = 1$. No readout correction.

and $T_2^\star = 4.4(5)$ ms for nuclear spin 2 (Fig. 4.21). An electron free-precession (Ramsey-type) measurement is performed during the experiments (interleaved on a μs timescale), so that the electron and nuclear $T_2^\star$ can be compared under the same magnetic field fluctuations.

We expect the nuclear dephasing time to be set by a combination of electron relaxation and magnetic field fluctuations (including the nuclear spin bath). Electron relaxation gives a rate of $\Gamma_{0,-1} + \Gamma_{0,+1} = 122(4)$ s^{-1} (time constant of 8.2 ms). To estimate the intrinsic nuclear dephasing timescale $T_{2int}^\star$ we subtract the electron depolarization rate from the inverse of the measured dephasing time $T_2^\star$. We find $T_{2int}^\star \sim 4.0$ ms for spin 1 and $T_{2int}^\star \sim 9.5$ ms for spin 2. The difference between values could originate from the differences in the nuclear spin's microscopic environments.

Magnetic field stability

We stabilize the magnetic field through a feedback loop by periodically measuring the energy splitting of the NV centre. This stabilization is required to counteract slow magnetic field drifts (order of 0.1 G) over the measurement time. Figure 4.22 characterizes the magnetic field stability during the quantum-error-correction measurements with simultaneous errors (taken over a total of 344 hours, spread out over 1 month). These values are representative for the other measurements.

The measured residual slow fluctuations of the magnetic field (38.7 kHz, 0.014 G) are small compared to the fast fluctuations due to the ^{13}C bath ($\sim$ 66 kHz, 0.024 G). These slow fluctuations are expected to decrease the electron $T_{2e}^\star$ from the instantaneous value 3.3 μs to 2.9 μs (and the nuclear $T_2^\star$ with approximately the same factor).

Part of the fluctuations are caused by the uncertainty in the measurements of the electron splitting. Figure 4.22 shows that this effect is small, because the measurement uncertainty of (6.9 kHz) is small compared to the total drift observed (38.7 kHz).

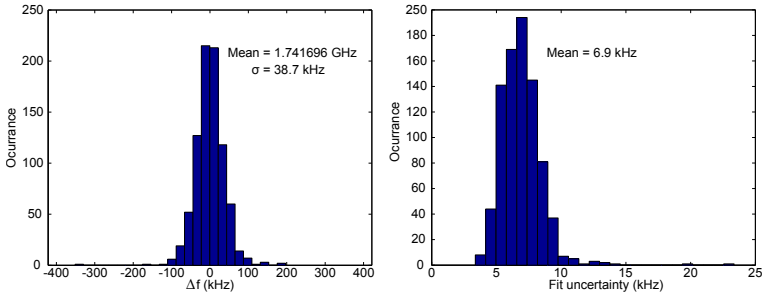


Figure 4.22 —Magnetic field stabilization. The magnetic field during the error correction measurements was stabilized by a feedback loop based on 840 measurements. (left) Electron energy splitting. Fluctuations during the experiment of 38.7 kHz (1σ) are observed, corresponding to 14 mG. (right) The average measurement uncertainty in a single instance of the magnetic field measurement is 6.9 kHz (2 mG).

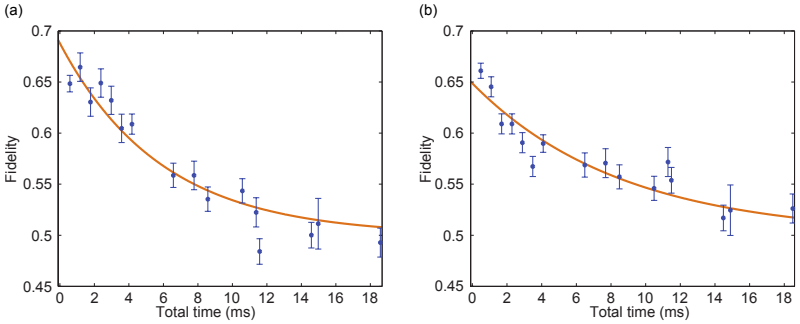


Figure 4.23 —Nuclear spin echo experiments. a, For nuclear spin 1: $T_2 = 5.9(8)$ ms. **b,** For nuclear spin 2: $T_2 = 9(1)$ ms. Single exponential fits. No readout or initialization correction.

Nuclear T_2

The nuclear spin coherence times can be extended by decoupling from the spin bath. Figure 4.23 shows the results of nuclear spin echo experiments. The required pi-pulse is constructed in the same way as all nuclear gates in this work. The electron is prepared in $m_s = 0$ and re-initialized before the pi-pulse, which makes it possible to use a conditional gate, and re-initialized again to be used in the final measurement. We find $T_2 = 5.9(8)$ ms (nuclear spin 1) and $T_2 = 9(1)$ ms (nuclear spin 2).

Nuclear dephasing $T_2^\star$ and depolarization T_1 under laser illumination

Being able to re-initialize the electron spin without depolarizing or dephasing the nuclear spins is essential for initializing the multi-qubit register and for performing partial measurements within such registers.

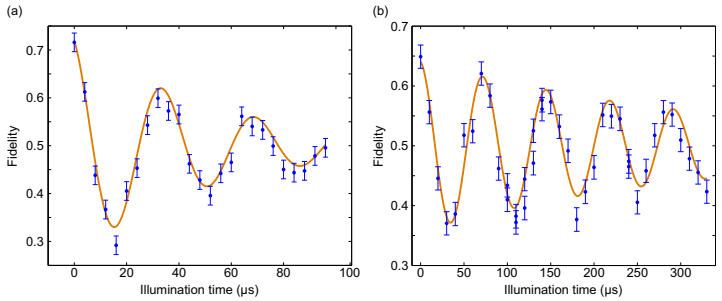


Figure 4.24 —Nuclear Ramseys and $T_2^\star$ under illumination. **a,** Nuclear spin 1, $T_2^\star = 51(7)$ μs. **b,** Nuclear spin 2, $T_2^\star = 0.35(9)$ ms. The laser power is the same as used in the initialization, re-initialization and readout steps. No readout or initialization correction.

Figure 4.24 shows a $T_2^\star$ under illumination of 51(7) μs for nuclear spin 1 and 0.35(9) ms for nuclear spin 2. These times are long compared to the time required to re-initialize the electron spin (~ 2 μs). For example, for nuclear spin 1 this predicts a contrast loss of approximately $1 - e^{-2/50} = 0.04$.

Figure 4.25 shows nuclear relaxation measurements for both spins with and without laser illumination. The nuclear spin is prepared in $|0\rangle$ and the electron spin in $m_s = 0$. We let the system relax for a variable time during which the laser is either on or off. For the experiment without laser illumination, the electron is reset by a short laser pulse (2 μs) so that it can be used to measure the nuclear spin state. Without illumination, we find $T_1 = 0.04(1)$ s and $T_1 = 21(5)$ ms for spin 1 and 2 respectively. With illumination, we find $T_1 = 2.5(3)$ ms and $T_1 = 1.2(2)$ ms for spin 1 and 2 respectively.

The nuclear depolarization during laser illumination is slow compared to the time it takes to re-initialize the electron spin (~ 2 μs), so that the electron can be re-initialized without depolarizing the nuclei. Note that the final signal approaches a fidelity of 0.5; prolonged laser light does not create a preferential polarization for these nuclear spins.

4.6.10 Fidelity estimates

The decoherence processes above decrease the ultimate fidelities of the protocols implemented in the main text. Here we provide estimates for the expected fidelities based on the above decoherence effects.

Quantum error correction

The estimates for the final fidelities for the three-qubit quantum-error-correction protocol in the main text are obtained from the electron decoherence time ($T_{coh} = 2.86(4)$ ms) and the two nuclear spin intrinsic dephasing times ($T_{2int}^\star \sim 4.0$ ms and $T_{2int}^\star \sim 9.5$). We approximate all three processes by rates and add them to obtain a final decay time $T_{est} = 1.4$ ms. The typical state fidelity for the 1.8 ms quantum error correction protocol

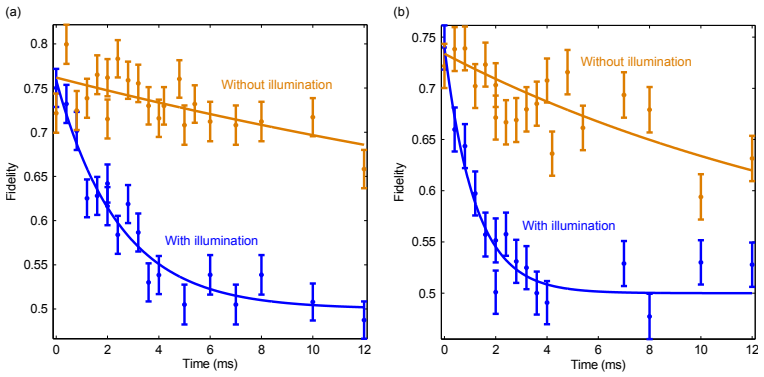


Figure 4.25 —Nuclear T1 with and without illumination. Lines are exponential fits. **a,** nuclear spin 1. **b,** nuclear spin 2. The laser power is the same as used in the initialization, re-initialization and readout steps. No readout correction.

becomes $F_{est} = e^{-1.8/T_{est}}/2 + 1/2 = 0.64$. This corresponds to an estimated process fidelity $F_{p,est} = 6F_{est}/4 - 1/2 = 0.46$, similar to the observed value. The average state fidelity loss per gate for the 10 nuclear gates in the error correction protocol is estimated from $F_{average} = 1/2\ \sqrt[10]{2F_{est} - 1} + 1/2 = 0.94$.

Nuclear initialization

The nuclear initialization protocol for spin 1 takes approximately 340 μs. As only two qubits are involved we add the rates for the electron decoherence and spin 1 to obtain $F_{1,est} = 0.91$ as the estimated initialization fidelity. In the same way we obtain $F_{2,est} = 0.94$ (time: 280 μs) for spin 2.

Entangling gate

The entangling gate takes 0.986 ms. Following the calculation for the error correction protocol, and including additional loss due to the nuclear $T_2^\star$ under illumination during the 2 μs electron reset, we find $F_{est} = 0.74$.

4.7 Bibliography

[1] D. D. Awschalom, L. C. Bassett, A. S. Dzurak, E. L. Hu and J. R. Petta. Quantum Spintronics: Engineering and Manipulating Atom-Like Spins in Semiconductors. *Science* **339**, 1174 (2013).

[2] W. F. Koehl, B. B. Buckley, F. J. Heremans, G. Calusine and D. D. Awschalom. Room temperature coherent control of defect spin qubits in silicon carbide. *Nature* **479**, 84 (2011).

[3] C. Yin *et al.* Optical addressing of an individual erbium ion in silicon. *Nature* **497**, 91 (2013).

[4] M. V. G. Dutt *et al.* Quantum Register Based on Individual Electronic and Nuclear Spin Qubits in Diamond. *Science* **316**, 1312 (2007).

[5] P. Neumann *et al.* Multipartite Entanglement Among Single Spins in Diamond. *Science* **320**, 1326 (2008).

[6] G. D. Fuchs, G. Burkard, P. V. Klimov and D. D. Awschalom. A quantum memory intrinsic to single nitrogen-vacancy centres in diamond. *Nature Physics* **7**, 789 (2011).

[7] T. van der Sar *et al.* Decoherence-protected quantum gates for a hybrid solid-state spin register. *Nature* **484**, 82 (2012).

[8] P. C. Maurer *et al.* Room-Temperature Quantum Bit Memory Exceeding One Second. *Science* **336**, 1283 (2012).

[9] W. Pfaff *et al.* Demonstration of entanglement-by-measurement of solid-state qubits. *Nature Physics* **9**, 29 (2013).

[10] J. J. Pla *et al.* High-fidelity readout and control of a nuclear spin qubit in silicon. *Nature* **496**, 334 (2013).

[11] F. Dolde *et al.* Room-temperature entanglement between single defect spins in diamond. *Nature Physics* **9**, 139 (2013).

[12] L. Jiang *et al.* Repetitive Readout of a Single Electronic Spin via Quantum Logic with Nuclear Spin Ancillae. *Science* **326**, 267 (2009).

[13] S.-Y. Lee *et al.* Readout and control of a single nuclear spin with a metastable electron spin ancilla. *Nature Nanotechnology* **8**, 487 (2013).

[14] D. G. Cory *et al.* Experimental Quantum Error Correction. *Physical Review Letters* **81**, 2152 (1998).

[15] O. Moussa, J. Baugh, C. A. Ryan and R. Laflamme. Demonstration of Sufficient Control for Two Rounds of Quantum Error Correction in a Solid State Ensemble Quantum Information Processor. *Physical Review Letters* **107**, 160501 (2011).

[16] P. Schindler *et al.* Experimental Repetitive Quantum Error Correction. *Science* **332**, 1059 (2011).

[17] M. D. Reed *et al.* Realization of three-qubit quantum error correction with superconducting circuits. *Nature* **482**, 382 (2012).

[18] H. Bernien *et al.* Heralded entanglement between solid-state qubits separated by three metres. *Nature* **497**, 86 (2013).

[19] N. H. Nickerson, Y. Li and S. C. Benjamin. Topological quantum computing with a very noisy network and local error rates approaching one percent. *Nature Communications* **4**, 1756 (2013).

[20] P. Neumann *et al.* Single-Shot Readout of a Single Nuclear Spin. *Science* **329**, 542 (2010).

[21] L. Robledo *et al.* High-fidelity projective read-out of a solid-state spin quantum register. *Nature* **477**, 574 (2011).

[22] A. Dréau, P. Spinicelli, J. R. Maze, J.-F. Roch and V. Jacques. Single-Shot Readout of Multiple Nuclear Spin Qubits in Diamond under Ambient Conditions. *Physical Review Letters* **110**, 060502 (2013).

[23] T. H. Taminiau *et al.* Detection and Control of Individual Nuclear Spins Using a Weakly Coupled Electron Spin. *Physical Review Letters* **109**, 137602 (2012).

[24] S. Kolkowitz, Q. P. Unterreithmeier, S. D. Bennett and M. D. Lukin. Sensing Distant Nuclear Spins with a Single Electron Spin. *Physical Review Letters* **109**, 137601 (2012).

[25] N. Zhao *et al.* Sensing single remote nuclear spins. *Nature Nanotechnology* **7**, 657 (2012).

[26] J. S. Hodges, J. C. Yang, C. Ramanathan and D. G. Cory. Universal control of nuclear spins via anisotropic hyperfine interactions. *Physical Review A* **78**, 010303 (2008).

[27] Y. Zhang, C. A. Ryan, R. Laflamme and J. Baugh. Coherent Control of Two Nuclear Spins Using the Anisotropic Hyperfine Interaction. *Physical Review Letters* **107**, 170503 (2011).

[28] J. R. Maze, J. M. Taylor and M. D. Lukin. Electron spin decoherence of single nitrogen-vacancy defects in diamond. *Physical Review B* **78**, 094303 (2008).

[29] P. London *et al.* Detecting and Polarizing Nuclear Spins with Double Resonance on a Single Electron Spin. *Physical Review Letters* **111**, 067601 (2013).

[30] V. Filidou *et al.* Ultrafast entangling gates between nuclear spins using photoexcited triplet states. *Nature Physics* **8**, 596 (2012).

[31] T. H. Taminiau, J. Cramer, T. v. d. Sar, V. V. Dobrovitski and R. Hanson. Universal control and error correction in multi-qubit spin registers in diamond. *Nature Nanotechnology* **9**, 171 (2014).

[32] N. Bar-Gill, L. M. Pham, A. Jarmola, D. Budker and R. L. Walsworth. Solid-state electronic spin coherence time approaching one second. *Nature Communications* **4**, 1743 (2013).

[33] H. Bernien *et al.* Two-Photon Quantum Interference from Separate Nitrogen Vacancy Centers in Diamond. *Physical Review Letters* **108**, 043604 (2012).

[34] B. Smeltzer, J. McIntyre and L. Childress. Robust control of individual nuclear spins in diamond. *Physical Review A* **80**, 050302 (2009).

[35] V. Jacques *et al.* Dynamic Polarization of Single Nuclear Spins by Optical Pumping of Nitrogen-Vacancy Color Centers in Diamond at Room Temperature. *Physical Review Letters* **102**, 057403 (2009).

[36] N. Aslam, G. Waldherr, P. Neumann, F. Jelezko and J. Wrachtrup. Photo-induced ionization dynamics of the nitrogen vacancy defect in diamond investigated by single-shot charge state detection. *New Journal of Physics* **15**, 013064 (2013).

[37] G.-Q. Liu, H. C. Po, J. Du, R.-B. Liu and X.-Y. Pan. Noise-resilient quantum evolution steered by dynamical decoupling. *Nature Communications* **4**, 2254 (2013).

Chapter 5

Repeated quantum error correction on a continuously encoded qubit by real-time feedback

J. Cramer, N. Kalb, M. A. Rol, B. Hensen, M. S. Blok, M. Markham, D. J. Twitchen, R. Hanson, T. H. Taminiau

Reliable quantum information processing in the face of errors is a major fundamental and technological challenge. Quantum error correction protects quantum states by encoding a logical quantum bit (qubit) in multiple physical qubits. To be compatible with universal fault-tolerant computations, it is essential that states remain encoded at all times and that errors are actively corrected. Here we demonstrate such active error correction on a continuously protected logical qubit using a diamond quantum processor. We encode the logical qubit in three long-lived nuclear spins, repeatedly detect phase errors by non-destructive measurements, and apply corrections by real-time feedback. The actively error-corrected qubit is robust against errors and encoded quantum superposition states are preserved beyond the natural dephasing time of the best physical qubit in the encoding. These results establish a powerful platform to investigate error correction under different types of noise and mark an important step towards fault-tolerant quantum information processing.

The results in this chapter have been published in *Nature Communications* **7**, 11526 (2016).

5.1 Introduction

Large-scale quantum information processing requires the correction of errors during computations. In quantum error correction a logical quantum bit (qubit) is encoded in a subspace of multiple physical qubits so that errors can be actively corrected without affecting the encoded information. A promising way to correct errors in encoded quantum states is to perform feedback based on multi-qubit measurements known as stabilizer measurements [1–3] (see Fig. 5.1a). These measurements are performed non-destructively using extra qubits (ancillas) and are frequently repeated to detect errors before they accumulate. The measurement outcomes are then processed in classical logic that identifies the error syndrome, and, in order to enable universal computations [1], active feedback is applied to the encoded system to correct errors where needed. The key experimental challenge is to perform such complete error-correction cycles including non-destructive stabilizer measurements and real-time feedback well within the coherence time.

Quantum-error-correction protocols have been explored across a range of platforms [4–14]. Pioneering experiments bypassed stabilizer measurements by reversing the encoding to correct errors, thus leaving the quantum state unprotected [5–11]. Recent breakthroughs have enabled the use of stabilizer measurements to passively track errors in quantum states and retrieve stored information afterwards through post processing [12–15].

Here we realize complete rounds of active quantum error correction on a continuously encoded logical qubit by exploiting newly-developed stabilizer measurements based on an electron spin ancilla with high-fidelity non-demolition readout, by encoding in long-lived nuclear spins, and by applying real-time correction of errors through fast classical logic. We show that the actively error-corrected logical qubit is robust against errors and that multiple rounds of error correction prevent errors from accumulating. Finally, by correcting time-correlated phase errors naturally induced by the environment, we demonstrate that encoded quantum superposition states are preserved beyond the dephasing time of the best physical qubit used in the encoding.

5.2 Error correction code

The three-qubit code considered here corrects a single phase error on any one of the physical qubits. To protect against such errors, we encode the logical qubit in states for which all physical qubits have the same phase: $|\psi\rangle_L = \alpha\,|0\rangle_L + \beta\,|1\rangle_L$ with $|0\rangle_L = (|{+}\mathrm{X}\rangle_1|{+}\mathrm{X}\rangle_2|{+}\mathrm{X}\rangle_3 + |{-}\mathrm{X}\rangle_1|{-}\mathrm{X}\rangle_2|{-}\mathrm{X}\rangle_3)/\sqrt{2}$, $|1\rangle_L = (|{+}\mathrm{X}\rangle_1|{+}\mathrm{X}\rangle_2|{+}\mathrm{X}\rangle_3 - |{-}\mathrm{X}\rangle_1|{-}\mathrm{X}\rangle_2|{-}\mathrm{X}\rangle_3)/\sqrt{2}$ and $|{\pm}\mathrm{X}\rangle = (|0\rangle \pm |1\rangle)/\sqrt{2}$. Errors ($Z$ operations) are detected by measuring the two stabilizer generators $X_1X_2I_3$ and $I_1X_2X_3$ via an ancilla. These measurements respectively compare the phases of qubit 1 & 2 and qubit 2 & 3. For an uncorrupted state both measurements yield outcome +1 (same phase, no error), but for a phase error on just one of the qubits the two measurements give a unique syndrome of -1 outcomes that identifies the error. For example, an error on the first qubit results in outcome -1 for the first stabilizer measurement and outcome +1 for the second. The logical qubit operators are $X_L = X_1I_2I_3$, $Y_L = Y_1Z_2Z_3$ and $Z_L = Z_1Z_2Z_3$ (or their permutations).

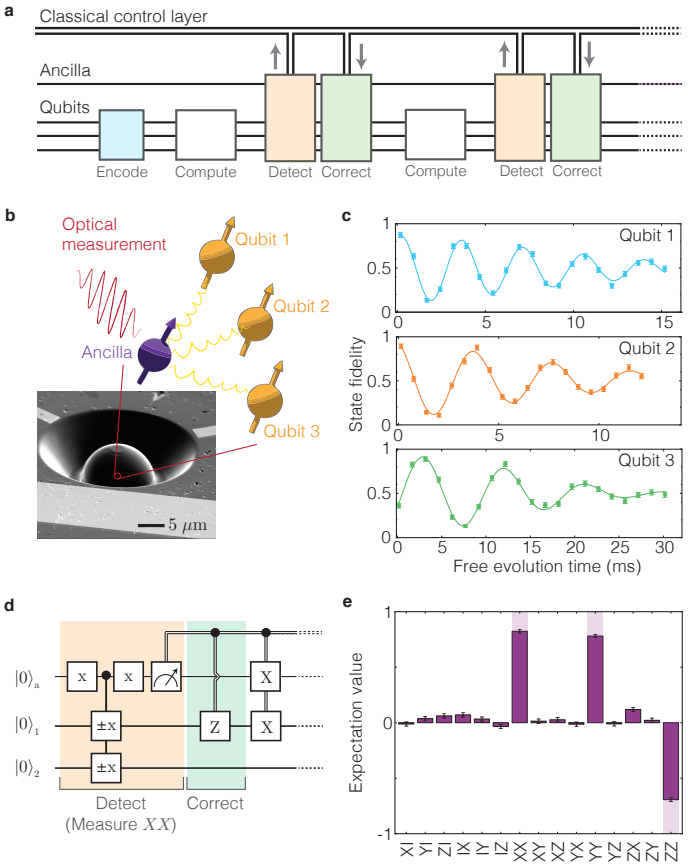


Figure 5.1 — Quantum error correction and implementation of stabilizer measurements. a, A quantum state is encoded in a logical qubit consisting of three physical qubits. Errors inevitably occur, for example during computations. An ancilla is used to repeatedly perform measurements that detect errors. Errors are corrected through classical logic and feedback, while the quantum state remains coherent and encoded. **b**, Device: CVD-grown single-crystal diamond with a solid-immersion lens[16] and on-chip lines for microwave control. Scale bar: 5 μm. Ancilla: the optically addressable electronic spin of a nitrogen vacancy (NV) centre. Qubits: three ^{13}C nuclear spins that are controlled and measured through the hyperfine coupling to the ancilla (Sec. 5.8.2). **c**, Free induction decay (Ramsey) experiments. Gaussian fits yield dephasing times $T_2^* = 12.0(9)$, 9.1(6) and 18.2(9) ms for qubits 1, 2 and 3, respectively. **d**, Deterministic entanglement of two qubits by XX stabilizer measurement and feedback. The $\pm x$ gates are $\pi/2$ rotations around x with the sign controlled by the ancilla state. The final operations reset the ancilla and account for an additional flip for the $+1$ outcome (Sec. 5.8.3). **e**, State tomography of the generated entangled state for qubits 2 and 3. The fidelity with the ideal state is $F = 0.824(7)$ (see Fig. 5.10 for other qubit combinations and post-selected results). All error bars are one statistical s.d.

5.3 Stabilizer measurements and real-time feedback

Our qubits are three ^{13}C nuclear spins ($I = 1/2$, 1.1% abundance) surrounding a single nitrogen-vacancy (NV) centre in diamond, whose electronic spin we use as ancilla ($S = 1$; $|0\rangle_a : m_s = 0$ and $|1\rangle_a : m_s = -1$) (Fig. 5.1b). At 4 K, the ancilla combines fast control[17], optical single-shot readout[18] and long coherence times[19] (> 25 ms, Sec. 5.8.1). We use relatively remote nuclear qubits (coupling to the ancilla 20-50 kHz) that are robust against optical excitation of the ancilla and design decoherence-protected gates to control them[9,20] (Sec. 5.8.2). All three qubits show long dephasing times T_2^* with the dominant natural errors being phase errors (Fig. 5.1c).

The key challenge for implementing stabilizer measurements in this system is that the ancilla-qubit interaction is always present: imperfect knowledge of the ancilla state during or after readout dephases the qubits[21–23]. To minimize this dephasing, we implement quantum non-demolition measurements of the ancilla by resonant optical excitation of $|0\rangle_a$ and stopping the excitation within 2 μs upon photon detection (outcome $|0\rangle_a$) to minimize uncontrolled spin flips in the optically excited state[24] (Sec. 5.8.1). The resulting readout fidelities are $F_0 = 0.890(4)$ for $|0\rangle_a$ and $F_1 = 0.988(2)$ for $|1\rangle_a$ (average: $F = 0.939(2)$). Crucially, the post-measurement fidelity after correctly assigning $|0\rangle_a$ is 0.992, demonstrating the desired non-demolition character.

To benchmark the stabilizer measurements and real-time feedback, we deterministically entangle two qubits by projecting into a Bell state, i.e. a simultaneous eigenstate of XX and ZZ[22,25,26]. First, the qubits are initialized in $|00\rangle$, an eigenstate of ZZ, with fidelity 0.910(6). Then a XX stabilizer measurement projects the qubits onto one of two Bell states (Fig. 5.1d). We interpret the -1 outcome as an error in the desired state and correct it through feedback before performing two-qubit tomography. The deterministically generated entangled state, with fidelity $F = 0.824(7)$ (Fig. 5.1e), demonstrates the non-destructive nature of the measurement; coherence within the subspaces is maintained throughout the measurement and feedback cycle. The complete cycle can be repeated up to 6 times within the shortest qubit T_2^*.

5.4 Active quantum error correction on a logical qubit

We now turn to quantum error correction by stabilizer measurements. The logical qubit is encoded by mapping an arbitrary state $|\psi\rangle_a = \alpha|0\rangle_a + \beta|1\rangle_a$ prepared on the ancilla to the three-qubit state $|\psi\rangle_L = \alpha|0\rangle_L + \beta|1\rangle_L$ (Fig. 5.2a). We characterize the encoding by preparing six basis states $|0\rangle_L$, $|1\rangle_L$, $|\pm\mathrm{X}\rangle_L = (|0\rangle_L \pm |1\rangle_L)/\sqrt{2}$ and $|\pm\mathrm{Y}\rangle_L = (|0\rangle_L \pm i|1\rangle_L)/\sqrt{2}$ and performing three-qubit state tomography. The fidelities with the ideal states confirm successful encoding and genuine three-qubit entanglement (Fig. 5.2b).

We first investigate the recovery of arbitrary logical qubit states from phase errors. To emulate a general process causing dephasing, uncorrelated incoherent errors are applied with variable probability p_e to each physical qubit simultaneously (Fig. 5.3a); for each qubit the error process is $E(\rho) = (1 - p_e)I\rho I + p_e Z\rho Z$, with ρ the single-qubit density matrix. By controllably applying such errors we characterize the effectiveness of the error correction for any process causing uncorrelated errors with equal probability to the qubits. We then

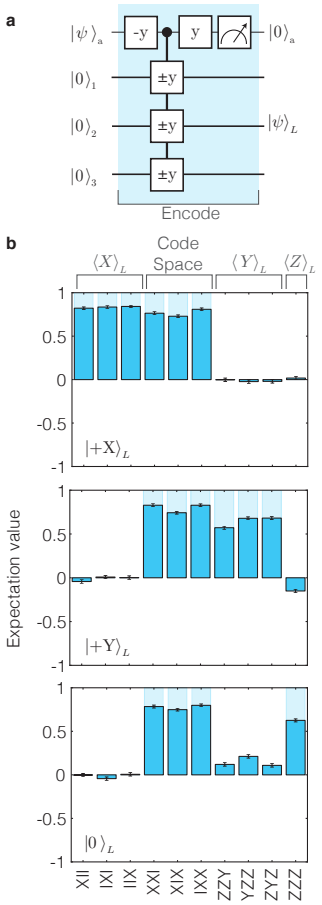


Figure 5.2 — Encoding of the logical qubit. a, Encoding an arbitrary quantum state $|\psi\rangle = \alpha\,|0\rangle + \beta\,|1\rangle$ prepared on the ancilla into $|\psi\rangle_L = \alpha\,|0\rangle_L + \beta\,|1\rangle_L$. Successful encoding is heralded by outcome $|0\rangle_a$. **b**, Characterization of the logical states $|+X\rangle_L$, $|+Y\rangle_L$ and $|0\rangle_L$. Only the logical qubit operators and stabilizers are shown (see Fig. 5.11 for complete tomography of all 6 logical basis states). The fidelities with the ideal three-qubit states are $F = 0.810(5)$, $0.759(5)$ and $0.739(5)$, respectively, demonstrating three-qubit entanglement[10]. The logical state fidelities are $F_{+X} = (1 + \langle X_L\rangle)/2 = 0.916(6)$, $F_{+Y} = (1 + \langle Y_L\rangle)/2 = 0.822(7)$ and $F_0 = (1 + \langle Z_L\rangle)/2 = 0.813(9)$. Ideally, all the encoded states are $+1$ eigenstates of the stabilizers $X_1X_2I_3$ and $I_1X_2X_3$. The fidelity to this code space, $F_S = (1 + \langle X_1X_2I_3\rangle + \langle I_1X_2X_3\rangle + \langle X_1I_2X_3\rangle)/4$, is $0.839(3)$ averaged over all states and gives the probability that the starting state is free of detectable errors. All error bars are one statistical s.d.

measure the stabilizers $X_1X_2I_3$ and $I_1X_2X_3$, identify potential errors and correct them through feedback. The probabilities to obtain the four different error syndromes (inset in Fig. 5.3b) show the expected symmetry around $p_e = 0.5$ and match the theoretical prediction based on the errors present in the initial states (Fig. 5.2b) and the average ancilla readout fidelity.

The protection of the logical qubit is characterized by the process fidelity with the identity (Fig. 5.3b) (Sec. 5.8.4). We quantitatively analyse the results by fitting to $wF_{QEC} + (1 - w)F_{linear}$, where $F_{QEC}(p_e)$ and $F_{linear}(p_e)$ are the theoretical curves with and without error correction ($w = 1$ indicates ideal robustness against applied single-qubit errors). When no error correction is applied we observe the expected linear dependence on the error probability: $w \approx 0$. In contrast, with quantum error correction w is 0.81(3), and a non-linear curve shape that is characteristic for robustness against single-qubit errors is obtained. This result demonstrates that the entropy associated to the applied errors is successfully removed from the system.

Comparisons to an unencoded qubit and the logical qubit without error correction reveal that adding quantum error correction on top of a computation does not yet provide a net improvement (Fig. 5.3b), due to additional errors introduced by the initialization, encoding and stabilizer measurements (total of 13 two-qubit gates, 488 ancilla refocusing pulses and 6 ancilla readouts/resets). To isolate the errors due to the stabilizer measurements, we compare the error-corrected logical qubit to the logical qubit left idle. We further optimize the error correction, by assigning the ancilla state with the best readout fidelity ($|1\rangle_a$, $F_1 = 0.988(2)$) to the most likely error syndrome (+1, +1 - no error, inset Fig. 5.3b), instead of averaging over all assignments as in Fig. 5.3b. With this improvement, error correction outperforms idling for a range of p_e (Fig. 5.3c); once the logical qubit is encoded, quantum error correction can be beneficial.

5.5 Multiple rounds of active error correction

Because a complete round of error correction (2.99 ms) fits well within the dephasing time of the physical qubits, we can concatenate multiple rounds to improve the coherence of continuously encoded quantum superpositions by preventing the accumulation of errors (Fig. 5.4a). Three new elements are introduced. First, the total error probability p_e is distributed over n rounds, so that the error probability per round is $p_n = (1 - \sqrt[n]{1 - 2p_e})/2$ (Sec. 5.8.4). This error model corresponds to errors occurring incoherently, for example with a constant rate in time. Second, to investigate dephasing we focus on the protection of the two states $|\pm\mathrm{X}\rangle_L = |\pm\mathrm{X}, \pm\mathrm{X}, \pm\mathrm{X}\rangle$ (i.e. a classical bit stored in the phase of a quantum superposition). Third, we exploit the intrinsic robustness of the logical qubit to single Z errors by redefining $X_L = (X_1I_2I_3 + I_1X_2I_3 + I_1I_2X_3 - X_1X_2X_3)/2$, which is equivalent to performing a round of error correction by majority voting at the end of the experiment [13].

For a single round of error correction (majority vote only) the average fidelity is higher than for an unencoded qubit for any p_e (Fig. 5.4b); adding more (identical) qubits is always beneficial in the repetition code. For $p_e = 0$, additional rounds of quantum error correction can only introduce errors, reducing the fidelity (Fig. 5.4b). For larger p_e, however, multiple rounds prevent errors from accumulating by dividing the error process in parts that are

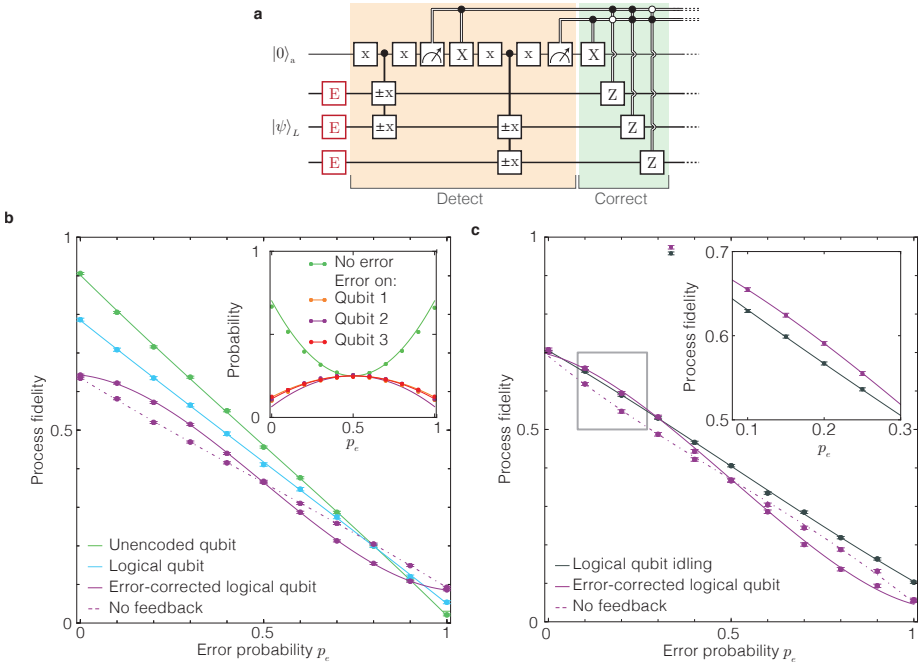


Figure 5.3 — Active quantum error correction by stabilizer measurements. a, All qubits are simultaneously subjected to uncorrelated phase errors E with probability p_e. Errors are detected by measuring $X_1X_2I_3$ and $I_1X_2X_3$ and subsequently corrected by Z operations through feedback. Finally we measure the process fidelity with the identity. **b**, Process fidelities for: an unencoded qubit (averaged over the three qubits), the logical qubit without stabilizer measurements, the error-corrected logical qubit, and the logical qubit without feedback (i.e. errors are detected but not corrected). We average over the logical qubit permutations, e.g. $X_L = X_1I_2I_3$, $I_1X_2I_3$ and $I_1I_2X_3$, and the four ways to assign the ancilla states to the error syndromes (see Fig. 5.12 for individual curves). Inset: probabilities for the error syndromes with theoretically predicted curves based on the state tomography in Fig. 5.2b (Sec. 5.8.5). **c**, Comparison between the error-corrected logical qubit and the logical qubit with the stabilizer measurements replaced by an equivalent idle time (2.99 ms). Compared to **b**, the effective readout fidelity is optimized by associating syndrome +1,+1 (no error) to obtaining $|1\rangle_a$ for both stabilizer measurements. Curves in **b** and **c** are fits described in Sec. 5.8.4. All error bars are one statistical s.d.

more likely to contain only single errors, which are corrected. In addition, unlike error detection with post-processing[13,14], active correction between rounds keeps the probability to obtain +1 (no error) high (inset Fig. 5.4b) and thus maintains the advantage of assigning the highest-fidelity ancilla readout to that outcome. Preventing errors by maximizing the probability that the ancilla qubits reside in the optimal state is a key general advantage of real-time feedback in quantum error correction. As a result, for $p_e > 0.3$, multiple rounds outperform a single round of error correction.

5.6 Correcting natural dephasing

Finally, as an example of suppressing errors naturally present in the environment, we let the qubits evolve freely instead of applying errors (Fig. 5.4c). The resulting errors are still spatially uncorrelated across the qubits, but the error probabilities are now different for each qubit because their intrinsic T_2^* differ due to their local environments (Fig. 5.14c). In addition, the errors arise from quasi static detunings due to the slowly fluctuating ^{13}C spin bath so that the errors in a given experimental run evolve coherently and are correlated in time. Like most environmental errors, such errors might also be suppressed by other methods than quantum error correction, for example by polarizing the spin environment[27,28], by refocusing pulses[29] or by isotopic purification[29–32].

The fidelity for the logical qubit with majority voting again starts above the best unencoded qubit, but drops below it for larger evolution times (Fig. 5.4d). Because the error probabilities vary between qubits, an error detected on the best qubit becomes more likely to actually correspond to errors on both other qubits and the wrong correction is made. An additional round of quantum error correction in the middle of the evolution time now not only prevents errors from accumulating by intermediately correcting them, but also interrupts any coherent build-up by projecting the errors, thus suppressing them (Fig. 5.4d). Due to this combination, the logical qubit shows an enhanced dephasing time (24.2(2) ms against 18.2(9) ms for the best physical qubit) and yields the highest average state fidelity for total evolution times between 5 and 19 ms (Fig. 5.4d). This result demonstrates an actively error-corrected logical qubit with an improved dephasing time over the best qubit used in the encoding.

5.7 Discussion

The presented non-destructive measurements and real-time feedback on encoded quantum states are the key primitives for universal computations on logical qubits and for error-correcting codes that correct both phase and bit-flip errors. To reach scalability thresholds, readout and gate fidelities should be further increased, for example by: improving the optical collection efficiency through optical cavities[33], enhancing coherence times through implantation or selective growth of defects and isotopes in purified diamonds[29,30], and improving gate design through optimal control[34]. In a wider perspective, our results can be combined with recently demonstrated entanglement between distant NV centres[35,36] to form quantum networks with error-corrected nodes for entanglement purification, quantum communication and networked quantum computation[37]. Therefore, these results establish a promising platform to experimentally investigate protocols for fault-tolerant quantum information processing under different types of noise and error correlations in diverse settings.

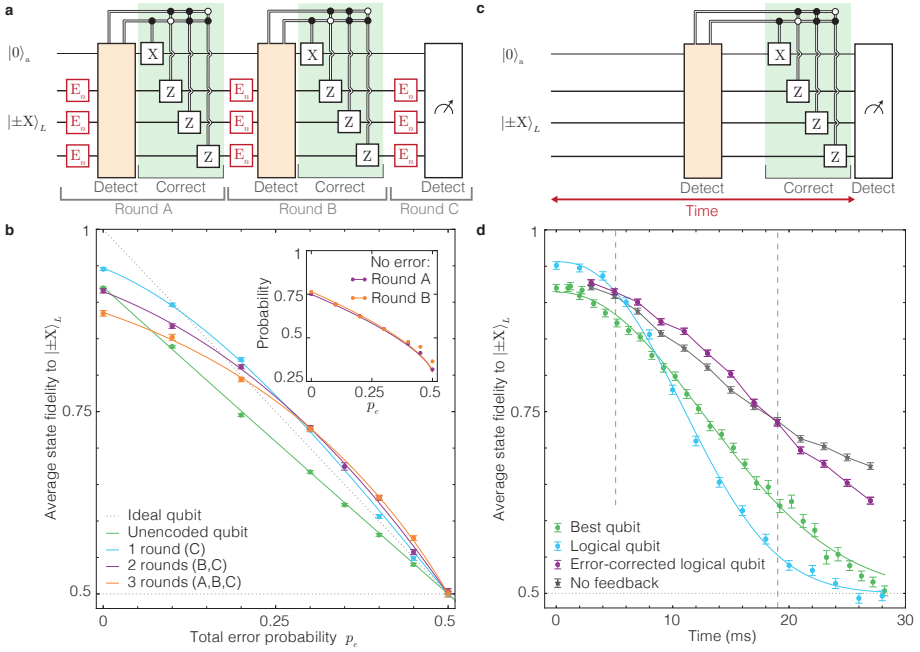


Figure 5.4 — Extending coherence by active quantum error correction. **a**, Three rounds of error correction on a logical qubit. The first two rounds of quantum error correction use stabilizer measurements and feedback. The final round is implemented by majority voting. **b**, Average logical state fidelity for $|+X\rangle_L$ and $|-X\rangle_L$ as a function of total error probability p_e for $n = 1$, 2 and 3 rounds of error correction compared to an unencoded qubit. The errors per round occur with probability p_n. Inset: probabilities that no error is detected ($n = 3$). The similarity of the results for rounds A and B confirms that errors are corrected in between rounds. **c**, Correcting natural dephasing. The storage time is defined from the end of the encoding until the start of the final measurements. **d**, Dephasing of the logical qubit: without stabilizer measurements, with quantum error correction and without feedback, compared to the best unencoded qubit. The dashed lines indicate the times between which the actively error-corrected logical qubit gives the highest fidelity. The data without feedback (detecting errors without correcting) isolates the suppression of coherently evolving errors by projecting them. For long times, applying error correction lowers the fidelity because the stabilizer measurements extract no useful information about errors, but nevertheless preferentially suppress evolutions that result in phase errors at the end of the sequence (See Fig. 5.14 for a detailed analysis). See Fig. 5.13 for error syndrome probabilities. Solid curves in **b** and **d** are fits described in Secs. 5.8.4, 5.8.4 and 5.8.5. Dashed lines are a guide to the eye. All error bars are one statistical s.d.

5.8 Methods and theoretical analysis

In this section we will discuss relevant background methods and on the the presented results. Figures corresponding to the following subsections are displayed on pages 105-115.

5.8.1 Sample and Setup

We use a naturally occurring Nitrogen-Vacancy (NV) in high-purity type IIa chemical-vapor-deposition (CVD) grown diamond with a 1.1% natural abundance of ^{13}C and a $< 111 >$ crystal orientation (Element Six). To enhance the collection efficiency a solid-immersion lens was fabricated on top of the NV centre[16,18] (Fig. 5.1b) and a single-layer aluminum-oxide anti-reflection coating was deposited[35,38]. The sample temperature is $T \approx 4.2$ K and a magnetic field of 403.553(3) G is applied along the NV symmetry axis.

The ancilla NV electron spin is characterized by a Rabi frequency of 4.3 MHz, a dephasing time T_2^*=4.6(2) μs, a Hahn echo time $T_2 = 1.03(3)$ ms and a longitudinal relaxation time of 0.43(6) s (due to microwave noise and laser background). The coherence time of the ancilla under dynamical decoupling exceeds 25 ms and does not limit the experiments (Fig. 5.5). We initialize and readout the ancilla through resonant excitation of the zero-phonon transitions of the NV centre (Fig. 5.6). Prior to every experiment the ^{14}N nuclear spin is initialized by measurement with a fidelity of $F_N = 0.94(3)$ in $m_I = -1$[18]. No external electric fields are applied: the gates in Fig. 5.1b are grounded.

5.8.2 Nuclear spin qubit control

The hyperfine interactions for the three nuclear spins are estimated by dynamical decoupling spectroscopy[9] (Tab. 5.1). Building on previous gate designs[9], nuclear gates are realized by applying sequences of π-pulses on the electron spin of the form $(\tau - \pi - 2\tau - \pi - \tau)^{N/2}$. The number of pulses N sets the rotation angle. The inter-pulse delay 2τ determines which qubit is controlled and whether the rotation is conditional on the ancilla state. In contrast to previous work (Ch. 4) we allow the gates to be detuned, providing greater flexibility to optimize τ and N for gate selectivity and minimal discretization errors. The gate parameters are listed in Tabs. 5.1, 5.2.

The nuclear spins are initialized by swapping with the ancilla electron spin (Fig. 5.7) and are read out by mapping the required correlation to the ancilla before reading it out (Fig. 5.8). To obtain best estimates for the actual states, the results are corrected for the fidelity of the gates used in the final readout (tomography) (details in Sec. 5.8.6). Uncorrected data is shown in Fig. 5.15.

5.8.3 Feedback

Real-time feedback is implemented through a programmable microprocessor (ADwin Pro II) that controls the experimental sequence (Fig. 5.9). We exploit feedback in four different ways. First, detected phase errors are corrected directly after the stabilizer measurements. Note that analysing errors over multiple rounds[14] would additionally enable real-time correction of ancilla readout errors, but that this is not implemented here. Second, dependent on

the ancilla measurement outcome the qubits pick up a deterministic phase shift due to the hyperfine interaction, which is corrected in the same way. Third, for an odd number of +1 outcomes the operations in the stabilizer measurements imprint a bit flip on the logical qubit, which we correct by transforming the logical qubit basis in real time. Fourth, to start each measurement sequence with the ancilla in $|0\rangle_a$ it is flipped back to $|0\rangle_a$ when the previous measurement returned $|1\rangle_a$.

Importantly, we perform real-time feedback either by adapting the qubit bases for all subsequent gates and measurements (for correcting Z errors and for the logical qubit) or by absorbing the feedback operations into the next gate acting on the same qubit (for the ancilla). Therefore the physical control sequence is directly adapted based on the measurement outcomes without introducing any unnecessary gate operations that would cause additional errors. In the circuit diagrams we sometimes display the gates for the feedback separately for clarity.

5.8.4 Quantum error correction analysis

The process fidelity with the identity is given by $F_p = (F_0+F_1+F_{+X}+F_{-X}+F_{+Y}+F_{-Y}-2)/4$, with $F_\alpha = \langle\alpha|\rho_\alpha|\alpha\rangle$ the six fidelities of the final states ρ_α with the ideal states $|\alpha\rangle_L$. The results of Fig. 5.3 are analysed by fitting to $wF_{QEC}(p_e) + (1-w)F_{linear}(p_e)$, with $F_{QEC}(p_e) = O + A(1-3p_e^2+2p_e^3)$ and $F_{linear}(p_e) = O + A(1-p_e)$. A and O account for the experimental fidelities.

The state fidelities for multiple rounds of error correction and incoherent errors (Fig. 5.4b) are fitted to the same equation using $F_{QEC}(p_e) = \frac{1}{2}(1+A(1-6p_n^2+4p_n^3)^n)$, with n the number of rounds, $p_n = \frac{1}{2}\sqrt[n]{1-2p_e}$ the error per round, and $F_{linear}(p_e) = \frac{1}{2}(1+A(1-2p_e))$. The error per round p_n is obtained as follows. An error process with total error probability (p_e) reduces the expectation value by a factor of $(1-2p_e)$. For incoherent errors, a process can be divided in n equal rounds using $(1-2p_e) = (1-2p_n)^n$, which results in $p_n = (1-\sqrt[n]{1-2p_e})/2$ (for $p_e \leq 0.5$). In Fig. 5.3c and Fig. 5.4b, A depends on the error-probability p_e, because we optimize the effective readout fidelity by associating the most likely error syndrome to the best ancilla readout. Further details on all theoretical analysis, including the error syndrome probabilities and numerical simulations of Fig. 5.4d. are discussed below.

State and process fidelities

For ideal error correction the process fidelity to the identity as a function of error probability p_e for a single round of quantum error correction (QEC) is

$$F_{QEC}(p_e) = O + A(1-3p_e^2+2p_e^3). \tag{5.1}$$

The offset O and amplitude A account for the finite experimental state fidelities. Note that the value at $p_e = 0.5$, $F_{QEC}(p_e=0.5) = O + A/2$, is determined by the fidelity of the logical states $|0\rangle_L$ and $|1\rangle_L$, which are insensitive to phase errors. Without error correction a linear function

$$F_{linear} = O + A(1-p_e) \tag{5.2}$$

is expected. The experimental data can be fitted to a weighted sum of the two functions by:

$$F_P = wF_{QEC} + (1-w)F_{linear}. \tag{5.3}$$

The shape of the curve is set by w, which gives the relative weights of the equations for ideal error correction and for no error correction.

Assignment of ancilla states to the error syndrome: effective measurement fidelity F_{M}

In our experiment, the ancilla readout fidelity is asymmetric: $|1\rangle_a$ has a higher readout fidelity ($F_1 = 0.988(2)$) than $|0\rangle_a$ ($F_0 = 0.890(4)$). The effective measurement fidelity for error correction F_{M} is therefore determined by the probabilities to obtain $|0\rangle_a$ or $|1\rangle_a$, which depend on the assignment of the ancilla states ($|0\rangle_a$ or $|1\rangle_a$) to each stabilizer measurement outcome (+1 or -1) and the probabilities for different errors to occur. There are four different ways to assign the ancilla states to the error syndromes: the +1,+1 outcome (no error) can be set to result in $\{|0\rangle_a, |0\rangle_a\}$, $\{|0\rangle_a, |1\rangle_a\}$, $\{|1\rangle_a, |0\rangle_a\}$ or $\{|1\rangle_a, |1\rangle_a\}$. The probability to obtain outcome +1,+1 (no error) ideally is $1 - 3p_e + 3p_e^2$, while the probability to detect an error on a given qubit is $p_e - p_e^2$. With these probabilities, we obtain the effective QEC measurement fidelity as function of error probability:

$$\begin{aligned} F_{\mathrm{M}} &= F^{(0)}(1 - 3p_e + 3p_e^3) + (F^{(1)} + F^{(2)} + F^{(3)})(p_e - p_e^2) \\ &= F^{(0)} + (F^{(1)} + F^{(2)} + F^{(3)} - 3F^{(0)})(p_e - p_e^2), \end{aligned} \tag{5.4}$$

with $F^{(0)}$, $F^{(1)}$, $F^{(2)}$ and $F^{(3)}$, the readout fidelities for 0 errors, an error on qubit 1, an error on qubit 2 and an error on qubit 3, respectively. For example, for assignment $\{|1\rangle_a, |1\rangle_a\}$ to stabilizer outcomes +1,+1 (no error), these readout fidelities are

$$\begin{aligned} F^{(0)} &= F_1^2, \\ F^{(1)} &= F^{(3)} = F_1 F_0, \\ F^{(2)} &= F_0^2, \end{aligned}$$

In a similar way, the fidelities for the other three assignments can be calculated.

Finally, if we assume that an erroneous ancilla readout decoheres the logical state, the dependence of the effective readout fidelity on p_e can be taken into account by setting:

$$A = A' F_{\mathrm{M}} \tag{5.5}$$

in Eqs. 5.1&5.2 for the process fidelity, with A' a constant.

Fitting of Figs. 3b, 3c and 5.12

In Fig. 5.3b, the ancilla readout is symmetrized by averaging over all four assignments, so that F_{M} equals the average readout fidelity 0.939(2) and is independent of p_e. We can therefore simply fit the data in Fig. 5.3b to Eq. 5.3, with A constant. We find $w = 0.81(3)$, corresponding to an average probability to successfully correct single-qubit errors of $\langle P_n \rangle = \frac{1}{3}(w + 2) = 0.94(1)$ [9]. We obtain $A = 0.557(2)$ and $O = 0.086(1)$. For the unencoded qubit, the encoded qubit without stabilizer measurements, and the encoded qubit without feedback, we find a linear function and $w \approx 0$ ($\langle P_n \rangle \approx 2/3$) as expected without error correction (exact values: $w = -0.06(3), -0.03(3)$ and $-0.07(3)$, $A = 0.882(4), 0.734(3)$

and 0.543(2), and $O = 0.019(3), 0.051(3)$ and $0.092(1)$, respectively for the three cases). In Fig. 5.12 the separate process fidelities for the different assignments are shown. Switching between assignments is done by adding or omitting a π-pulse before the ancilla readout.

In Fig. 5.3c, we assign the ancilla state $|1\rangle_a$ to the +1 outcome for all stabilizer measurements. This assignment is optimal because it associates the best readout fidelity with the most likely outcome: +1,+1 (no error, inset in Fig. 5.3b). We fit the data in Fig. 5.3c and Fig. 5.12 to Eq. 5.3, with A now error-dependent according to Eq. 5.5 and obtain $w = 0.8(1)$, corresponding to $\langle P_n \rangle = 0.93(3)$ ($A' = 0.666(8)$ and $O = 0.038(6)$). The values for w and $\langle P_n \rangle$ are in good agreement with the result of Fig. 5.3b, indicating that the treatment in Eqs. 5.4&5.5 is accurate.

Multiple rounds of error correction (incoherent errors), Fig. 5.4b

For multiple rounds of QEC with incoherent errors and with the total error with probability p_e equally distributed over n rounds, the error-probability per round is $p_n = \frac{1}{2}(1 - \sqrt[n]{1-2p_e})$, for $p_e < 0.5$. Ideally, the (average) state fidelity is then described by:

$$F = \frac{1}{2}[1 + (1 - 6p_n^2 + 4p_n^3)^n]. \tag{5.6}$$

As before we fit the data to a weighted sum of the equations for ideal error correction and for a linear error-dependence (no error correction). We use the optimal ancilla state assignment ($F_{\mathrm{M}}(p_e)$ from Eq. 5.4). For two rounds of error correction we obtain

$$F_2 = \frac{1}{2}w[1 + A'F_{\mathrm{M}}(1 - 6p_2^2 + 4p_2^3)^2] + \frac{1}{2}(1-w)[1 + A'F_{\mathrm{M}}(1-2p_e)], \tag{5.7}$$

giving $w = 0.66(4)$ and $A' = 0.850(9)$. For three rounds it becomes

$$F_3 = \frac{1}{2}w[1 + A'F_{\mathrm{M}}^2(1 - 6p_3^2 + 4p_3^3)^3] + \frac{1}{2}(1-w)[1 + A'F_{\mathrm{M}}^2(1-2p_e)], \tag{5.8}$$

giving $w = 0.71(2)$ and $A' = 0.810(5)$. Importantly, the data for multiple rounds cannot be accurately described by the expected shape for a single round of error correction (Eq. 5.3).

Naturally occurring decoherence (coherent errors), Fig. 5.4d

The experiments for the best unencoded qubit, the logical qubit with QEC and without QEC (majority vote only) are fitted to a general exponentially decaying function:

$$F = \frac{1}{2}(1 + Ae^{-(t/T)^n}). \tag{5.9}$$

Here, we obtain for the error-corrected logical qubit: $T = 24.2(2)$ ms and $n = 2.03(7)$, while for the best qubit we find: $T = 17.3(2)$ ms and $n = 2.09(7)$. For the encoded qubit with majority voting we obtain: $T = 13.7(1)$ ms and $n = 2.37(8)$.

To get a better understanding of quantum error correction and the projection of errors in the experiments with stabilizer measurements at half the free evolution time in Fig. 5.4d we turn to numerical Monte Carlo simulations, see Fig. 5.14 for details and results.

5.8.5 Error probabilities

The probability to detect no error ($P^{(0)}$) is the sum of the probability to have no error (no qubits flipped) or three errors (all qubits flipped) and is described by:

$$P^{(0)} = (1 - p_{\text{tot}}^{(1)})(1 - p_{\text{tot}}^{(2)})(1 - p_{\text{tot}}^{(3)}) + p_{\text{tot}}^{(1)} p_{\text{tot}}^{(2)} p_{\text{tot}}^{(3)}, \tag{5.10}$$

where $p_{\text{tot}}^{(i)}$ is the error probability for qubit i. The probability to detect an error on one of the three qubits ($P^{(i)}$) is the probability to have an error on qubit i, or an error on both of the other qubits, which for example for qubit 1 is described by:

$$P^{(1)} = p_{\text{tot}}^{(1)}(1 - p_{\text{tot}}^{(2)})(1 - p_{\text{tot}}^{(3)}) + (1 - p_{\text{tot}}^{(1)}) p_{\text{tot}}^{(2)} p_{\text{tot}}^{(3)}. \tag{5.11}$$

With finite input error probability $p_{\text{in}}^{(i)}$ for qubit i (errors already present in the initially prepared state), the total error as function of the applied error probability p_e, becomes:

$$p_{\text{tot}}^{(i)} = p_{\text{in}}^{(i)} + p_e - 2 p_{\text{in}}^{(i)} p_e \tag{5.12}$$

Finally we can take imperfect ancilla readout into account and obtain the probability to detect one of the error outcomes $P_{\text{D}}^{(i)}$ (i=0 for no detected error) as function of the applied error p_e:

$$P_{\text{D}}^{(0)} = P^{(0)} F^2 + (P^{(1)} + P^{(3)}) F(1 - F) + P^{(2)}(1 - F)^2 \tag{5.13}$$

$$P_{\text{D}}^{(1)} = P^{(1)} F^2 + (P^{(0)} + P^{(2)}) F(1 - F) + P^{(3)}(1 - F)^2 \tag{5.14}$$

$$P_{\text{D}}^{(2)} = P^{(2)} F^2 + (P^{(1)} + P^{(3)}) F(1 - F) + P^{(0)}(1 - F)^2 \tag{5.15}$$

$$P_{\text{D}}^{(3)} = P^{(3)} F^2 + (P^{(0)} + P^{(2)}) F(1 - F) + P^{(1)}(1 - F)^2 \tag{5.16}$$

The XX stabilizers in the encoded state tomography (Fig. 5.2) detect errors present in the encoded state, we obtain:

$$\begin{aligned}
P^{(0)} =& \langle \frac{1}{4}(1 + X_1, X_2, I_3)(1 + X_1, I_2, X_3) \rangle \\
=& \frac{1}{4}(1 + \langle X_1, X_2, I_3 \rangle + \langle I_1, X_2, X_3 \rangle + \langle X_1, I_2, X_3 \rangle) = 0.785(2) \\
P^{(1)} =& \langle \frac{1}{4}(1 - X_1, X_2, I_3)(1 - X_1, I_2, X_3) \rangle \\
=& \frac{1}{4}(1 - \langle X_1, X_2, I_3 \rangle + \langle I_1, X_2, X_3 \rangle - \langle X_1, I_2, X_3 \rangle) = 0.060(2) \\
P^{(2)} =& \langle \frac{1}{4}(1 - X_1, X_2, I_3)(1 + X_1, I_2, X_3) \rangle \\
=& \frac{1}{4}(1 - \langle X_1, X_2, I_3 \rangle - \langle I_1, X_2, X_3 \rangle + \langle X_1, I_2, X_3 \rangle) = 0.083(2) \\
P^{(3)} =& \langle \frac{1}{4}(1 + X_1, X_2, I_3)(1 - X_1, I_2, X_3) \rangle \\
=& \frac{1}{4}(1 + \langle X_1, X_2, I_3 \rangle - \langle I_1, X_2, X_3 \rangle - \langle X_1, I_2, X_3 \rangle) = 0.071(2)
\end{aligned}$$

which are uncorrected for qubit readout. These results can be translated to the input errors, as these outcomes refer to Eqs. 5.10&5.11 with no additional applied error p_e, giving $p_{\text{in}}^{(1)} = 0.064(2)$, $p_{\text{in}}^{(2)} = 0.091(2)$, $p_{\text{in}}^{(3)} = 0.077(2)$.

Using these values we estimate the expected total error detection probabilities $P_{\text{D}}^{(0)}$, $P_{\text{D}}^{(1)}$, $P_{\text{D}}^{(2)}$ and $P_{\text{D}}^{(3)}$ as function of applied error probability p_e according to Eqs. 5.10-5.16. The expected error-dependent QEC measurement outcomes are shown by the solid lines in the inset of Fig. 5.3b.

Error syndrome assignment

For the different error assignments, the asymmetry in the ancilla readout complicates the error detection curves: the QEC measurement fidelity is dependent on the error probability. If, for instance, both stabilizer measurements giving +1 are assigned to $\{|1\rangle_a, |1\rangle_a\}$, Eqs. 5.13-5.16 become:

$$P_{11}^{(0)} = P^{(0)}F_1^2 + (P^{(1)} + P^{(3)})F_1(1-F_0) + P^{(2)}(1-F_0)^2 \tag{5.17}$$

$$P_{11}^{(1)} = P^{(1)}F_1F_0 + P^{(0)}F_1(1-F_1) + P^{(2)}F_0(1-F_0) + P^{(3)}(1-F_1)(1-F_0) \tag{5.18}$$

$$P_{11}^{(2)} = P^{(2)}F_0^2 + (P^{(1)} + P^{(3)})F_0(1-F_1) + P^{(0)}(1-F_1)^2 \tag{5.19}$$

$$P_{11}^{(3)} = P^{(3)}F_1F_0 + P^{(0)}F_1(1-F_1) + P^{(2)}F_0(1-F_0) + P^{(2)}(1-F_1)(1-F_0) \tag{5.20}$$

All error detection curves for the four error assignments using similar equations are plotted in Fig. 5.12.

Multiple rounds of error correction, Fig. 5.4b

For multiple rounds we now calculate the average input error $p_{\text{in}}^{(\text{avg})}$ from the detection probability for no additional applied error ($p_e = 0$). We simplify Eq. 5.10 to

$$P^{(0)} = 1 - 3p_{\text{tot}}^{(\text{avg})} + 3(p_{\text{tot}}^{(\text{avg})})^2 \tag{5.21}$$

and use Eq. 5.17 to obtain the following average input error for round 1: $p_{\text{in}}^{(\text{avg})} = 0.092(1)$ and for round 2: $p_{\text{in}}^{(\text{avg})} = 0.086(1)$. The resulting curves according to Eq. 5.17 are shown in the inset of Fig. 5.4b.

5.8.6 Qubit readout calibration

To obtain best estimates for the actual states, the results are corrected for the fidelity of the gates used in the final readout (tomography). We distinguish between reading out single- two- and three-qubit expectation values.

For a single qubit i that is initialized and readout immediately, the measured expectation value $\langle Z_i \rangle$ is set by the initialization fidelity of the nitrogen spin ($F_N = 0.94(3)$) and by factors due to the initialization ($C_{\text{init},Qi}$) and readout (C_{Q_i}) of the qubit. Because the

initialization and readout consist of the same set of gates, we assume that $C_{\mathrm{init},Qi} = C_{Q_i}$ for this experiment and obtain:

$$\langle Z_i \rangle = F_N C_{Q_i}^2, \tag{5.22}$$

from which a readout correction factor $1/C_{Q_i}$ can be determined.

To calibrate the multi-qubit readouts we initialize the three qubits in separable states. For example, for state $|000\rangle$, the measured three-qubit expectation value $\langle Z_1 Z_2 Z_3 \rangle$ is set by the nitrogen initialization F_N, by factors $C_{\mathrm{init},Qi}$ due to the individual initialization fidelities of the three-qubits and by a factor C_{Q_1,Q_2,Q_3} due to the three-qubit readout:

$$\langle Z_1 Z_2 Z_3 \rangle = F_N C_{\mathrm{init},Q1} C_{\mathrm{init},Q2} C_{\mathrm{init},Q3} C_{Q_1,Q_2,Q_3} \rightarrow C_{Q_1,Q_2,Q_3} = \frac{\langle Z_1 Z_2 Z_3 \rangle}{F_N C_{\mathrm{init},Q1} C_{\mathrm{init},Q2} C_{\mathrm{init},Q3}}. \tag{5.23}$$

This equation assumes that the initialization errors, other than those due to the nitrogen initialization, are uncorrelated. The initialization fidelities are obtained using the single-qubit expectation values and single qubit C_{Q_i} for the corresponding qubit, i.e. for qubit 1:

$$\begin{aligned} \langle Z_1 I_2 I_3 \rangle &= F_N C_{\mathrm{init},Q1} C_{Q_1} \\ &\rightarrow C_{\mathrm{init},Q1} = \frac{\langle Z_1 I_2 I_3 \rangle}{F_N C_{Q_1}} \end{aligned} \tag{5.24}$$

with C_{Q_1} from Eq. 5.22. In a similar way, the two-qubit readout is calibrated using two-qubit expectation values of two- and three-qubit states. We obtain the following values:

$C_{Q_1} = 0.95(1)$	$C_{Q_1 Q_2} = 0.94(2)$	$C_{Q_1 Q_2 Q_3} = 0.92(5)$
$C_{Q_2} = 0.94(1)$	$C_{Q_1 Q_3} = 0.88(4)$	
$C_{Q_3} = 0.95(1)$	$C_{Q_2 Q_3} = 0.90(2)$	

which are used to calibrate the final readouts for tomography. Note that the uncertainty in the readout calibration potentially creates a small systematic error (a rescaling of all y-axes). For this reason we also provide all raw (uncalibrated) data for the error correction in Fig. 5.15.

Although our data do not yield a rigorous value of the two-qubit gate fidelity, the qubit readout fidelities derived here, $F = (1 + C_{Q_i})/2 \approx 0.97$ give an indication of the two-qubit gate fidelity as readout consists of two single qubit gates and one two-qubit gate.

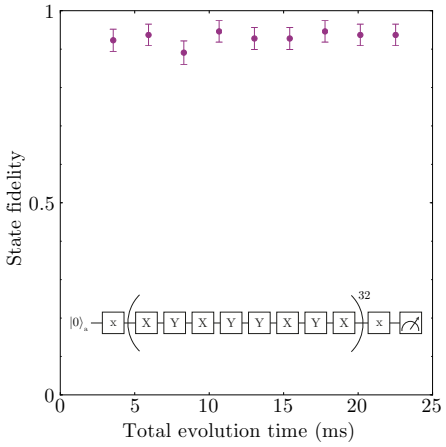


Figure 5.5 —Coherence of the NV electron spin by dynamical decoupling with 256 pulses. The spin is decoupled from the nuclear spin bath by applying a sequence of 256 π-pulses with alternating phases. The time between the pulses is chosen to be a multiple of the Larmor period of the ^{13}C spins. This result shows no significant decay on the relevant timescale of our experiments.

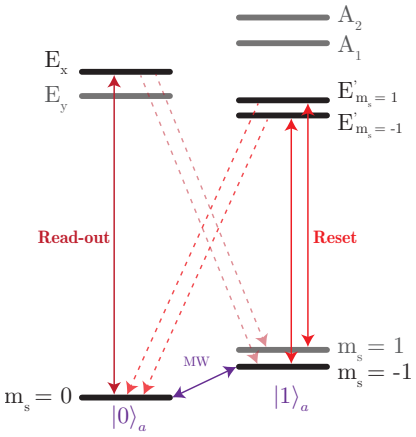


Figure 5.6 —Optical readout and initialization of the ancilla NV electron spin. The electron spin is initialized and read out by spin-selective resonant excitation[18]. To initialize or reset the electron spin state we apply a laser pulse that excites only the $m_s = \pm 1 \leftrightarrow E'_{m_s=\pm 1}$ transitions (Reset). Due to spin mixing in the excited state this prepares the electron spin in the $m_s = 0$ state (fidelity > 0.98)[18]. To measure the spin state we apply a laser pulse resonant with the $m_s = 0 \leftrightarrow E_x$ transition (Read-out). Ideally, this results in the detection of 1 or more photons for the $m_s = 0$ state, and no detected photons for $m_s = \pm 1$. The resulting readout fidelities are asymmetric: $F_0 = 0.890(4)$ for $m_s = 0$ (limited by the detection efficiency and number of cycles before a spin flip) and $F_1 = 0.988(2)$ for $m_s = \pm 1$ (limited by background counts and unwanted excitations). Because uncontrolled spin flips in the excited state decohere nearby nuclear spins, we minimize the number of unnecessary optical excitations by using a weak readout pulse with a maximum duration of 114 μs (~ 100 excitations) and by switching off the laser within 2 μs (~ 2 excitations) once a photon is detected[24]. The resulting measurement is non-destructive: the probability that the spin prepared in $m_s = 0$ is still in that state after a measurement with outcome $m_s = 0$ is 0.992. In contrast, without dynamically stopping the laser the spin would be pumped almost completely to $m_s = \pm 1$. For the final readout at the end of the experiment, which is allowed to be destructive, we use a stronger readout pulse of maximum duration 35 μs.

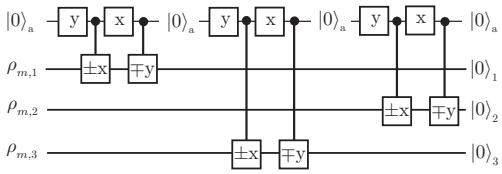


Figure 5.7 —Qubit initialization. All qubits naturally start in fully mixed states ρ_m. The ancilla is initialized in $|0\rangle_a$ and a reduced SWAP operation between the ancilla and the qubit is performed, deterministically initializing the qubit in $|0\rangle$. The ancilla is then reinitialized by a 300 μs laser pulse (Reset) and the process is repeated to initialize the other qubits. Note that the signs of the controlled $\pm y$-rotations are corrected with respect to the publication.

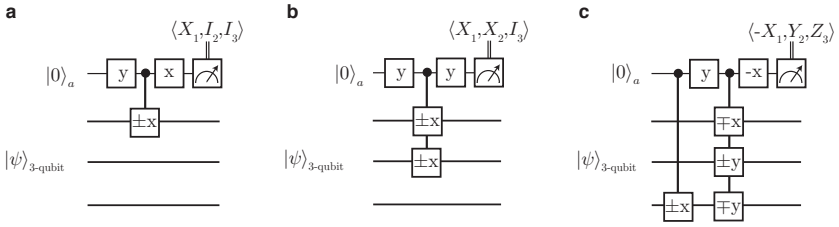


Figure 5.8 —Tomography sequences for three-qubit states. Examples of three-qubit expectation values that are measured by mapping the required correlation on the ancilla before reading it out. **a,** $\langle X_1, I_2, I_3\rangle$, **b,** $\langle X_1, X_2, I_3\rangle$, **c,** $\langle -X_1, Y_2, Z_3\rangle$. Note that the phase of the last $\pi/2$-pulse on the ancilla depends on the number of qubits read out (i.e. the number of operators that are not I). Note that the sign of the controlled $\pm y$-rotation in **c** is corrected with respect to the publication. The examples given here for the measurement of one- two- and three-qubit expectation values can be translated to any of the 63 measurements in the full three-qubit state tomography.

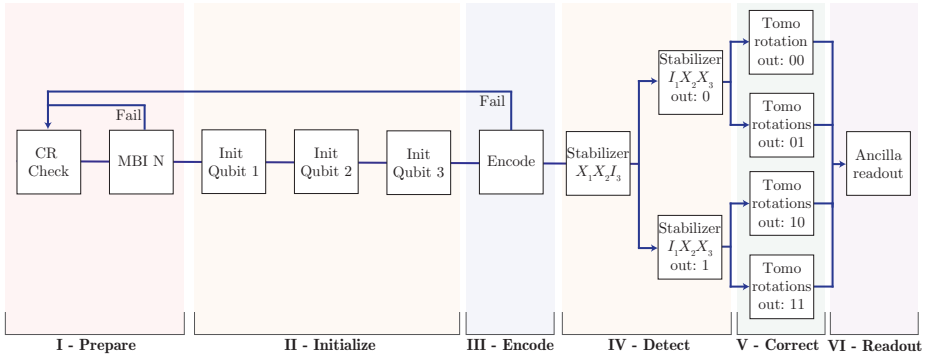


Figure 5.9 —Experimental sequence and logic for the QEC experiments. Example for a single round of quantum error correction by stabilizer measurements (as in Fig. 5.3). The order of the sequence is controlled in real-time by an ADwin microprocessor. **I** - The NV centre is prepared in its negative charge state and on resonance with the readout and reset lasers (Fig. 5.6) by turning on both lasers, counting the fluorescence photons and requiring a threshold to be passed ("CR Check"). The ^{14}N nuclear spin is initialized by measuring it and continuing only for outcome $m_I = -1$ ("MBI N", success probability 0.073(7)). **II** - The qubits are sequentially deterministically initialized following Fig. 5.7. **III** - The encoding of the logic state is a probabilistic process (success probability 0.41(1)), as shown in Fig. 5.2a. When the wrong outcome is obtained the preparation of the experiment starts over. **IV** - Errors are detected by two stabilizer measurements. Depending on the outcome (-1 or $+1$) of each measurement, the next sequence to execute is communicated to the waveform generator in real time. **V** - Depending on which of the 4 outcomes is obtained, a set of gates is performed to correct errors and to map the desired expectation value onto the ancilla (Fig. 5.8). **VI** - Finally the ancilla is read out. Each outcome is taken into account without post processing or post selection. Note that for the experiment with three rounds of error correction (two rounds of stabilizer measurements QEC, Fig. 5.4b), the sequence branches in 16 paths instead.

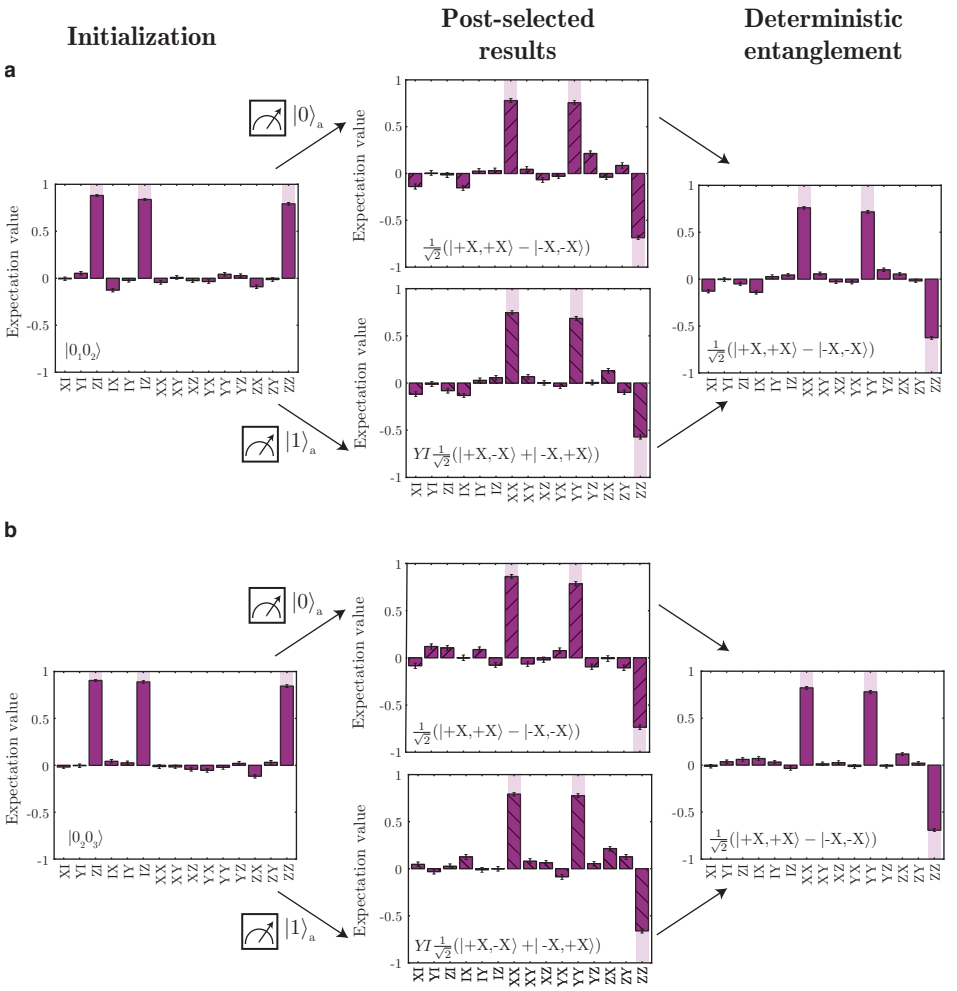


Figure 5.10 —Deterministic entanglement by stabilizer measurements including post-selected results. a, For qubits 1 and 2. **b,** For qubits 2 and 3. First the qubits are initialized following Fig. 5.7 in $|00\rangle$ with fidelity 0.878(6) for (a) and 0.910(6) for (b) (left column). Then a XX measurement is performed (Fig. 5.1d). Depending on the measurement outcome feedback is applied, so that independent of the outcome the same two-qubit state is obtained, as can be seen by post-selecting on the two outcomes (middle column). The full result is a deterministically entangled state (right column). The fidelity with the desired two-qubit entangled state is 0.776(7) in (a) and 0.824(7) in (b).

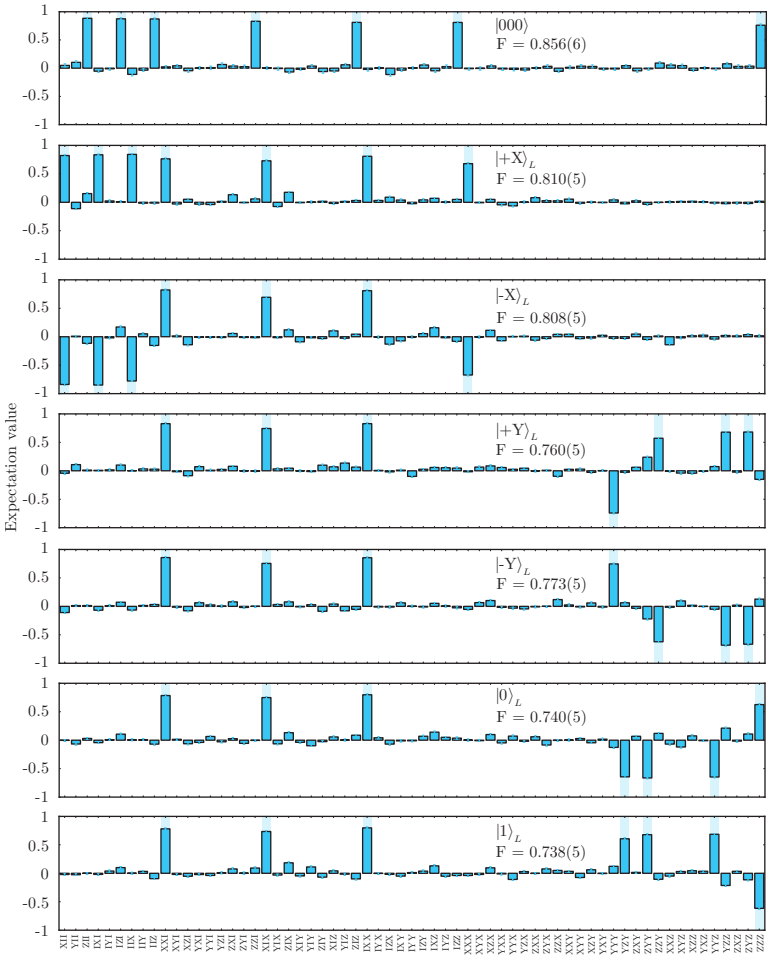


Figure 5.11 —Three-qubit state tomography for $|000\rangle$ and the six logical states. The three qubits are initialized as in Fig. 5.7 and encoded following Fig. 5.2a. The fidelities F shown are the three-qubit state fidelities and the shaded bars indicate the ideal states. Ideally, the 6 encoded states are all eigenstates of the XX stabilizers with eigenvalues $+1$, in agreement with the high values for $\langle X_1, X_2, I_3\rangle$, $\langle X_1, I_2, X_3\rangle$ and $\langle I_1, X_2, X_3\rangle$ for all states and an average fidelity with this code subspace of 0.839(3). The logical qubit is encoded as $\alpha\,|0\rangle_L + \beta\,|1\rangle_L$, with $|0\rangle_L = \frac{1}{\sqrt{2}}(|+X,+X,+X\rangle + |-X,-X,-X\rangle)$ and $|1\rangle_L = \frac{1}{\sqrt{2}}(|+X,+X,+X\rangle - |-X,-X,-X\rangle)$. The logical state expectation values are given by: $\langle X\rangle_L = \langle X_1, I_2, I_3\rangle$, $\langle Y\rangle_L = \langle Y_1, Z_2, Z_3\rangle$, $\langle Z\rangle_L = \langle Z_1, Z_2, Z_3\rangle$ or cyclic permutations. The logical qubit fidelities for the states are $|+X\rangle_L : 0.916(6)$, $|-X\rangle_L : 0.911(6)$, $|+Y\rangle_L : 0.822(7)$, $|-Y\rangle_L : 0.828(7)$, $|0\rangle_L : 0.813(9)$ and $|1\rangle_L : 0.808(9)$.

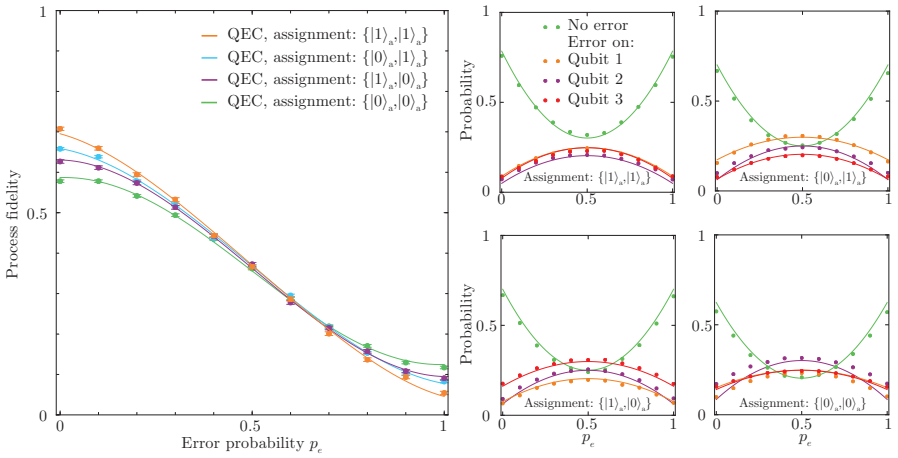


Figure 5.12 —Process fidelity and error syndrome probabilities for different ancilla assignments. Left: comparison of the process fidelities for the quantum error correction experiment in Fig. 5.3 for all four possible assignments of the ancilla states to the +1,+1 outcome of the stabilizer measurements. In Fig. 5.3b we average over these four curves. In Fig. 5.3c the optimal result is used (assignment $\{|1\rangle_a, |1\rangle_a\}$). Solid lines are fits to Eq. 5.3 taking into account Eq. 5.4 and yield: $w = 0.8(1)$, $w = 0.71(7)$, $w = 0.95(7)$ and $w = 0.84(9)$ for the four assignments. Right: the probabilities for the error syndromes for each of the four ancilla state assignments. Solid lines are expected curves similar to Eqs. 5.17-5.20, based on the estimated initial errors in the encoded states: $p_{\text{in}}^{(1)} = 0.091(2)$, $p_{\text{in}}^{(2)} = 0.064(2)$, $p_{\text{in}}^{(3)} = 0.077(2)$ obtained from Fig. 5.11. The theoretical probabilities are in good agreement with the experimental values (no free parameters). The probabilities are the normalized occurrences in 84000 samples for the assignments $\{|0\rangle_a, |0\rangle_a\}$ and $\{|0\rangle_a, |1\rangle_a\}$ and in 28000 samples for the assignments $\{|1\rangle_a, |1\rangle_a\}$ and $\{|1\rangle_a, |0\rangle_a\}$.

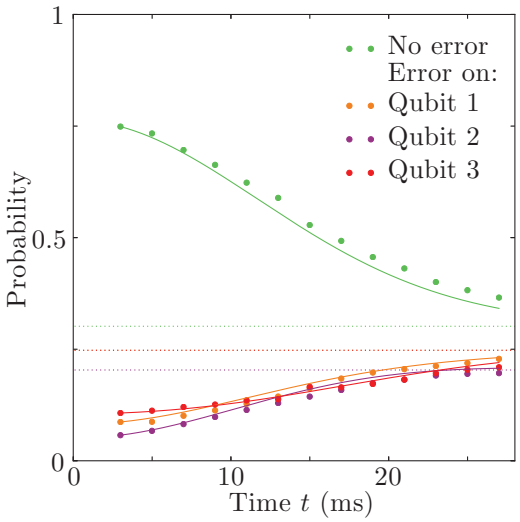


Figure 5.13 —Error syndrome probabilities for naturally occurring errors. Corresponding to Fig. 5.4d. Solid lines are theoretical predictions from the unique coherence times T_2^* of the individual qubits and the initial error (p_{in}) determined from this data. As the stabilizer measurements are performed halfway the waiting time, the error probability for each qubit is: $p_e(\frac{t}{2}) = \frac{1}{2}(1 - \text{Exp}[-(\frac{t}{2T_2^*})^2])$. Using Eqs. 5.17-5.20 and the measured error outcome probabilities at the first datapoint ($t = 2.99$ ms), we estimate the input errors at $t = 0$ to be $p_{\text{in}}^{(1)} = 0.049(2)$, $p_{\text{in}}^{(2)} = 0.0804(4)$ and $p_{\text{in}}^{(3)} = 0.110(2)$. Dashed lines show the expected probabilities for complete dephasing. The probabilities are based on the normalized occurrences in 12000 samples.

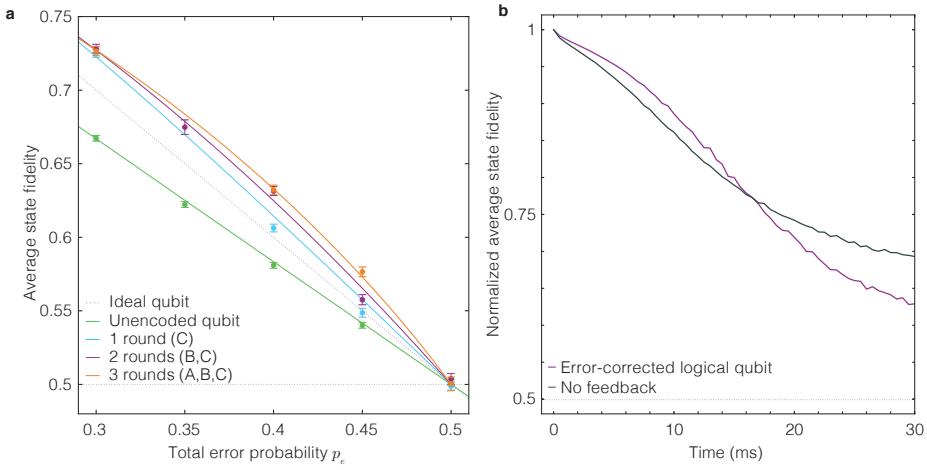


Figure 5.14 —Zoom of data of Fig. 5.4b (a) and numerical simulation of Fig. 5.4d (b). a, A zoom-in of the area of the data in Fig. 5.4b in which additional rounds of error-correction are advantageous. **b,** Numerical Monte-Carlo simulations for the error correction experiment of Fig. 5.4d. **Sequence.** The initial state is $|X\rangle_L$. Each qubit then coherently evolves with a constant detuning randomly drawn from a Gaussian probability distribution with $\sigma = \sqrt{2}/T_2^*$ for that qubit. Halfway the evolution time the stabilizer measurements instantaneously project the quantum state, taking into account the asymmetric fidelity of the ancilla readout and the error-dependent readout fidelity (Eqs. 5.3-5.5). After letting the state evolve for the second period with the same detuning, detected errors are corrected (this final step is omitted for "No feedback"). **Longitudinal relaxation.** The qualitative behavior of the simulations is dominated by the dephasing times T_2^*. We additionally take into account the measured longitudinal relaxation of each qubit, which approximately decays with $e^{-(t/T_1)^{0.5}}$ for ancilla state $|0\rangle_a$ (See Tab. 5.1), and of the ancilla (time-constant 300 ms, due to MW and laser background). The longitudinal decay results in a small quantitative correction, but does not alter the qualitative behavior observed. **Results & discussion.** The simulation results qualitatively match all the main features of the observed dephasing curves (Fig. 4d). For short times, the stabilizer measurements suppress errors by stopping small errors from building up coherently and error correction further reduces the remaining errors. For long times, the stabilizer measurements halfway the sequence preferentially suppress coherent evolutions that would result in an error at the end of the sequence. As a result the fidelity at long times exceeds 0.5 and decays only slowly. Moreover, for long times, applying error correction becomes detrimental: at the moment the stabilizer measurements are applied the state is essentially random and no useful information about errors is extracted so that applied corrections further dephase the final state. A complete quantitative comparison would require detailed modeling of the full evolution of the 4-qubit system during the gates, initialization, stabilizer measurements, and readout sequences as well as of the longitudinal decay at short times.

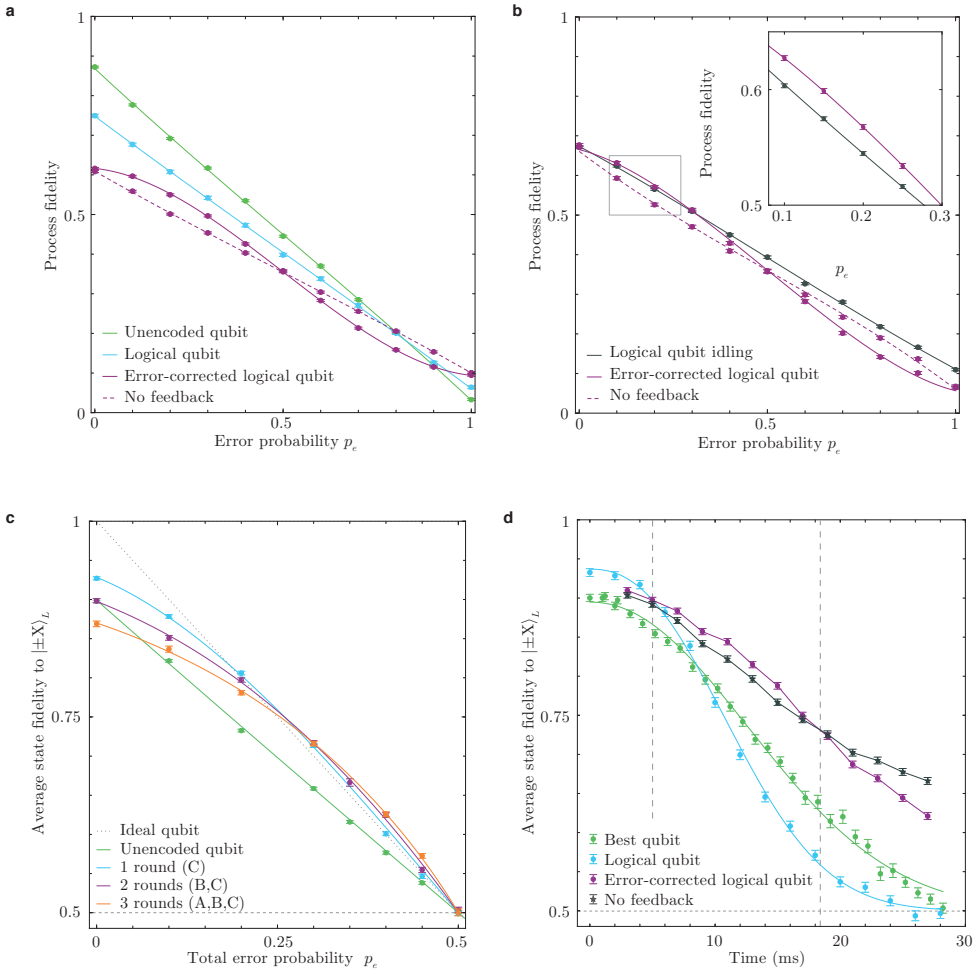


Figure 5.15 —Data of Fig. 5.3b (a) 5.3c (b), 5.4b (c) and 5.4d (d), without correction for the final readout gates. a, b, The fitted value for w is identical as in the main text (curve shapes are not influenced by the readout calibration). **c,** Corresponding fit values for the unencoded qubit: $w = -0.02(2)$, for 1 round: $w = 0.56(6)$, for 2 rounds $w = 0.64(4)$ and for three rounds $w = 0.70(2)$. **d,** The logical qubit follows Eq. 5.9 with $T = 13.7(1)$ ms and $n = 2.35(8)$.

	Qubit 1	Qubit 2	Qubit 3
$A_\parallel$ (kHz)	2π·20.6	2π·-36.4	2π·24.4
$A_\perp$ (kHz)	2π·43	2π·25	2π·26
ω_0 (kHz)	2π·431.874(3)	2π·431.994(3)	2π·431.934(3)
ω_1 (kHz)	2π·413.430(3)	2π·469.025(3)	2π·408.303(3)
τ (μs)	13.616	4.996	11.312
N	32	34	48
gate time (μs)	980	400	1086
T_2^*, $m_s = 0$ (ms)	12.0(9)	9.1(6)	18.2(9)
T_2^*, $m_s = -1$ (ms)	12.8(6)	9.8(4)	21(1)
T_1, $m_s = 0$ (ms)	110(10)	100(10)	330(30)

Table 5.1 —Qubit and gate parameters. $A_\parallel$ and $A_\perp$ are the estimated hyperfine interaction components parallel and perpendicular to the applied magnetic field. ω_0 and ω_1 are the nuclear precession frequencies for $m_s = 0$ ($|0\rangle_a$) and $m_s = -1$ ($|1\rangle_a$). τ is half the inter pulse delay, N the number of pulses and $gate\ time$ the total duration for the conditional $\pm x$-gates. These values vary slightly over the experiment as they are calibrated every ~ 36 hours. T_2^* is the (natural) dephasing time and T_1 the longitudinal relaxation time.

	Fig. 5.3b (logical qubit with QEC)	Fig. 5.4b (3 rounds)
Two-qubit gates	19	20
Ancilla refocusing pulses	698	808
Ancilla read-out and reset	7	9

Table 5.2 —Experimental complexity. Number of operations in the entire sequence, starting from the initialization of the nuclear spins as qubits. All qubit (^{13}C) gates are composed of ancilla (NV electron spin) refocusing pulses and the ancilla is read-out and reset multiple times. We give values for two examples: a single round of QEC with measurement of $\langle Z_1 Z_2 Z_3 \rangle$ (Fig. 5.3b) and three rounds of QEC with measurement of $\langle X_1 X_2 X_3 \rangle$ (Fig. 5.4b).

5.9 Bibliography

[1] B. M. Terhal. Quantum error correction for quantum memories. *Reviews of Modern Physics* **87**, 307 (2015).

[2] S. B. Bravyi and A. Y. Kitaev. Quantum codes on a lattice with boundary. *arXiv:quant-ph/9811052* (1998).

[3] R. Raussendorf and J. Harrington. Fault-Tolerant Quantum Computation with High Threshold in Two Dimensions. *Physical Review Letters* **98**, 190504 (2007).

[4] D. Nigg *et al.* Quantum computations on a topologically encoded qubit. *Science* **345**, 302 (2014).

[5] E. Knill, R. Laflamme, R. Martinez and C. Negrevergne. Benchmarking Quantum Computers: The Five-Qubit Error Correcting Code. *Physical Review Letters* **86**, 5811 (2001).

[6] J. Chiaverini *et al.* Realization of quantum error correction. *Nature* **432**, 602 (2004).

[7] P. Schindler *et al.* Experimental Repetitive Quantum Error Correction. *Science* **332**, 1059 (2011).

[8] M. D. Reed *et al.* Realization of three-qubit quantum error correction with superconducting circuits. *Nature* **482**, 382 (2012).

[9] T. H. Taminiau, J. Cramer, T. v. d. Sar, V. V. Dobrovitski and R. Hanson. Universal control and error correction in multi-qubit spin registers in diamond. *Nature Nanotechnology* **9**, 171 (2014).

[10] G. Waldherr *et al.* Quantum error correction in a solid-state hybrid spin register. *Nature* **506**, 204 (2014).

[11] B. P. Lanyon *et al.* Measurement-Based Quantum Computation with Trapped Ions. *Physical Review Letters* **111**, 210501 (2013).

[12] A. D. Córcoles *et al.* Demonstration of a quantum error detection code using a square lattice of four superconducting qubits. *Nature Communications* **6**, 6979 (2015).

[13] D. Ristè *et al.* Detecting bit-flip errors in a logical qubit using stabilizer measurements. *Nature Communications* **6**, 6983 (2015).

[14] J. Kelly *et al.* State preservation by repetitive error detection in a superconducting quantum circuit. *Nature* **519**, 66 (2015).

[15] L. Sun *et al.* Tracking photon jumps with repeated quantum non-demolition parity measurements. *Nature* **511**, 444 (2014).

[16] J. P. Hadden *et al.* Strongly enhanced photon collection from diamond defect centers under microfabricated integrated solid immersion lenses. *Applied Physics Letters* **97**, 241901 (2010).

[17] G. D. Fuchs, V. V. Dobrovitski, D. M. Toyli, F. J. Heremans and D. D. Awschalom. Gigahertz Dynamics of a Strongly Driven Single Quantum Spin. *Science* **326**, 1520 (2009).

[18] L. Robledo *et al.* High-fidelity projective read-out of a solid-state spin quantum register. *Nature* **477**, 574 (2011).

[19] N. Bar-Gill, L. M. Pham, A. Jarmola, D. Budker and R. L. Walsworth. Solid-state electronic spin coherence time approaching one second. *Nature Communications* **4**, 1743 (2013).

[20] G.-Q. Liu, H. C. Po, J. Du, R.-B. Liu and X.-Y. Pan. Noise-resilient quantum evolution steered by dynamical decoupling. *Nature Communications* **4**, 2254 (2013).

[21] L. Jiang *et al.* Coherence of an Optically Illuminated Single Nuclear Spin Qubit. *Physical Review Letters* **100**, 073001 (2008).

[22] W. Pfaff *et al.* Demonstration of entanglement-by-measurement of solid-state qubits. *Nature Physics* **9**, 29 (2013).

[23] G. Wolfowicz *et al.* 29 Si nuclear spins as a resource for donor spin qubits in silicon. *New Journal of Physics* **18**, 023021 (2016).

[24] M. S. Blok *et al.* Manipulating a qubit through the backaction of sequential partial measurements and real-time feedback. *Nature Physics* **10**, 189 (2014).

[25] J. T. Barreiro *et al.* An open-system quantum simulator with trapped ions. *Nature* **470**, 486 (2011).

[26] D. Ristè *et al.* Deterministic entanglement of superconducting qubits by parity measurement and feedback. *Nature* **502**, 350 (2013).

[27] P. London *et al.* Detecting and Polarizing Nuclear Spins with Double Resonance on a Single Electron Spin. *Physical Review Letters* **111**, 067601 (2013).

[28] M. D. Shulman *et al.* Suppressing qubit dephasing using real-time Hamiltonian estimation. *Nature Communications* **5**, 5156 (2014).

[29] P. C. Maurer *et al.* Room-Temperature Quantum Bit Memory Exceeding One Second. *Science* **336**, 1283 (2012).

[30] G. Balasubramanian *et al.* Ultralong spin coherence time in isotopically engineered diamond. *Nature Materials* **8**, 383 (2009).

[31] K. Saeedi *et al.* Room-Temperature Quantum Bit Storage Exceeding 39 Minutes Using Ionized Donors in Silicon-28. *Science* **342**, 830 (2013).

[32] J. T. Muhonen *et al.* Storing quantum information for 30 seconds in a nanoelectronic device. *Nature Nanotechnology* **9**, 986 (2014).

[33] L. Li *et al.* Coherent spin control of a nanocavity-enhanced qubit in diamond. *Nature Communications* **6**, 6173 (2015).

[34] F. Dolde *et al.* High-fidelity spin entanglement using optimal control. *Nature Communications* **5**, 3371 (2014).

[35] W. Pfaff *et al.* Unconditional quantum teleportation between distant solid-state quantum bits. *Science* **345**, 532 (2014).

[36] B. Hensen *et al.* Loophole-free Bell inequality violation using electron spins separated by 1.3 kilometres. *Nature* **526**, 682 (2015).

[37] N. H. Nickerson, Y. Li and S. C. Benjamin. Topological quantum computing with a very noisy network and local error rates approaching one percent. *Nature Communications* **4**, 1756 (2013).

[38] T. K. Yeung, D. L. Sage, L. M. Pham, P. L. Stanwix and R. L. Walsworth. Anti-reflection coating for nitrogen-vacancy optical measurements in diamond. *Applied Physics Letters* **100**, 251111 (2012).

Chapter 6

Towards general QEC experiments with spins in diamond

J. Cramer

In the preceding chapters I presented the experimental implementation of basic QEC protocols. However, these protocols could only correct for specific errors. In this chapter I will discuss the protection of quantum information against general single-qubit errors and propose the experimental implementation of fault-tolerant protocols based on the techniques developed in this thesis for diamond spins. I will consider the protection of two logical qubits by quantum error detection (Sec. 6.2) and the active protection of a single logical qubit by five-qubit quantum error correction, the smallest general QEC code (Sec. 6.3).

6.1 Introduction

Realistic quantum information processing demands the correction of general errors on arbitrary quantum states. Quantum error correction (QEC) protects quantum information by redundant encoding in multiple data qubits and subsequent correlation measurements to detect errors that can be actively corrected[1–4]. While the detection and correction of specific errors in quantum systems has been explored experimentally[5–16], there have not been experimental implementations that detect and correct quantum states against general errors (X, Y and Z errors) on continuously encoded qubits.

Spins in diamond have shown to be a promising platform for the implementation of QEC, employing nuclear spins surrounding the NV electron spin (Chaps. 4,5). The long coherence times of these nuclear spins, combined with high-fidelity non-destructive single-shot readout of the NV electron spin state, provide a hybrid quantum system allowing for QEC by ancilla-based correlation measurements and real-time feedback. The NV centre coupled to ^{13}C spins provides an extendable quantum register allowing for the implementation of general QEC codes[17,18].

In this chapter I propose the implementation of general quantum error detection and correction codes based on the control of nuclear ^{13}C spins in diamond via the NV centre electron spin. For quantum error detection, two logical qubits are encoded in four data qubits, detecting single-qubit errors by stabilizer measurements. The smallest code for general quantum error correction, which detects and corrects single-qubit errors, requires five data qubits for the encoding and four correlation measurements to detect errors that can subsequently be corrected.

One important task in the experimental implementation of such codes in our system is the compiling of the protocol into the natural two-qubit gates between the NV electron spin and a ^{13}C nuclear spin. The resulting deterministic basis rotations transform the Pauli frame of the protocol (Ch. 2), which will be worked out in this chapter.

6.2 Quantum error detection

Besides active detection and correction of quantum errors, general quantum computations can be achieved by post-selected error detection protocols[19]. Such error detection protocols can be relatively fast with respect to quantum error correction protocols and generally require less qubits. Due to the post-selection however, the final resource requirements can be larger than for quantum error correction in which post-selection is not needed[19,20].

The minimal code detecting general errors in arbitrary quantum information is the four-qubit code[21]. A combination of two stabilizer measurements (e.g. $ZZZZ$ and $XXXX$) detects general errors on single qubits in the encoding. No information is obtained regarding the erroneous qubit, which makes it impossible to deterministically correct the state. Extending the nuclear spin register from three (Ch. 5) to four weakly coupled ^{13}C spins in a single experiment allows for the implementation of four-qubit quantum error detection.

6.2.1 Logical qubit

The four-qubit quantum error detection code protects two logical qubits by encoding in four data qubits. The code space can be defined by the stabilizers $XXXX$ and $ZZZZ$. This allows for two qubits of freedom, two logical operators therefore define the four codewords $|00\rangle_L, |01\rangle_L, |10\rangle_L$ and $|11\rangle_L$. The logical operators for the two logical qubits can for example be defined by:

$$X_{L1} = X_1X_2, \qquad Z_{L1} = Z_1Z_3, \qquad X_{L2} = X_1X_3, \qquad Z_{L2} = Z_1Z_2.$$

Initialization in a logical state in the code space can be performed by a chosen method, such as:

- Measurement of two stabilizer operators corresponding to the code space and two logical operators corresponding to the intended logical state projects the data qubits to the code space and the logical state. For example, subsequent measurements of the operators $XXXX$, $ZZZZ$, Z_1Z_2 and Z_1Z_3 on a four-qubit (mixed) state initialized the qubits in the logical state $|00\rangle_L$.
- Initialization of the data qubits can reduce the number of measurements. For example, an input state of $|0000\rangle$ only requires measurement of the operator $XXXX$ to initialize the logical qubit in $|00\rangle_L$ (Fig. 6.1a).
- Initialization in a logical two-qubit state by one of the methods above followed by an operation via the ancilla qubit, as employed in Ch. 5. For example, a controlled

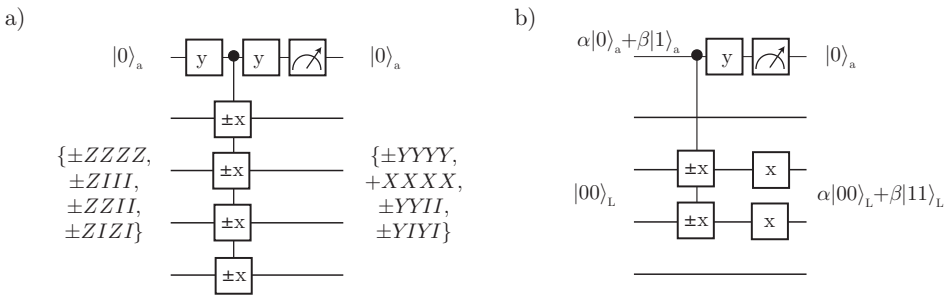


Figure 6.1 — Logical state initialization for four-qubit encoding. a, The four nuclear spins are encoded in a two-qubit logical codeword by initializing in an eigenstate of $ZZZZ$ and $ZIII$ and two logical operators, for example $ZZII$ and $ZIZI$. A measurement of $XXXX$ detects the overlap with the code space, intializing qubits in the logical state. **b,** An example of initialization in state $\alpha|00\rangle_L + \beta|11\rangle_L$ via the ancilla qubit is given. After the circuit shown in **a**, a state on the logical qubit is initialized via the ancilla qubit. To compensate for the extra $\pi/2$-rotations in the electron-controlled operations on the ^{13}C, a $\pi/2$ gate can be applied on each physical qubit. In practice, however, these operations are taken into account by Pauli frame updates in subsequent operations.

$X_{L_1}X_{L_2}$ operation on the logical state $|00\rangle_L$, for the ancilla in $\alpha|0\rangle + \beta|1\rangle$, initializes the system in $\alpha|00\rangle_L + \beta|11\rangle_L$ upon projection of the ancilla qubit by measurement (Fig. 6.1b).

The code space is determined by the measurement outcomes of the stabilizer measurements (error syndrome), which can simultaneously mark a first round of error detection.

6.2.2 Error detection

The four-qubit quantum error detection code detects general errors by stabilizer measurements via an ancilla qubit. The logical code space is stabilized by the operators $XXXX$ and $ZZZZ$. By projecting the stabilizer operators in the initialization, the code space is defined. To detect errors, these stabilizer operators are continuously measured. When a single error on a data qubit occurs, a measurement of the noncommuting stabilizer operator switches sign[22] ('clicks'); the measurement returns the opposite eigenvalue indicating an error. The combination of the two stabilizer measurement outcomes returns the 'error syndrome', to identify if no error or an error around the $x-$, $y-$ or $z-$axis on one of the four qubits occurred.

Due to the extra basis rotations in the physical gates of our system, the measurements transform the Pauli frame (Ch. 2) and thus the stabilizer operators defining the code space. A measurement of the $XXXX$-stabilizer transforms the stabilizers $ZZZZ \leftrightarrow YYYY$, while a measurement of the $YYYY$-stabilizer transforms the stabilizers $ZZZZ \leftrightarrow XXXX$. Keeping track of these transformations will result in the correct error detection as well as the updates of Pauli frame of the logical qubit. The symmetric concatenation of the four-qubit stabilizer

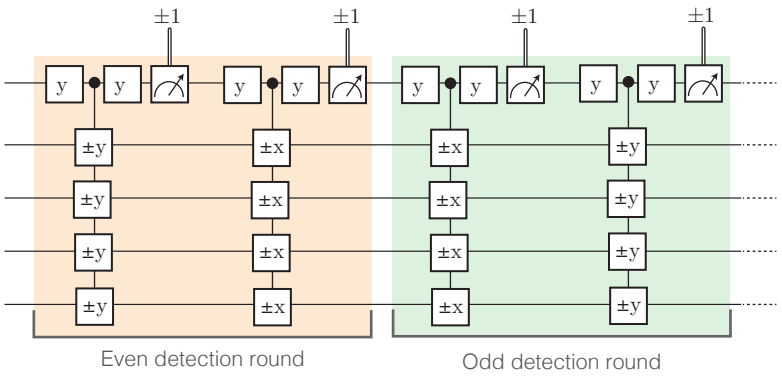


Figure 6.2 — Repeated sequence of stabilizer measurements for four-qubit error detection. Repeating the stabilizer measurements for error detection in the proposed way returns the initial states after four succesful stabilizer measurements (two rounds of error detection). Transformations can be tracked and taken into account in updates of the Pauli frame of the logical quantum state.

measurements as shown in Fig. 6.2, transforms the stabilizer operators such that after two effective rounds of error detection (four stabilizers), the initial Pauli frame is obtained.

To characterize the experimental implementation of the protocol state fidelity and state tomography can be measured. Full state tomography of the final four-qubit state requires a set of 255 measurements to obtain all expectation values in the Pauli-set $\{\langle IIII\rangle, ..., \langle ZZZZ\rangle\}$. However, the logical two-qubit state tomography requires measurement of only fifteen operators $\{\langle I_{L1}I_{L2}\rangle, ..., \langle Z_{L1}Z_{L2}\rangle\}$. The logical state-fidelity is obtained by measurement of three logical operators defining the intended logical state or the fifteen operators defining the corresponding four-qubit state.

6.3 Five-qubit quantum error correction

The four-qubit error detection code as discussed above detects single-qubit errors around all axes (X, Y and Z errors), but does not identify the data qubit that got the error. According to the Hamming bound[23] a minimum number of five qubits is required to detect and correct for single-qubit errors around all axes. Here, I will discuss the implementation of such a five-qubit QEC protocol as first proposed by Laflamme *et al.*[24], extending the spin register and methods used in Ch. 4.

6.3.1 Logical qubit

The five-qubit quantum error correction code detects and corrects general single-qubit errors by encoding a single logical qubit of information in five data qubits. A combination of four four-qubit stabilizer measurements detects the error syndrome, leaving one degree of freedom for the encoding of the logical qubit state. The logical code space can be defined by four stabilizer operators[22,25]:

$$K^a = XYYXI, \qquad K^b = XZIZX, \qquad K^c = YIYZZ, \qquad K^d = ZXXZI. \tag{6.1}$$

The logical-qubit operators can be defined by

$$X_L = XXXXX, \qquad Z_L = ZZZZZ. \tag{6.2}$$

Initialization of the data qubits in a logical single-qubit state, can be performed dependent on experimental preference and intended encoded state, similar to the four-qubit logical state (Sec. 6.2). We focus on three methods to initialize the logical qubit state. All methods require the measurement of the four stabilizer operators, to project into the logical code space.

- To initialize in an eigenstate of a logical Clifford operator, one can initialize the five data qubits individually in a eigenstate of the single-qubit operators X, Y or Z, e.g. $|00000\rangle$, followed by projection of the four stabilizer operators (Eq. 6.1).
- Initialization in an eigenstate of a logical operator (Eq. 6.2) can also be performed by projection of this operator, followed by projection of the four stabilizer operators (Eq. 6.1). An example of such initialization along the x-axis is given in Fig. 6.3a, where the operator X_L is projected, taking into account the basis rotations of our experimental two-qubit gates.

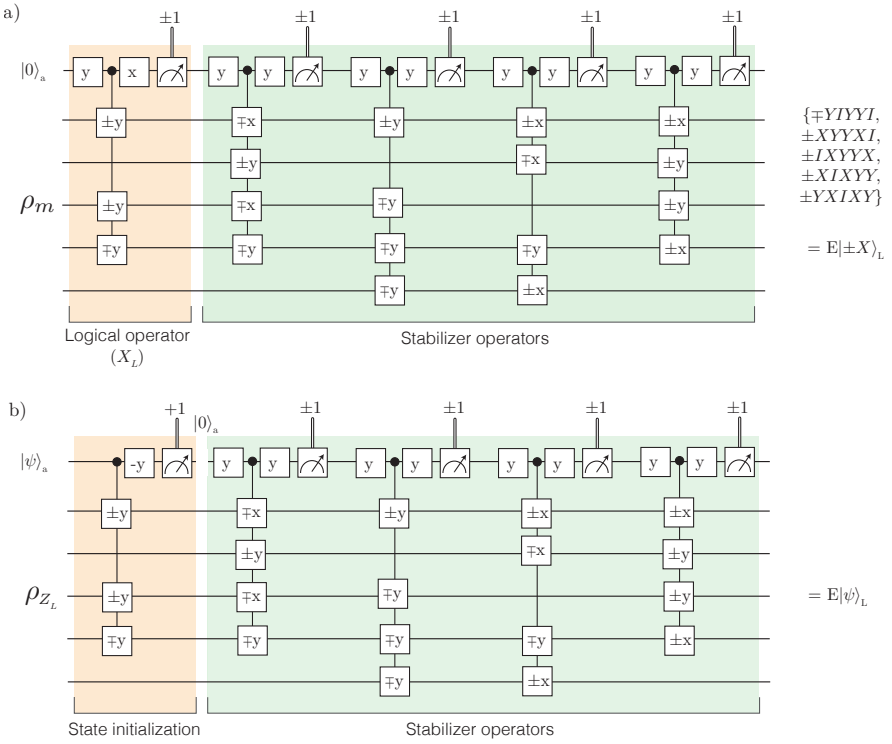


Figure 6.3 — Logical state initialization for five-qubit encoding. A logical state is encoded in five data qubits either **(a)** from a fully mixed state by first measuring the logical operator corresponding to the required logical state (here logical operator X_L to obtain $|X\rangle_L$) or (**b**) via the ancilla qubit. An arbitrary state can be initialized on the data qubits which are stabilized by $Z_L = ZZZZZ$. To initialize in the code space, in both cases, four orthogonal stabilizer operators are subsequently measured, taking into account extra basis rotations corresponding to the gate implementation in our system. The final state is the positive or negative eigenstate of the chosen logical operator, with at most one single-qubit error that is 'detected' by the four stabilizer measurements and can thus be corrected by a single-qubit operation or Pauli update as given in Tab. 6.1.

- An arbitrary logical state can be initialized via the ancilla qubit, as employed in Ch. 5. For example, after initializing the data qubits in an eigenstate of $ZZZZZ$, the sequence shown in Fig. 6.3b initializes an arbitrary state on the logical qubit and projects the data qubits in the code space by the stabilizer measurements.

Dependent on the measurement outcomes of all stabilizer measurements and the projection of the logical operator, the final state is at most one single-qubit error and a logical bit-flip away from the intended logical state. The code space can be defined by the stabilizer measurement outcomes. In rounds of QEC (next section), errors are detected when stabilizer measurement outcomes switch sign ('click').

6.3.2 Error syndrome detection and correction

Once a logical qubit is encoded in the five data qubits, errors are detected by stabilizer measurements via the ancilla qubit. The five-qubit code detects and distinguishes single X, Y and Z errors on the data qubits. The combination of four stabilizer measurement outcomes forms the four-bit error syndrome; the information that is required to succesfully correct general single-qubit errors in the encoded system.

After the logical qubit initialization (Sec. 6.3.1, Fig. 6.3), the code space is defined by the stabilizer operators given in Eq. 6.1. Taking into account basis rotations due to our two-qubit gates that transform the Pauli frame, errors are detected by a chosen set of orthogonal stabilizer measurements (Fig. 6.4), corresponding to the operators of Eq. 6.1. The sequence given in Fig. 6.3 corresponds to the measurements of stabilizer operators:

$$K^{a'} = XYXYI, \qquad K^{b'} = ZIZYY, \qquad K^{c'} = YZIYZ, \qquad K^{d'} = YXZZI. \tag{6.3}$$

By transformations of the Pauli frame errors also transform through the circuit. An initial error on a data qubit, corresponding to a detected syndrome by the sequence of Fig. 6.4 (corresponding to Eq. 6.3) requires a correcting operation given in Tab. 6.1 and transforms the system to the Pauli frame given by the stabilizer operators of Eq. 6.3. Reversing the sequence of Fig. 6.4 (equal to the order of stabilizer measurements of Fig. 6.3) symmetrizes the sequence and transforms the system to the Pauli frame given by the stabilizer operators of Eq. 6.1. This combination of rounds of detecting errors can be convenient but are not a requirement to the experiment as the basis rotations only require processing in software and no additional overhead in the quantum processor.

6.3.3 Proposed experimental implementation

The control of five nuclear spins via the NV electron spin can allow for the implementation of five-qubit quantum error correction. The spin register can be initialized in a logical state and error detection and correction can be performed. In this section I will propose initial experiments to determine the feasibility of the full implementation of five-qubit quantum error correction.

Error		I	X_1	Y_1	Z_1	X_2	Y_2	Z_2	X_3	Y_3	Z_3	X_4	Y_4	Z_4	X_5	Y_5	Z_5
Syndrome	K^a	+	+	-	-	-	+	-	-	+	-	+	-	-	+	+	+
	K^b	+	+	-	-	-	-	+	+	+	+	-	-	+	+	-	-
	K^c	+	-	+	-	+	+	+	-	+	-	-	-	+	-	-	+
	K^d	+	-	-	+	+	-	-	+	-	-	-	-	+	+	+	+
Correction		I	Y_1	Z_1	X_1	Y_2	X_2	Z_2	X_3	Z_3	Y_3	Z_4	X_4	Y_4	Z_5	X_5	Y_5

Table 6.1 —Unique pattern of positive (+) and negative (-) measurement outcomes for a combination of measurements of the four stabilizer operators for the five-qubit QEC code and required correction. Inital errors X_i, Y_i and Z_i on data qubit i corresponding to the outcomes of the measurement of the set of stabilizer operators (K) given in Fig. 6.4, corresponding to Eq. 6.3, result in a unique error syndrome. 'Error' and 'Correction' are interchanged for the set of stabilizer measurements in Fig. 6.3 corresponding to the stabilizer operators of Eq. 6.1.

State initialization by five-qubit QEC

As a first demonstration of five-qubit QEC, the initialization sequence shown in Fig. 6.3a contains all required elements. The sequence combines initialization and a first round of general QEC on the five-qubit logical state. Starting in a five-qubit mixed state, the circuit of Fig. 6.3a projects the codeword by measurement of the logical operator and the code space by measurement of four stabilizer operators. This effectively initializes the five-qubit register in a defined logical state that deviates from the intended logical state by at most a logical bit flip, dependent on the measurement outcome of the logical operator, and a single-qubit Pauli operation, dependent on the stabilizer measurement outcomes (the 'error syndrome'). Correspondingly, a correction is either just a single-qubit Pauli operation or a Pauli frame update (Tab. 6.1).

The initialization procedure (Fig. 6.3) results in $2^5 = 32$ possible final five-qubit states, defined by the five ancilla measurement outcomes. Postselection of the final state, dependent on the detected syndrome, gives insight in the initialization fidelity of the logical state, as well as in the fidelity of the stabilizer measurements. The detected 'error' can be actively corrected by the adaption of further operations on the data qubits. Feedback can be applied to keep the ancilla qubit in the optimal state throughout the experiment (Ch. 5).

State tomography of the resulting five-qubit state requires the measurement of $4^5 - 1 = 1023$ expectation values in the full Pauli set. The five-qubit state fidelity after initialization in a logical state is obtained by measurement of the corresponding $2^5 = 31$ non-zero expectation values in the Pauli set. Logical state tomography is performed by measurement of three logical operators via the ancilla qubit (e.g. $X_L = -IYXYI$, $Y_L = -YIXXI$ and $Z_L = -YIZIY$). To determine the quality of the experimental encoding, process fidelity of the sequence in Fig. 6.3 can be determined by initializing in the eigenstates of logical Clifford gates, defining:

$$F_p = \frac{1}{4}(F_X + F_{-X} + F_Y + F_{-Y} + F_Z + F_{-Z} - 2), \tag{6.4}$$

with F_α the logical output state fidelity to the intended state $|\alpha_L\rangle$.

Once the logical qubit is encoded in the five-qubit register as described in this section, a

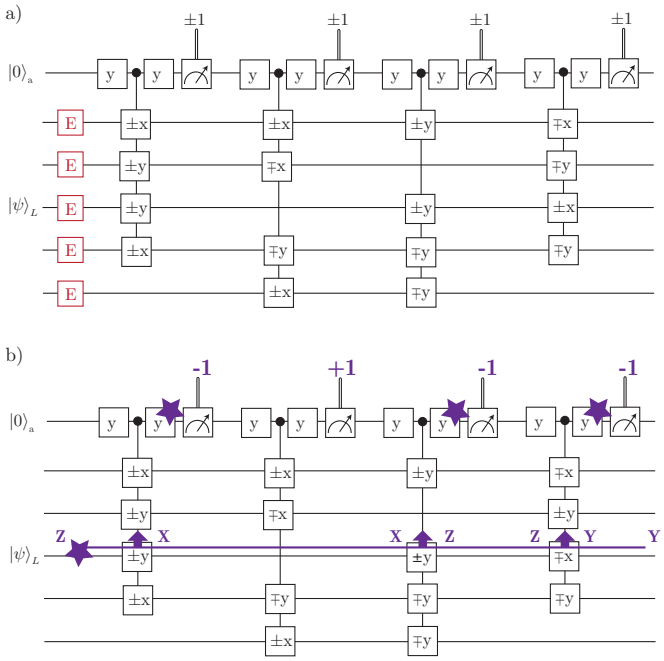


Figure 6.4 — Five-qubit QEC on a logical encoded qubit, taking into account basis rotations. a, The combination of four stabilizer measurements on the data qubits uniquely detects general single-qubit errors on the data qubits. The stabilizer measurements are compiled to take into account extra basis rotations due to our gate implementation. **b**, Example of an initial Z error on data qubit 3. The error propagates through the circuit. This particular error propagates to the ancilla qubit in three out of four stabilizer measurements and thus results in the syndrome $\{-1, +1, -1, -1\}$, see Tab. 6.1.

next round of QEC can be performed following Fig. 6.4a. To characterize the QEC code, single-qubit errors around all axes can be applied on the initialized state and analyzed according to Tab. 6.1.

6.4 Discussion

In this chapter, I proposed the experimental implementation of two general quantum codes that can detect and correct general errors on the data qubits. The implementation of such codes requires the extension of the nuclear spin register, exploiting the experimental implementation of Ch. 5. The natural gates between the NV electron spin and a nuclear spin cause extra basis rotations on the data qubits in the encoding, transforming the Pauli frame

(Chs. 4, 5). These transformations are taken into account in the compiling of the protocol to our experimental implementation.

First demonstrations of such general quantum error detection and correction codes with spins in diamond, detecting and/or correcting single-qubit X, Y and Z errors, include logical qubit Initialization by correlation measurements on a register of data qubits via the ancilla qubit. initializing the logical states by stabilizer measurements can be considered as a first round of error detection that characterizes the experimental implementation of these protocols.

6.5 Bibliography

[1] P. W. Shor. Scheme for reducing decoherence in quantum computer memory. *Physical Review A* **52**, R2493 (1995).

[2] A. M. Steane. Error Correcting Codes in Quantum Theory. *Physical Review Letters* **77**, 793 (1996).

[3] S. B. Bravyi and A. Y. Kitaev. Quantum codes on a lattice with boundary. *arXiv:quant-ph/9811052* (1998).

[4] R. Raussendorf and J. Harrington. Fault-Tolerant Quantum Computation with High Threshold in Two Dimensions. *Physical Review Letters* **98**, 190504 (2007).

[5] E. Knill, R. Laflamme, R. Martinez and C. Negrevergne. Benchmarking Quantum Computers: The Five-Qubit Error Correcting Code. *Physical Review Letters* **86**, 5811 (2001).

[6] J. Chiaverini *et al.* Realization of quantum error correction. *Nature* **432**, 602 (2004).

[7] P. Schindler *et al.* Experimental Repetitive Quantum Error Correction. *Science* **332**, 1059 (2011).

[8] D. Nigg *et al.* Quantum computations on a topologically encoded qubit. *Science* 1253742 (2014).

[9] M. D. Reed *et al.* Realization of three-qubit quantum error correction with superconducting circuits. *Nature* **482**, 382 (2012).

[10] B. P. Lanyon *et al.* Measurement-Based Quantum Computation with Trapped Ions. *Physical Review Letters* **111**, 210501 (2013).

[11] G. Waldherr *et al.* Quantum error correction in a solid-state hybrid spin register. *Nature* **506**, 204 (2014).

[12] A. D. Córcoles *et al.* Demonstration of a quantum error detection code using a square lattice of four superconducting qubits. *Nature Communications* **6**, 6979 (2015).

[13] D. Ristè *et al.* Detecting bit-flip errors in a logical qubit using stabilizer measurements. *Nature Communications* **6** (2015).

[14] J. Kelly *et al.* State preservation by repetitive error detection in a superconducting quantum circuit. *Nature* **519**, 66 (2015).

[15] N. Ofek *et al.* Extending the lifetime of a quantum bit with error correction in superconducting circuits. *Nature* **536**, 441 (2016).

[16] T. Unden *et al.* Quantum Metrology Enhanced by Repetitive Quantum Error Correction. *Physical Review Letters* **116**, 230502 (2016).

[17] T. H. Taminiau *et al.* Detection and Control of Individual Nuclear Spins Using a Weakly Coupled Electron Spin. *Physical Review Letters* **109**, 137602 (2012).

[18] T. H. Taminiau, J. Cramer, T. v. d. Sar, V. V. Dobrovitski and R. Hanson. Universal control and error correction in multi-qubit spin registers in diamond. *Nature Nanotechnology* **9**, 171 (2014).

[19] E. Knill. Quantum computing with realistically noisy devices. *Nature* **434**, 39 (2005).

[20] S. J. Devitt. Performing Quantum Computing Experiments in the Cloud. *arXiv:1605.05709 [quant-ph]* (2016).

[21] M. Grassl, T. Beth and T. Pellizzari. Codes for the quantum erasure channel. *Physical Review A* **56**, 33 (1997).

[22] N. D. Mermin. *Quantum computation and quantum information*. Cambridge University Press, Cambridge (2007).

[23] D. Gottesman. Class of quantum error-correcting codes saturating the quantum Hamming bound. *Physical Review A* **54**, 1862 (1996).

[24] R. Laflamme, C. Miquel, J. P. Paz and W. H. Zurek. Perfect Quantum Error Correcting Code. *Physical Review Letters* **77**, 198 (1996).

[25] S. J. Devitt, W. J. Munro and K. Nemoto. Quantum error correction for beginners. *Reports on Progress in Physics* **76**, 076001 (2013).

Chapter 7

Conclusions and outlook

J. Cramer

The future of quantum technology requires the protection of quantum information against uncontrollable errors. The results in this thesis present the NV centre as a hybrid quantum node and implement active quantum error correction on a continuously encoded quantum state in spins in diamond. These methods and results can be extended to the experimental implementation of general quantum error correction protocols. The developed quantum register based on spins in diamond can be employed as a local node for quantum networks as basis for other multi-qubit experiments. In this chapter I will summarize the results of this thesis and address future research directions.

7.1 Conclusions

This thesis presents the experimental implementation of quantum error correction based on a spin register in diamond. In the first experiments at ambient temperature, errors are detected by encoding in three spins and corrected after decoding to a single spin (Ch. 4), leaving the quantum state unprotected. In the work presented in Ch. 5 errors are detected and corrected on a continuously encoded quantum state in nuclear spins in diamond by stabilizer measurements and real-time feedback, enabled by high-fidelity single-shot readout of the NV electron spin as ancilla qubit at cryogenic temperatures. The results presented in this thesis can be summarized as follows:

- Universal control over deterministically available multi-qubit spin registers is realized via the electron spin of NV centres in diamond. Multiple ^{13}C spins in the spin bath of such NV centres are selectively initialized, controlled and read out.

- Single-shot correlation measurements of ^{13}C spins can be performed via the electron spin of the NV centre, without projecting the individual nuclear spin states. Moreover, feedback can be applied while protecting coherence in the projected subspaces of these spin states.

- Multiple rounds of active quantum error correction are performed on a continuously protected logical qubit in a spin register in diamond, demonstrating robustness against phase errors on the data qubits in the encoding.

- A logical quantum superposition state is preserved beyond the natural dephasing time of the best physical qubit in the encoding.

- By extending the number of individually controlled ^{13}C spins general quantum error detection and correction protocols are within reach by the implementation of stabilizer measurements and feedback via the NV electron spin.

Combining the recent results on the long-distance coupling of NV centres [1,2] via photonic channels [3] with the presented control of quantum spin registers in diamond makes the NV centre a promising platform for the implementation of quantum networks [4–6]. Extending the number of spins controlled via the NV centre electron spin, as well as improving the rate and efficiency of the coupling between distant NV centres allows for the exploration of more advanced quantum error correction protocols, first applications in quantum technology and other related experiments.

7.2 Extended quantum error correction protocols

Protecting quantum states against general errors requires the extension of the experimental methods presented in this thesis to a larger register of data qubits. First experiments based on four or five nuclear spins are within reach employing current control methods as proposed in Ch. 6. While it is still an open question how many nuclear spins can be controlled via the NV centre, the characterization of the nuclear spins in the NV centre's spin bath, shown in Chs. 4, 5 indicates that more than the three spins used in the presented experiments can be controlled as qubits. It is expected that the current quantum register in diamond can be extended to a larger number of qubits by exploring different methods of control[7,8].

The two-qubit gates between the NV electron spin and a ^{13}C nuclear spin mainly rely on the perpendicular component of the hyperfine interaction[9]. Nuclear spins with relatively small perpendicular hyperfine coupling to the NV electron spin, require long dynamical decoupling gates and can be difficult to control individually. This can be overcome by combining the decoupling gates with radio-frequency pulses, directly driving the nuclear spins, using a similar approach to earlier work on the control of the nitrogen spin of the NV centre[10]. To avoid gate errors by discretization and to increase spin-selectivity on the nuclear gates, elaborated decoupling sequences built-up by non-equally spaced decoupling elements can be explored[8]. For the numerical optimization of such gates, detailed simulations of the system are required[11].

Flexibility in the spin-selective control of nuclear spins can be increased by using the third spin level of the electron spin state. Decoupling the NV electron spin between the ($m_s = 0 \leftrightarrow m_s = +1$) transition or the ($m_s = 0 \leftrightarrow m_s = -1$) transition results in a different resonant interaction with each nuclear spin (Ch. 3). Where decoupling on one transition allows for high-fidelity, individual control of certain nuclear spins, for other spins the other electron transitions can be more favorable. Combining both electron transitions in a single experiment can therefore increase the number of controllable nuclear spins in a single experiment. This requires coherent and robust population transfer between the $m_s = -1 \leftrightarrow m_s = +1$ spin states[12].

The coherence times of quantum states in spins in diamond can be extended with various methods. Purified diamond samples[13,14], containing a lower density of nuclear spins, or selective co-implantation of closely coupled NV centres[15] and local nuclear spins can enhance the natural coherence times of both electron and nuclear spins. The interactions between nuclear spins in the spin bath cause uncontrolled spin flips and dephasing of the nuclear spin qubits. The dephasing effects can be suppressed by methods such as decoupling the nuclear spins[16,17] and polarization of the nuclear spin bath. Uncontrolled spin-flips between nuclear spins are strongly suppressed by storing the NV electron spin in the $m_s = -1$ or $m_s = +1$ spin states[17,18]. While the current operations on the nuclear spins involve the $m_s = 0$ spin level, this effect can be studied in more detail[17]. Furthermore, when nuclear spins have strongly correlated noise, decoherence-protected subspaces[19] can be used to suppress such noise; by encoding a quantum state in a combined spin state of two such nuclear spins the dephasing can cancel out.

Extending the number of nuclear spins in the encoding allows for the implementation of more elaborate quantum error correction codes[20], such as the seven[21] or nine[22] qubit

QEC codes. Quantum error corrected logical qubit operations can be implemented and explored. Repeated rounds of quantum error correction allow for characterization [23] and optimization [24,25] of the experimental QEC protocols.

7.3 Quantum networks

The presented local control over a spin register in diamond and the recent advances in the realization of quantum entanglement over macroscopic distances [1,2,26] can become the building blocks of a multi-node quantum network [4,5] as illustrated in Fig. 7.1. These networks can be used to study both fundamental questions as well as future applications. Large macroscopic multi-qubit quantum entangled states can be generated as a basis for experiments on fundamental and technical questions in quantum mechanics. In such a network, measurement-based quantum computing can be implemented [27,28] and device-independent quantum key distribution can be studied [29,30].

The local spin register in diamond combined with photonic coupling between distant NV centres is a promising platform to develop such a network [1,4,31]. The proposed networks [4] allow for reasonably high error thresholds in the entanglement generation (on the order of ten percent) if the local errors are on the order of one percent. To efficiently develop such networks, the rate of entanglement generation between distant nodes should exceed the local memory lifetime. The two main requirements for such networks are the ability to create links

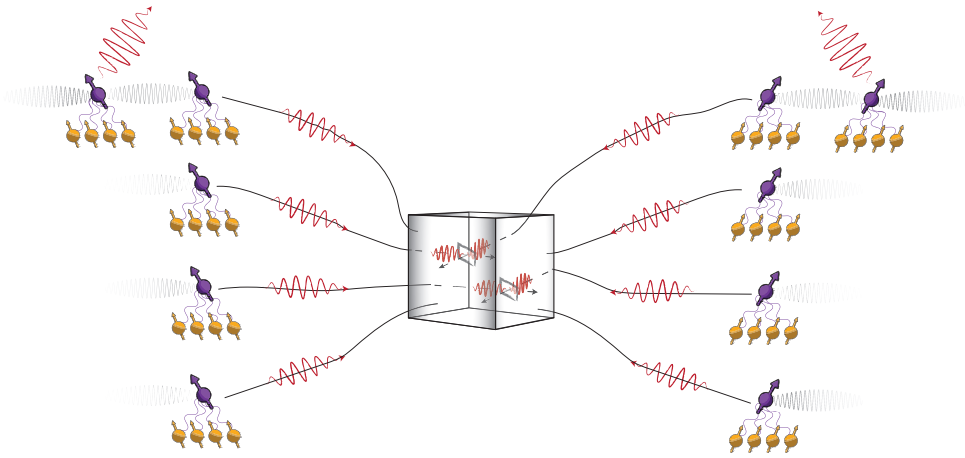


Figure 7.1 — Towards quantum networks based on spins in diamond. The envisioned quantum network consists of local nodes of NV centres that are each coupled to a nuclear spin register. These nodes can be coupled via photonic channels and by direct coupling between closeby NV centres.

via photonic channels and long-lived local memories that can be stored while the networking links are generated.

First, for long memory lifetimes, the stored quantum information in the nodes should not be disturbed by the generation of entanglement to other nodes. During optical excitation, readout and reset of the NV electron spin required for the entanglement generation, the electron spin state is unknown. The nuclear spins that are used in this thesis are weakly coupled to the NV electron spin. Recent work[32,33] has shown that such weakly coupled spins can withstand in the order of hundreds of attempts of entanglement generation. Quantum states in decoherence-protected subspaces based on two of these spins can be robust to ~ 1000 attempts, the order of attempts currently required to generate one entanglement event[26].

Secondly, for efficient entanglement generation, the photon collection efficiency can be improved[2]. The current entanglement generation protocol between NV centres in diamond relies on the emission and detection of indistinguishable photons[1] in two consecutive rounds of single-photon detection events[34]. Only $\sim 4\%$ of the emitted photons is suitable for entanglement generation and these photons are emitted omnidirectional. The efficiency of photon emission can be improved by means of a micro-cavity, controlling both the spectral and spatial properties of the emitted photons[35–37]. Furthermore, the detection of these photons can be improved by decreasing the photon loss over distance. At the wavelength of the naturally emitted photon (637 nm), losses in optical fibers are in the order of 5 dB/km. By downconverting the emitted photons of the NV centre to telecom wavelengths[38], these losses can be decreased to 0.2 dB/km.

The fidelity of entanglement between such nodes can be improved by entanglement purification[31], employing nuclear spins in the entanglement generation protocol. Remote entanglement between NV centres is swapped[39] to coupled nuclear spins, repeating the entanglement generation, purifying the entanglement probabilistically. By using entanglement purification, the entanglement protocol can be relaxed to a single-photon heralding scheme[40]. This makes the impact of photon loss on failure linear, versus quadratic in the two-photon protocol[34].

7.4 Other related experiments

Apart from the interest in future applications in quantum computing and quantum networks, the proposed research directions can also be used for fundamental research. The generation of larger entangled states and qubit registers, as well as the generation of macroscopic quantum states invites to explore fundamental limitations of quantum information[29].

The stabilizer measurements employed in this thesis, using the NV electron spin to detect correlations between nuclear spin qubits, are of interest beyond quantum error correction. The ability to project correlations in logical quantum states, without projecting individual qubits, allows for the study of the effect of such measurements. Our recent work on the repeated projection of correlations, generating Zeno subspaces, allow for the exploration of effects of such repeated measurements on different types of noise and other dynamics between quantum states[18].

Furthermore, the NV centre has shown to be a very precise sensor in many applications

such as living cells[41], single spins[42] and temperature[43]. The NV centre can be used to sense fields outside of the diamond when placed close enough to the surface[44,45]. However, spectral diffusion and instability of the NV centres complicate these applications. Repeated sensing with nuclear spins as (error-corrected) memory[46], and adaptive protocols[47] while using real-time feedback could improve these applications.

7.5 Bibliography

[1] H. Bernien *et al.* Heralded entanglement between solid-state qubits separated by three metres. *Nature* **497**, 86 (2013).

[2] B. Hensen. *Quantum nonlocality with spins in diamond*. PhD Thesis, Delft, University of Technology (2016).

[3] L. Robledo, H. Bernien, I. van Weperen and R. Hanson. Control and Coherence of the Optical Transition of Single Nitrogen Vacancy Centers in Diamond. *Physical Review Letters* **105**, 177403 (2010).

[4] N. H. Nickerson, Y. Li and S. C. Benjamin. Topological quantum computing with a very noisy network and local error rates approaching one percent. *Nature Communications* **4**, 1756 (2013).

[5] H. J. Kimble. The quantum internet. *Nature* **453**, 1023 (2008).

[6] N. H. Nickerson, J. F. Fitzsimons and S. C. Benjamin. Freely Scalable Quantum Technologies Using Cells of 5-to-50 Qubits with Very Lossy and Noisy Photonic Links. *Physical Review X* **4**, 041041 (2014).

[7] F. Dolde *et al.* High-fidelity spin entanglement using optimal control. *Nature Communications* **5**, 3371 (2014).

[8] J. Casanova, Z.-Y. Wang, J. F. Haase and M. B. Plenio. Robust dynamical decoupling sequences for individual-nuclear-spin addressing. *Physical Review A* **92**, 042304 (2015).

[9] T. H. Taminiau *et al.* Detection and Control of Individual Nuclear Spins Using a Weakly Coupled Electron Spin. *Physical Review Letters* **109**, 137602 (2012).

[10] T. van der Sar. *Quantum control of single spins and single photons in diamond*. PhD Thesis, Delft, University of Technology (2012).

[11] M. J. G. Scheer. *Spins in the rough: finding 13C nuclear spins near a nitrogen-vacancy center in diamond*. BSc Thesis, Providence, Brown University (2016).

[12] A. J. Stolk. *Better control of weakly coupled 13C spins surrounding an NV-centre*. MSc Thesis, Delft, University of Technology (2016).

[13] P. C. Maurer *et al.* Room-Temperature Quantum Bit Memory Exceeding One Second. *Science* **336**, 1283 (2012).

[14] G. Balasubramanian *et al.* Ultralong spin coherence time in isotopically engineered diamond. *Nature Materials* **8**, 383 (2009).

[15] F. Dolde *et al.* Room-temperature entanglement between single defect spins in diamond. *Nature Physics* **9**, 139 (2013).

[16] J. Casanova, Z.-Y. Wang and M. B. Plenio. Noise-resilient Quantum Computing with a Nitrogen-Vacancy Center and Nuclear Spins. *arXiv:1602.06862 [quant-ph]* (2016).

[17] M. Bakker. *Frozen core spin dynamics in diamond.* MSc Thesis, Delft, University of Technology (2015).

[18] N. Kalb *et al.* Experimental creation of quantum Zeno subspaces by repeated multi-spin projections in diamond. *Nature Communications* **7**, 13111 (2016).

[19] D. A. Lidar. Review of Decoherence Free Subspaces, Noiseless Subsystems, and Dynamical Decoupling. *Adv. Chem. Phys.* **154**, 295 (2014).

[20] J. Preskill. Fault-tolerant quantum computation. *arXiv:quant-ph/9712048* (1997).

[21] A. M. Steane. Error Correcting Codes in Quantum Theory. *Physical Review Letters* **77**, 793 (1996).

[22] P. W. Shor. Fault-tolerant quantum computation. *Proceedings of the 37th IEEE Symposium on foundations of computer science* (1996).

[23] E. Magesan *et al.* Efficient Measurement of Quantum Gate Error by Interleaved Randomized Benchmarking. *Physical Review Letters* **109**, 080505 (2012).

[24] A. J. Landahl, J. T. Anderson and P. R. Rice. Fault-tolerant quantum computing with color codes. *arXiv:1108.5738 [quant-ph]* (2011).

[25] A. G. Fowler, D. Sank, J. Kelly, R. Barends and J. M. Martinis. Scalable extraction of error models from the output of error detection circuits. *arXiv:1405.1454 [quant-ph]* (2014).

[26] W. Pfaff *et al.* Unconditional quantum teleportation between distant solid-state quantum bits. *Science* **345**, 532 (2014).

[27] C. Monroe *et al.* Large-scale modular quantum-computer architecture with atomic memory and photonic interconnects. *Physical Review A* **89**, 022317 (2014).

[28] S. Barz *et al.* Demonstration of Blind Quantum Computing. *Science* **335**, 303 (2012).

[29] A. Ekert and R. Renner. The ultimate physical limits of privacy. *Nature* **507**, 443 (2014).

[30] A. Acín *et al.* Device-Independent Security of Quantum Cryptography against Collective Attacks. *Physical Review Letters* **98**, 230501 (2007).

[31] W. Dür, H.-J. Briegel, J. I. Cirac and P. Zoller. Quantum repeaters based on entanglement purification. *Physical Review A* **59**, 169 (1999).

[32] A. Reiserer *et al.* Robust Quantum-Network Memory Using Decoherence-Protected Subspaces of Nuclear Spins. *Physical Review X* **6**, 021040 (2016).

[33] M. S. Blok, N. Kalb, A. Reiserer, T. H. Taminiau and R. Hanson. Towards quantum networks of single spins: analysis of a quantum memory with an optical interface in diamond. *Faraday Discussions* **184**, 173 (2015).

[34] S. D. Barrett and P. Kok. Efficient high-fidelity quantum computation using matter qubits and linear optics. *Physical Review A* **71**, 060310 (2005).

[35] D. Hunger *et al.* A fiber Fabry–Perot cavity with high finesse. *New Journal of Physics* **12**, 065038 (2010).

[36] R. Albrecht, A. Bommer, C. Deutsch, J. Reichel and C. Becher. Coupling of a Single Nitrogen-Vacancy Center in Diamond to a Fiber-Based Microcavity. *Physical Review Letters* **110**, 243602 (2013).

[37] H. Kaupp *et al.* Scaling laws of the cavity enhancement for nitrogen-vacancy centers in diamond. *Physical Review A* **88**, 053812 (2013).

[38] S. Zaske *et al.* Visible-to-Telecom Quantum Frequency Conversion of Light from a Single Quantum Emitter. *Physical Review Letters* **109**, 147404 (2012).

[39] C. H. Bennett, D. P. DiVincenzo, J. A. Smolin and W. K. Wootters. Mixed State Entanglement and Quantum Error Correction. *Physical Review A* **54**, 3824 (1996).

[40] E. T. Campbell and S. C. Benjamin. Measurement-Based Entanglement under Conditions of Extreme Photon Loss. *Physical Review Letters* **101**, 130502 (2008).

[41] G. Kucsko *et al.* Nanometre-scale thermometry in a living cell. *Nature* **500**, 54 (2013).

[42] T. H. Taminiau, J. Cramer, T. v. d. Sar, V. V. Dobrovitski and R. Hanson. Universal control and error correction in multi-qubit spin registers in diamond. *Nature Nanotechnology* **9**, 171 (2014).

[43] D. M. Toyli, C. F. de las Casas, D. J. Christle, V. V. Dobrovitski and D. D. Awschalom. Fluorescence thermometry enhanced by the quantum coherence of single spins in diamond. *Proceedings of the National Academy of Sciences of the United States of America* **110**, 8417 (2013).

[44] H. J. Mamin *et al.* Nanoscale Nuclear Magnetic Resonance with a Nitrogen-Vacancy Spin Sensor. *Science* **339**, 557 (2013).

[45] T. Staudacher *et al.* Nuclear Magnetic Resonance Spectroscopy on a (5-Nanometer)3 Sample Volume. *Science* **339**, 561 (2013).

[46] T. Unden *et al.* Quantum Metrology Enhanced by Repetitive Quantum Error Correction. *Physical Review Letters* **116**, 230502 (2016).

[47] M. S. Blok *et al.* Manipulating a qubit through the backaction of sequential partial measurements and real-time feedback. *Nature Physics* **10**, 189 (2014).

Summary

Quantum error correction with spins in diamond

Digital information based on the laws of quantum mechanics promisses powerful new ways of computation and communication. However, quantum information is very fragile; inevitable errors continuously build up and eventually all information is lost. Therefore, realistic large-scale quantum information processing requires the protection of quantum bits (qubits) against errors. In this thesis we present the experimental implementation of quantum error correction protocols based on spins in diamond. In such protocols, a quantum state is protected against errors by encoding in multiple qubits. Errors can be detected and corrected by measurement of correlations, so-called stabilizer-measurements, on these qubits.

The experimental work presented in this thesis employs multiple spins in diamond as qubits to explore and implement error correction protocols. The nitrogen-vacancy (NV) centre in diamond is a lattice defect consisting of a nitrogen atom (N) and a vacancy (V) on two adjacent diamond lattice sites. This defect effectively results in an electronic spin that can be addressed as a qubit. The spin state can be manipulated by microwave fields and optically read out. At liquid helium temperatures (cryogenic temperature, ~ 4 K = -269 °C), the NV electron spin provides high-fidelity single-shot readout and long coherence times.

The NV centre is surrounded by naturally available (1.1% abundance) nuclear ^{13}C spins. As the number of spins that are close enough to the NV centre to be strongly coupled is limited, we employ the weakly coupled nuclear spins in the spin bath of the NV centre. Using dynamical decoupling techniques these nuclear spins can be detected via the NV electron spin through the hyperfine interaction. The nuclear spins are long-lived and robust against optical excitation of the NV electron spin, which can make these spins a robust quantum register for quantum error correction.

In Ch. 4 we demonstrate universal control over multiple of such weakly coupled nuclear ^{13}C spins in the environment of the NV centre at ambient temperatures. We demonstrate initialization, control and read-out of individual nuclear spins. Finally, we implement a quantum error correction protocol by encoding a quantum state in the NV electron spin and two nuclear spins. Errors are detected by un-encoding the quantum state back to the electron spin and correction via a double controlled operation.

For universal fault-tolerant quantum computations it is essential that the quantum information remains encoded at all times. In Ch. 5 we present multiple rounds of quantum error correction and active feedback on a continuously encoded qubit at cryogenic temperatures. A quantum state is protected by encoding in three weakly coupled spins. Errors are detected via high-fidelity non-demolition readout of the NV electron spin and actively corrected using fast classical electronics. We demonstrate that an actively error-corrected qubit is robust against phase flip errors and show that a superposition state can live longer than the best physical qubit in the encoding.

The presented methods and results can be extended to a range of future experiments. In Ch. 6 we propose the implementation of five-qubit quantum error correction, the smallest code to correct for general single-qubit errors on the physical qubits in the encoding, by extending the experimental methods as developed in Chs. 4&5. Besides the exploration and

development of larger error correction protocols and fault-tolerant quantum computing, the presented quantum register based in spins in diamond can be employed as a quantum node and combined with recent advances in the realization of quantum entanglement over large distances to form quantum networks. These networks can be used to study both fundamental questions as well as future applications in quantum information technology.

Samenvatting

Quantumfoutcorrectie met spins in diamant

Digitale informatie gebaseerd op de wetten van de quantummechanica belooft nieuwe, krachtige methodes voor berekeningen en communicatie. Maar quantuminformatie is heel kwetsbaar; onvermijdelijke fouten bouwen continu op waardoor de informatie verloren gaat. Voor realistische quantuminformatie op grote schaal is het daarom noodzakelijk om quantumbits (qubits) te beschermen tegen fouten. In dit proefschrift presenteren we de experimentele implementatie van quantumfoutcorrectieprotocollen gebaseerd op spins in diamant. In deze protocollen is een quantumtoestand beschermd tegen fouten door deze te encoderen in meerdere qubits. Fouten kunnen worden gedetecteerd en gecorrigeerd door correlaties tussen deze qubits te meten.

Het experimentele werk dat in dit proefschrift wordt gepresenteerd maakt gebruik van meerdere spins in diamant als qubits om quantumfoutcorrectieprotocollen te onderzoeken en implementeren. Het stikstof-gat (nitrogen-vacancy, NV) centrum is een roosterdefect in diamant waarbij een stikstof atoom (N) en een gat (V) twee naastgelegen roosterpunten bezetten. Deze combinatie resulteert effectief in een elektronspin die kan worden aangestuurd als qubit. De spintoestand kan worden gemanipuleerd door microgrolfvelden en optisch worden uitgelezen. Op de temperatuur van vloeibaar helium (cryogene temperatuur, ~ 4 K$= -269^{\circ}$C) kan de elektronspin met hoge betrouwbaarheid in een keer worden uitgelezen en heeft deze een lange coherentietijd.

Het NV centrum is omgeven door ^{13}C kernspins (1.1% natuurlijke aanwezigheid in het rooster). Het aantal kernspins die zo dicht bij het NV centrum zitten dat deze sterk gekoppeld zijn, is gelimiteerd, daarom gebruiken we zwak gekoppelde kernspins uit het spinbad van het NV centrum. Door gebruik te maken van dynamische ontkoppelingstechnieken kunnen dit soort spins worden gedetecteerd dankzij de hyperfijne interactie met de elektronspin van het NV centrum. Deze kernspins kunnen hun toestand lang behouden en zijn bestand tegen optische excitatie van de elektronspin van het NV centrum, waardoor ze een robuust quantum register kunnen vormen voor quantumfoutcorrectie.

In hoofdstuk 4 demonstreren we de universele controle van meerdere van zulke zwak gekoppelde ^{13}C spins in de omgeving van het NV centrum bij kamertemperatuur. We demonstreren het initialiseren, controleren en uitlezen van individuele kernspins. Uiteindelijk implementeren we een quantumfoutcorrectieprotocol door een quantumtoestand te encoderen in de elektronspin van het NV centrum en twee kernspins. Fouten worden gedetecteerd door de quantumtoestand terug te brengen naar de elektronspin en gecorrigeerd door een dubbel-gecontroleerde quantumoperatie.

Voor universele fout-tolerante quantumberekeningen is het essenteel dat de quantuminformatie altijd geëncodeerd blijft. In hoofdstuk 5 presenteren we de implementatie van meerdere rondes quantumfoutcorrectie en actieve terugkoppeling op een continu geëncodeerde qubit bij cryogene temperatuur. Een quantumtoestand is beschermd door deze te encoderen in drie zwakgekoppelde spins en actief gecorrigeerd door gebruik te maken van snelle klassieke electronica. We demonstreren dat een actief fout-gecorrigeerde qubit robuust is tegen fasefouten en laten ziet dat een superpositie langer bewaard kan blijven dan de beste fysieke qubit in het geëncodeerde systeem.

De gepresenteerde methodes en resultaten kunnen worden uitgebreid naar een spectrum aan toekomstige experimenten. In hoofdstuk 6 stellen we de implementatie van vijf-qubit quantumfoutcorrectie voor, de kleinste code om algemene enkele-qubit fouten op de qubits in de geëncodeerde toestand te corrigeren, door de ontwikkelde experimentele methodes uit te breiden. Naast het bestuderen en ontwikkelen van grotere quantumfoutcorrectieprotocollen en fout-tolerante quantumberekeningen kan het gepresenteerde quantum register van spins in diamant worden gebruikt als quantumknooppunt en worden gecombineerd met de recente ontwikkelingen in het realiseren van quantumverstrengeling over lange afstanden als basis voor quantumnetwerken. Deze netwerken kunnen worden gebruikt om zowel fundamentele vragen te bestuderen en toekomstige toepassingen in quantuminformatietechnologie te onderzoeken.

Acknowledgements

At the end of my bachelors program in Applied Physics, I wanted to become a science journalist. Science was not for me, I just had to finish my degree by doing a final research project. This project changed my idea of doing science; I was fascinated by doing experiments based on the counterintuitive laws of quantum mechanics and I was positively surprised by the atmosphere in the research group of which I learned I could be part. I decided to follow the Casimir pre-PhD masters track to find out if I should do a PhD: the answer became a clear 'YES'. I want to thank Hendrik Casimir and his granddaughter Sytske for the opportunity they gave me to continue my research in Delft.

Ronald, I want to thank you for your trust in me. Even before finishing my masters you promised me a position, independent of the outcome of the Casimir grant. For me, you are a great role model: I don't know any person that is so well-organised and so clear and confident in his own boundaries and decisions. I think this is one of the main reasons why you manage to get Team Diamond to great results every time. While you are so busy and often working remote, I always have the feeling that you know exactly what is happening in the group and you are there when really needed. And I want to thank you for introducing me to Tim when I had to write my Casimir proposal.

Tim, even before I started in Team Diamond, we became a team writing our own QEC proposals. I admire your patience and persistence with setups and people. You are always respectful and take time to explain every detail. I think I could have never wished for a better person to work so close with during these four years. My PhD would have been so different if I would not have worked with you. I did not only learn science content from you, I learned what it means to be a scientist. Thank you for everything, I am sure your new team will have a great future within QuTech!

Of course I want to thank all of Team Diamond, which in the past years I have seen transforming into a group with several specialized goals in different labs. Toeno and Gijs, while you both were gone before I started, I have enjoyed both the scientific work you did before me as well as the Diamond Spirit that you created. Wolfgang, thank you for all your creativity combined with programming skills. I learned a lot from both and it was fun to join the FOM film competition even before I joined the team. Hannes, I believe everyone should get a chance to work with you. Even in the most stressful times you kept your patience to answer the most stupid questions. Thank you for all your help and advice. Machiel, I almost started smoking to have a better reason for our short gossip breaks, both the scientific and personal discussions were always good. It is great to know that even while you are so far away you are often the first to point me at some good science communication or give more life advices! Bas, it has been an adventure to work in the same lab with you, I am impressed by your strength in both theory and experiment and visiting another lab together with you always ended up in learning much more thanks to your smart questions. It was an honour to be your paranymph and I am sure your adventure in Sydney will be great! Stefan, it was great to grow up together in the team. While our projects and paths were very different I really enjoyed our secret coffee breaks after which I think we both had renewed motivation. Norbert, I am really impressed by everthing you manage to do in such a short time while still enjoying a life outside of the university. I am sure your PhD will be a great success and I'm happy to have contributed a little to your first steps in the lab. Suus, starting as

first friends since the beginning of our study time we became collegues in Team Diamond. It is great to have a good friend so close and I really admire your persistance in your work. It is awesome to see you shine in the cavity project and I'm sure you will push it to great results! Mohamed, while you just started as Tims first real PhD student I am sure you are a great fit in the group, it was fun to help you start up a bit but soon you will be the one that knows most. Martin, thanks for all the help on the new setup, it was great to start the lab together with Tim and you. Marko, thanks for visiting our group, you added a lot and the year passed by so quickly. Slava, while I always had a hard time understanding our scientific discussions, it was always a pleasure to have you visit our group, great that you now really came to Delft. Anaïs you are a great office buddy; we ate so much chocolate during our little chats in between work! Good luck in Montpellier, you will be a great group leader. Andreas and Cristian, I am sure you are doing great in setting up your own groups, I will always remember our little conference-'holiday' in San Francisco. Peter, you will do great as a Dutch man but please never loose your accent. Sorry for shamelessly using your language skills, I do believe in your scientific value too! Adriaan and Michiel, it was great to help out with your master project, I think I learned as much as you in return! Arian, from the day you came to talk about a project I was happy to work with you. The combination of motivation, dedication and stability that you have shown will bring you very far. Lisanne, it was a lot of fun to explore working in the lab together during you bachelor project and it was good to see you come back. Maarten and Valeria, I wish you a great time, you definitely chose the right team!

Furthermore I want to thank many people within QuTech. I am very glad to have been part of the transition from QT to QuTech, which has grown to a professional institute with even more than one coffee machine! Leo DC, thank you for introducing me to the world of quantum computing and qantum error correction, I still benefit from the many things I learned from you. Leo K, thanks for building up such a great research institute. Without your vision this would not have grown so fast. Lieven, you are the most steady factor in QuTech and it is always great to have a chat with you in the hallways. Stephanie, I admire your vision and dedication and it is always fun to receive an email from our 'theory friends'. Val, while you are not part of QuTech anymore, I have enjoyed my first steps in quantum experiments with your supervision and this was a great start of my quantum adventures. Kemo, you are a great addition to the QuTech MT, thank you for all your thrust in me. Anouschka, you are the one that is not always very visible, but extremely valuable. Thanks for your help and advises. All (new) QuTech-PI's: I wish you all the best in your projects. I think it will be more and more of a joint effort and that will be a challenge with great prospects.

I believe that we would have not so much time and stability to spend all our effort on science without such dedicated staff all around us, not sticking to their job-description but all being very flexible. Marja, Chantal, Yuki, Marion and Joanna, thank you for all the work you have done. You always help thinking what is the best way to do something, arrange everything up to the smallest detail and always have time for questions. Besides that, it is always a nice break to walk in your offices. Yuki, I wish you all the best in Japan! Marja and Chantal, I am very happy that you will still be here! Heera, you have been both a friend and a great support to me. I enjoyed all our brainstorms on 'how to say it best' and I am looking forward to work together with you! All other new and 'old' QuTech staff: thanks for

your flexibility and enthusiasm! Bram, Mark, Jelle, Remco, Olaf, Nico, Ronald, Jason, Siebe, thanks for being so helpful on the cryostat issues and other lab-related stuff. It it great that you always take time to think with us, ask more questions than we already thought of ourselves to find the issue or the best solution as soon as possible! Raymond, Raymond, Marijn, Jack and Ruud, without you my time spent on electronics would have been infinite! Thanks for explaining things that must be peanuts for you guys, helping to find the best solutions and to solve any electronics-related issues!

Basia, thanks to you I became a scientist. I am so grateful that I met you during my bachelor project and that we became good friends later on. Together with Yun and Marieke we had the best times. David and Önder, it's been a long four years since we started together on our first day. I am so happy to see you guys found your path, both scientifically and in life: so grown up! Arjan and Jakob, we had the best office! With both of you I have had great conversations about science and many other things. Erika, you are one of the strongest women I have met, thanks for sharing rooms with me at conferences. Tim Baart, we have had both fun and serious conversations on everything in academia and going to conferences and schools with you always resulted in the best activities, like swimming in the ice-cold lake Konstanz. Niels, coming back to QuTech was one of your best decisions, you really fit in and it is great to see you flourish in the team. Besides that, it's been a great bonus that you are always around!

Besides the people within QuTech, I have strolled around the TU Delft and found many valuable people there. Miriam, I am so happy to have had you as my mentor during my PhD. You are an amazing support and it is great that you can both just listen and give your valuable vision at the right times. Both you and Sander are great teachers and it was great to assist in 'Vaste Stof Fysica'. Pauline, all our lunches and tea-moments have been very valuable, we both went through ups and downs and you always helped me with great advise, funny pictures or just a big hug. Max, from house-mates to far-away collegues and friends, if your office were not that crazy far away we would have had much more chats, but I'm not sure if that would have been good for our work-output. Paula and Tanja, thank you for the help and advise when I needed it most. Michel and Roy, I am so happy to have met you; your trainings are great but I mainly want to thank you for the advises you gave me on the future! Marije, Jan, Tjerk and the rest of the Casimir committee, I really enjoyed to organise the spring school and to help think about other important things within the Casimir Research School. Marije, thanks for always forwarding me great ideas and invitations.

My future would not have been so clear for me without all the great people that I met when exploring science communication. Ionica, thank you for making time for advice at first, and for all your thrust in me to offer me a position; I am really looking forward to working together! Ron and Eric, already during my studies you gave me the opportunity to write for Breen, thank you so much. KNAW and Kennislink, Irene, Iris, Sanne, Edda, Martine and Jasmijn, thanks for organising Faces of Science, for your enthusiasm in giving young scientists a face. I am very happy that I responded to your email about ScienceBattle: René, Suzanne, Patrick and Richard and all participants, I feel part of a new family. Thanks to you I learned to enjoy standing on a stage and interacting with an audience! Bruno, it was a lot of fun to make a movie on my main result with you. Martijn, Krijn, Jeroen, Rolf, Jos, Roel and Ruud, I hope there will future opportunities to work together again. Marjolijn, Job, Julia, Patrick, Yarona and Jonathan, thanks for the opportunity to speak at your events

and thanks for the coaching to make my story great!

Finally I want to thank all my family and friends, a few in particular. Marleen, thanks for always showing interest in what I am doing, while you are the one that is most distant to my research topic. Please keep on telling physics jokes! Caroline, our unconditional friendship should not need any thanks, however I am very grateful to have something so positive for the rest of our lives out of that year of Industrial Design! I am looking forward to sharing all our future adventures in life, preferably on a couch on sunday afternoons. Niels and Suus, my paranymphs, we go way back! While I was convinced I didn't need any nerd-friends in the physics building, you were the first to show me the opposite, and all time has been fun ever since. Mischa, I am increadibly proud of all your achievements and very happy that there is still plenty of room for tea and chats. Anne-Marije, I hope we will have plenty more moments involving either chocolate or sweat.
Papa en Mama, dankjewel voor alles wat jullie mij hebben meegegeven, niet alleen door jullie opvoeding maar ook in al jullie sterke eigenschappen! Stijn, elke keer als ik je zie vraag ik me af waar mijn kleine broertje is gebleven, ik ben ongelooflijk trots op je! Opa en Oma, ik ben heel blij dat jullie niet alleen deze dag meemaken maar ook zo ontzettend betrokken zijn bij alle stappen die ik zet. Dankjewel voor al jullie advies, vertrouwen en enthousiasme. Leen, tante Betty, PJ en alle anderen, ik voel me als buitenstaander en buitenlander altijd welkom. Lex, $1 + 1 = \infty$, thanks for being you!

List of Publications

1. *Experimental creation of quantum Zeno subspaces by repeated multi-spin projections in diamond.*
   N. Kalb, J. Cramer, D.J. Twitchen, M. Markham, R. Hanson, T.H. Taminiau,
   Nat. Commun. **7**, 13111 (2016).
2. *Repeated quantum error correction on a continuously encoded qubit by real-time feedback.*
   J. Cramer, N. Kalb, M.A. Rol, B. Hensen, M.S. Blok, M. Markham, D.J. Twitchen, R. Hanson, and T.H. Taminiau.
   Nat. Commun. **7**, 11526 (2016)
3. *Universal control and error correction in multi-qubit spin registers in diamond.*
   T.H. Taminiau, J. Cramer, T. van der Sar, V.V. Dobrovitski, R. Hanson,
   Nat. Nanotech. **9 (3)**, 171-176 (2014).
4. *Entanglement genesis by ancilla-based parity measurement in 2D circuit QED.*
   O.P. Saira, J.P. Groen, J. Cramer, M. Meretska, G. De Lange, L. DiCarlo,
   Phys. Rev. Lett. **112 (7)**, 090502 (2014).
5. *Partial-measurement backaction and nonclassical weak values in a superconducting circuit.*
   J.P. Groen, D. Riste, L. Tornberg, J. Cramer, P.C. De Groot, T. Picot, G. Johansson, L. DiCarlo,
   Phys. Rev. Lett. **111 (9)**, 090506 (2012).

Curriculum Vitae

Julia Cramer

Jan. 30, 1988	Born in Eindhoven, The Netherlands.
2000 - 2006	Secondary school, *Oostvaarders College*, Almere, The Netherlands.
2007 - 2010	B. Sc. Applied Physics, *Delft University of Technology.* Graduated Cum Laude. Graduation research in the Quantum Transport group. Supervisor: Dr. ir. V. Zwiller.
2010 - 2012	M. Sc. Applied Physics, *Delft University of Technology.* Selected for Casimir Pre-PhD program. Graduation research in the Quantum Transport group. Supervisor: Dr. ir. L. DiCarlo.
2011	Research internship, *Delft University of Technology.* Research project in the Theoretical Physics department. Supervisor: Dr. M. Blaauboer.
2011	Research internship, *ETH Zurich.* Research project in the Quantum Optics department. Supervisor: Prof. A. Imamoglu.
2012 - 2016	Ph.D. researcher, *Delft University of Technology.* Funded by Casimir prize PhD position. Subject: Quantum error correction with spins in diamond Group: QuTech and Kavli Institute of Nanoscience. Promotor: Prof. dr. ir. R. Hanson. Co-promotor: Dr. ir. T. H. Taminiau.

ISBN 978-90-8593-270-3
Casimir PhD series 2016-26

TU Delft Delft University of Technology

TEAM DIAMOND EST. 2008 A.D.

QUTech